

POLITECNICO OF TORINO

Wireless Systems Design

Master's Thesis Project

WIDEBAND FABRY-PÉROT CAVITY ANTENNA WITH OVERLAPPING FEEDS FOR ADVANCED COMMUNICATIONS



Candidate:
Alessio Berto
s244081

Supervisor:
Ladislau Matekovits

Supervisor in the Host institution
University of California Irvine:
Filippo Capolino

December 2019

ABSTRACT

This Master's Thesis project suggests a general procedure to design a Fabry-Pérot Cavity (FPC) antenna with two feeding that can be used for advanced communications. In order to better understand the characteristics of this kind of antennas, a theoretical introduction on Leaky-Wave antenna (LWA) is presented at the beginning. Then, the antenna design starting from the basic unit cell is presented, explaining each step and showing several combinations of the FPC antenna parameter, in particular cavity height and distance between the feeding point of the two patches, in order to find the best solution for the broad-side gain. Moreover, an optimization for the patch dimensions has been carried out in order to have good matching at the two designed frequencies. The final antenna is composed of two coaxial fed patch antennas on a RT5880 ($h = 0.787\text{mm}$, $\epsilon_r = 2.2$ and $\delta = 0.0009$), an air cavity and a Partially Reflective Surface (PRS), on a RO3010 dielectric ($h = 0.64\text{mm}$, $\epsilon_r = 11.2$ and $\delta = 0.0022$), with 14×14 unit cells. The designed antenna shows a wide bandwidth, of almost 6 GHz, within 18 – 28GHz range with a maximum gain of 13.5dB at the two designed frequencies of operation: 20.7 GHz and 24.3 GHz, respectively. Furthermore, the structure has been fabricated and a comparison between its measurements and simulated data has been carried out. The overall project and the fabricated structure measurements have been carried out in part at the University of California Irvine (UCI) and in part at the Politecnico of Torino.

Nihil est magnum somnianti.

— M. Tulli Ciceronis [1]

ACKNOWLEDGMENTS

I would like to thank my supervisor in Italy, Professor Ladislau Matekovits, and in the host institution, Professor Filippo Capolino, for helping me better understand such interesting but not intuitive topic. I would like also to thank them for allowing me to work on a design project related to this topic and to thank all the P.h.D. student that helped me in the lab.

A particular thanks also to Professor Franco Maddaleno for guiding me during the first days in the host institution.

Last but not least, I would like to thank my mother and father that assisted me during all these university years. I would like also to thank all my friends for all the encouragement and support they gave me in the saddest moment and for the fun we had together. In particular, even if our paths are now divided, I want to thank Silvia for having sustained me during my worst moments of the past.

CONTENTS

I PREFACE

- 1 INTRODUCTION 3
 - 1.1 Background 3
 - 1.2 Aim & contribution 4
 - 1.3 Outline 4

II STATE OF ART

- 2 ANTENNAS INTRODUCTION 7
 - 2.1 Antenna Parameters 7
 - 2.1.1 Radiation pattern and Beamwidth 8
 - 2.1.2 Radiation intensity, Efficiency, Directivity and Gain 9
- 3 LEAKY-WAVE ANTENNAS 11
 - 3.1 Historical Introduction 11
 - 3.2 General Introduction 12
 - 3.2.1 Principle of Operation 12
 - 3.3 2-D Leaky-Wave Antennas 14
 - 3.3.1 Principle of Operation and Wide-band analysis for FPC antenna 17
- 4 SOURCES 25
 - 4.1 Slot Antenna 25
 - 4.2 Patch antenna 26
 - 4.2.1 Design 27
 - 4.2.2 Input impedance and feeding location 28

III SIMULATIONS

- 5 UNIT CELL DESIGN 33
 - 5.1 Unit cell geometry solutions 33
 - 5.1.1 PRS reflection coefficient comparison 34
 - 5.1.2 PRS resonance height comparison 35
 - 5.1.3 Radiation intensity comparison 36
 - 5.2 PRS with circular hole on the bottom 37
 - 5.2.1 Reflection coefficient comparison 37
 - 5.2.2 Resonance height comparison 39
 - 5.2.3 Radiation intensity comparison 39
 - 5.3 Optimized solution 40
- 6 DESIGNED FPC ANTENNA 45
 - 6.1 Slot Feeding 45
 - 6.1.1 Slot Design 45
 - 6.1.2 Single feeding FPC 46
 - 6.2 Patch Feeding 47
 - 6.2.1 Unit Cell Analysis 48

6.2.2	Patch Design	50
6.2.3	Single port	51
6.3	FPC fed by two patches	52
6.3.1	Final structure	56
IV FABRICATION AND CONCLUSION		
7	FABRICATION AND TEST	61
7.1	Fabrication	61
7.2	Test	62
8	CONCLUSIONS	65
8.1	Future analysis	65
V APPENDIX		
A	ATMOSPHERIC ABSORPTION AT EHF	69
B	TEN MODEL ADMITTANCES DERIVATION	71
B.1	Evaluation of Y_{down}	71
B.2	Evaluation of Y_{up}	72
C	ROGER SUBSTRATE THICKNESS LIMITATIONS	75
C.1	RO3210	75
C.2	RO4360G2	76
C.3	TMM13i and TMM10i	76
C.4	RO4350B	78
D	DATASHEET RO3010	79
E	DATASHEET RO5880	85
F	DATASHEET SMA CONNECTOR	89
G	SIMULATION MESH AND ACCURACY	95
G.1	Unit cell	95
G.2	Radiating source	99
G.3	Single fed structure	100
G.4	Double fed structure	102
BIBLIOGRAPHY		103

LIST OF FIGURES

Figure 2.1	Equivalent Transmitter (T_x) and Receiver (R_x) antenna circuits.	7
Figure 2.2	Radiation pattern example.	8
Figure 3.1	Generic LWA representation.	13
Figure 3.2	two-dimensional (2-D) LWA geometry.	15
Figure 3.3	2-D LWA beams.	15
Figure 3.4	2D LWA cross section.	16
Figure 3.5	PRS-based LWAs.	17
Figure 3.6	FPC antenna geometry and two port network model for a slot source.	18
Figure 4.1	Example of Slot Antenna.	25
Figure 4.2	Complementary structures.	26
Figure 4.3	Example of Patch Antenna.	26
Figure 4.4	Resonant cavity model.	27
Figure 4.5	Patch Transmission Line (TL) model.	28
Figure 4.6	Patch TL model without fringing effect.	28
Figure 4.7	Z_{in} evaluation.	29
Figure 4.8	Inset fed solutions.	29
Figure 4.9	Optimum patch feeding distance.	30
Figure 5.1	Investigated geometries for a PRS unit cell.	33
Figure 5.2	PRS reflection coefficient magnitude and phase for different substrates and geometries.	34
Figure 5.3	Cavity height plots for different substrates and geometries.	35
Figure 5.4	Radiation intensity graphs for different substrates and geometries.	36
Figure 5.5	Unit cell geometry with and without glue.	37
Figure 5.6	Reflection coefficient magnitude analysis for glued PRS.	38
Figure 5.7	Reflection coefficient phase analysis for glued PRS.	38
Figure 5.8	Cavity height analysis for glued PRS.	39
Figure 5.9	Radiation intensity analysis for glued PRS.	40
Figure 5.10	Optimized PRS geometry and reflection coefficient magnitude and phase.	40
Figure 5.11	Optimized cavity height.	41
Figure 5.12	Optimized radiation intensity graph.	41
Figure 5.13	α and β diagram.	42
Figure 5.14	Radiation intensity vs. Angle θ .	43
Figure 5.15	Radiation intensity vs. Angle θ at the 20.37GHz and 23.8 GHz.	43

Figure 6.1	Slot antenna.	45
Figure 6.2	Slot reflection coefficients.	46
Figure 6.3	Single slot fed FPC antenna.	46
Figure 6.4	Slot with PRS matching solutions at 23.8GHz.	47
Figure 6.5	Slot with PRS matching solutions at 20.37GHz.	47
Figure 6.6	FPC antenna geometry and two port network model with for a Patch source.	48
Figure 6.7	Unit cell simulation by using reciprocity theorem.	49
Figure 6.8	Normalized radiation intensity for patch feeding.	49
Figure 6.9	Radiation intensity vs. angle θ for patch feeding.	50
Figure 6.10	Patch antenna with coaxial feeding.	50
Figure 6.11	Reflection coefficients for the patch sources.	51
Figure 6.12	Single patch fed FPC antenna.	51
Figure 6.13	Reflection coefficients for the single patch fed FPC antenna.	52
Figure 6.14	Double Fed FPC antenna	52
Figure 6.15	S ₁₁ and S ₂₂ of the double fed FPC antenna.	53
Figure 6.16	Double Fed FPC antenna broadside gain.	53
Figure 6.17	Cavity height tuning.	54
Figure 6.18	Distance between feeding lines.	55
Figure 6.19	Tuning of the distance between feeding lines	55
Figure 6.20	Patches re-tuning effect on S ₁₁ and S ₂₂ for a better matching.	56
Figure 6.21	Patches re-tuning effect on broadside gain.	56
Figure 6.22	S ₁₂ , S ₂₁ , Radiation efficiency and total efficiency.	57
Figure 6.23	Broadside and realized gain.	58
Figure 6.24	Comparison between 14x14 and 20x20 unit cell PRS.	58
Figure 7.1	Fabricated antenna.	61
Figure 7.2	S ₁₁ and S ₂₂ with and without PRS comparison.	62
Figure 7.3	Measurements and full wave simulation comparison between S ₁₁ and S ₂₂	62
Figure 7.4	Broadside gain comparison for large patch.	63
Figure 7.5	Broadside gain comparison for small patch.	63

Figure 7.6	<i>E</i> - and <i>H</i> -plane measurements vs simulations comparison. 64	
Figure A.1	RF signal attenuation due to atmospheric gases. 69	
Figure B.1	TL model for Y_{down} . 71	
Figure B.2	TL model for Y_{up} . 73	
Figure B.3	Equivalent TL model for Y_{up} . 73	
Figure G.1	Unit cell boundary conditions. 95	
Figure G.2	Unit cell Floquet port. 96	
Figure G.3	Unit cell type of mesh. 96	
Figure G.4	Unit cell frequency domain solver setup. 97	
Figure G.5	Unit cells mesh number setup. 98	
Figure G.6	Unit cell mesh view. 98	
Figure G.7	Radiating source boundaries. 99	
Figure G.8	Radiating source port and mesh view. 100	
Figure G.9	Radiating source mesh number setup. 100	
Figure G.10	Single fed structure mesh view. 101	
Figure G.11	Single fed structure mesh setup. 101	
Figure G.12	Double fed structure mesh view. 102	
Figure G.13	Double fed structure mesh number setup. 102	

LIST OF TABLES

Table C.1	Roger Cladding Thickness Notation.	75
Table C.2	RO3210 limitations.	75
Table C.3	RO4360G2 limitations.	76
Table C.4	TMM13i limitations.	76
Table C.5	TMM10i limitations.	77
Table C.6	RO4350B limitations.	78
Table D.1	RO3010 thickness limitations.	79
Table E.1	RO5880 thickness limitations.	85

ACRONYMS

FPC	Fabry-Pérot Cavity
LWA	Leaky-Wave antenna
PRS	Partially Reflective Surface
EBG	Electromagnetic Band-Gap
SHF	Super High Frequency
EHF	Extremely High Frequency
MMW	MilliMeter-Wave
CMOS	Complementary Metal-Oxide Semiconductor
LO	Local Oscillator
Tx	Transmitter
Rx	Receiver
HPBW	Half Power Beamwidth
FNBW	First Null Beamwidth
SLL	Secondary Lobe Level
1-D	one-dimensional
2-D	two-dimensional
HED	Horizontal Electric Dipole
HMD	Horizontal Magnetic Dipole
VED	Vertical Electric Dipole
VMD	Vertical Magnetic Dipole
TEN	Transverse Equivalent Network
TL	Transmission Line
SGH	Standard Gain Horn
SMA	SubMiniature version A

Part I

PREFACE

INTRODUCTION

1.1 BACKGROUND

In the last few decades, the explosive development of wireless communications has led to a growing request of wider bandwidth and high-speed communication.

In order to provide a solution to this growing demand, the operational band has been increased from Super High Frequency (SHF), saturated in the available frequency bandwidth now, towards the Extremely High Frequency (EHF).

There are many applications for this recently available frequency band: from radio astronomy and remote sensing to broadband mobile systems, from automotive and military radar to security imaging like detectors [2].

Unfortunately, designing for MilliMeter-Wave (MMW) band has shown the incompatibility of planar antennas due to their low radiation efficiency and gain, the significant intrinsic loss related to the material used, metal and dielectric, and the high atmospheric absorption in some portions of this band [3].

Moreover, powerful generators and power amplifiers that provide higher gain are needed to work on shorter wavelengths because functioning on shorter transmission range for a given power.

However, obtaining the firsts is a challenge because phase noise or jitter in the carrier frequency led to an accuracy degradation of the system while a well generated Local Oscillator (LO) signal not properly delivered will degrade the overall system performances [4].

The same challenge holds for the seconds where of linearity requirements and limited supply voltage for Complementary Metal-Oxide Semiconductor (CMOS) technology are the main issues [5, 6].

Due to this designing difficulties, low profile antennas with high gain and radiation efficiency started to be fundamental in order to compensate these high losses and low generated output power.

A promising solution, due to its high radiation efficiency, good pattern performances and low profile nature, is the Fabry-Pérot Cavity (FPC) antenna, a planar leaky-wave structure that has been hardly investigated in recent years [7, 8]. It is based on a dielectric cavity, where the source is placed, bounded on the bottom by a metal ground plane and on the top by sort of semi-transparent mirror, made of a Partially Reflective Surface (PRS). This layer in part reflects the wave generated by the source and in part let it pass through. The multiple reflection of the wave, that bounce in the cavity, allows an increase of the electrical

aperture size.

1.2 AIM & CONTRIBUTION

This thesis presents a general design process for a wide-band and high gain FPC antenna with double feeding usable both for MMW and microwave applications in order to provide a better solution with respect to existing structures.

Starting from the design for a one feed wide-band FPC antenna explained in [7], the idea is to optimize the illumination efficiency by adding another source with its own feed taking into account the work [8] using CST Microwave Studio as commercial software for the simulations. In order to design this FPC antenna, the following procedure has been carried out. The PRS unit cell has been designed in order to obtain a wide-band behavior for the final structure. Afterwards, to obtain the same value of broadside gain at the two main frequencies of interest, the cavity height and distance between feeding points variation has been investigated. Moreover, the two patches have been matched at the two operational frequencies.

The final structure obtained from this evaluations has then been fabricated and tested. The comparison between experimental results and simulation data exhibits a good agreement.

1.3 OUTLINE

This thesis consists of three more parts:

- in Part ii, after a brief introduction on various antenna parameters, Chapter 2, the theoretical background behind LWAs and FPC is proposed in Chapter 3. An overview on their possible radiating sources, focusing on the design procedure, is presented in Chapter 4;
- in Part iii, the design and simulation results of the unit cell is proposed in Chapter 5. Then of the final antenna, Chapter 6, are presented;
- in Part iv, particularly in Chapter 7, the fabricated structure is presented and the test results are compared to the simulation ones. Then in Chapter 8 the project results are discussed and reviewed.

Part II

STATE OF ART

ANTENNAS INTRODUCTION

Before introducing **LWAs** and their characteristics, and overview on what antennas are and their most important parameter has to be done. In wireless communications systems, antennas are fundamental components: they provide the necessary coupling between circuits and open space allowing the information transfer between a **Tx** and a **Rx** through free space propagation. In particular, a **Tx** antenna is the system element that, fed by a power source, transforms guided power on a transmission line, for example a microstrip or waveguide, to radiated power in space. On the contrary, a **Rx** antenna transforms the electromagnetic field and power density associated to an incident wave in power along a transmission line linked to a receiver. The equivalent circuits for **Tx** and **Rx** cases are reported as follows:

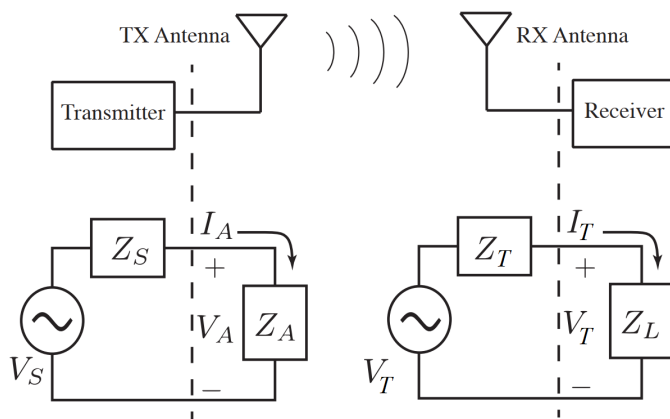


Figure 2.1: Equivalent circuits for a **Tx** and **Rx** antenna.

- **Tx** antennas behave as loads for their feeding transmission lines and so characterized by an input reflection coefficient value. The transmitter can be modeled with a voltage generator plus its self impedance;
- **Rx** antennas behave as generators and they are modeled with a Thevenin equivalent circuit;

2.1 ANTENNA PARAMETERS

Various parameters are really important to describe the performances of an antenna, from the radiation pattern to the gain, directivity and efficiency. In this chapter, the most useful formulas and concepts for the comprehension of the topic are reported.

2.1.1 Radiation pattern and Beamwidth

The antenna radiation pattern is a graphical representation of the radiated energy distribution as function of space coordinates [9, 10].

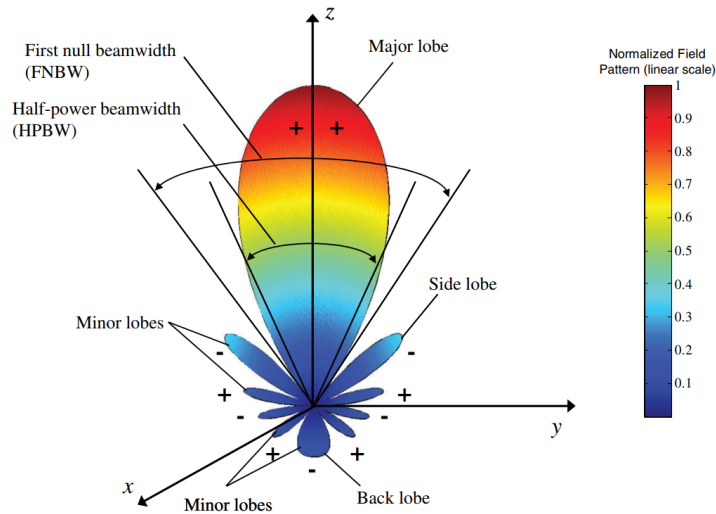


Figure 2.2: Example of radiation pattern. (Fig. 2.3 of [10])

Radiation patterns can be classified in three major groups:

- *isotropic*; the radiation pattern is the same in all directions. Antennas with this property do not exist in practice, they are ideal and they are used as reference to express the real antennas radiation properties;
- *omnidirectional*; antennas that behaves like an isotropic radiator in a plane and like a directional one in the orthogonal plane. For example, dipoles or slots belongs to this category;
- *directional*; antennas with this property do not show any symmetry in the radiation pattern. They have a main peak in the direction where the radiated power travels. The omnidirectional ones are a subcategory of these;

The radiation pattern can be subdivided in regions that have a local maximum separated from each other by points, *nulls*, where the radiated signal strength drops to zero. These pattern portions are called lobes and they can be classified as follows:

- *major lobe*, also called *main beam*, is defined as the radiating lobe containing the direction of maximum radiation;
- *minor lobes*; they comprehends any lobe except the main one. They can be called:

- *side lobe*; any lobe except the main one that contain a maximum can be called in this way;
- *back lobe*; it is the radiation lobe whose axis makes an angle of 180° with respect to the antenna main beam;

Linked to the side lobes concept, it is important to mention the *Secondary Lobe Level (SLL)*, defined as the value of the side lobe adjacent to the main beam. The antenna pattern is usually analyzed by looking at its *E*- and *H*-plane, where the *E* and *H* field lies on, respectively. These planes are orthogonal to each other because the two field are orthogonal. Another important parameter related to the radiation pattern is the *beamwidth* that represents the angular distant between two identical points at the opposite side with respect to the main beam. are:

- *Half Power Beamwidth (HPBW)*; in the plane of maximum direction, it is defined as the angle at which the radiated power is reduced of 3dB;
- *First Null Beamwidth (FNBW)*; it is defined as the angular separation between the first pattern nulls.

2.1.2 Radiation intensity, Efficiency, Directivity and Gain

The *radiation intensity* is defined as the power radiated from an antenna per unit solid angle [10]. In the far field zone, it can be expressed as:

$$U(\theta, \phi) = \frac{r^2}{2\eta} |E(r, \theta, \phi)|^2, \quad (2.1)$$

where $E(r, \theta, \phi)$ is the electric field expressed in spherical coordinates, $\eta = Z = \sqrt{(\mu_0\mu_r)/(\epsilon_0\epsilon_r)}$ is the medium characteristic impedance and r is the distance. The isotropic radiation intensity is defined as [10]:

$$U_0 = \frac{P_{rad}}{4\pi}, \quad (2.2)$$

where P_{rad} is the total power radiated.

Antenna *directivity* is defined as the ratio between the antenna radiation intensity in a given direction and the isotropic one.

$$D = \frac{U}{U_0} = \frac{4\pi U}{P_{rad}}. \quad (2.3)$$

if the beamwidth is known, the maximum antenna directivity can be computed through an approximated formula [10]:

$$D = \frac{4\pi}{\Omega_A} = \frac{4\pi\epsilon_m}{\Omega_M} \approx \frac{4\pi\epsilon_m}{HP_E * HP_H} = \frac{41,253\epsilon_m}{HP_{E^\circ} * HP_{H^\circ}}, \quad (2.4)$$

where Ω_A is solid angle of the entire pattern, Ω_M is the main beam solid angle that, in many cases, is approximated by the product of the half-power beam-widths in the E - and H -plane patterns, HP_{E° and HP_{H° , and ε_m the beam efficiency. If the pattern has no side lobes, so no power outside the main beam, $\varepsilon_m = 1$ and the formula becomes:

$$D = \frac{41.253}{HP_{E^\circ} * HP_{H^\circ}}. \quad (2.5)$$

The gain is defined as the ratio of the intensity, in a given direction, to the isotropic radiation intensity. It can be expressed as:

$$G = 4\pi \frac{U(\theta, \phi)}{P_{in}}. \quad (2.6)$$

The radiation intensity of an isotropic source is equal to the power P_{in} accepted by the antenna divided by 4π . Through the radiation efficiency concept, a relation between the gain and the directivity can be established. The total antenna efficiency R_{tot} takes into account the losses at the input terminals and within the antenna structure, such as conduction, dielectric and reflection losses for the mismatch between the transmission line that is feeding the antenna and the antenna itself.

$$R_{tot} = R_{eff}(1 - \Gamma_{in}), \quad (2.7)$$

where R_{eff} is the antenna radiation efficiency that is caused by conduction and dielectric losses. Because the total radiated power is related to the total input power by R_{eff} , the gain is related to the directivity by the following formula:

$$G = R_{eff}D. \quad (2.8)$$

The realize gain is defined as the gain that takes into account the reflection/mismatch losses of the structure and it can be expressed as:

$$G_R = (1 - |\Gamma|^2) G. \quad (2.9)$$

By looking at Fig. 2.1, the Tx antenna is a load impedance of value $Z_A = R_A + jX_A$. The resistance is defined as $R_A = R_r + R_L$, where R_r is the antenna radiation resistance and R_L the antenna loss resistance. From this expression, R_{eff} can be written as:

$$R_{eff} = \frac{R_r}{R_r + R_L}. \quad (2.10)$$

In this chapter, a theoretical background about LWAs is presented in order to show their basic physics and operating principles. Afterwards, their 2-D version, usually referred in literature as FPC or Electromagnetic Band-Gap (EBG) antennas [11], is introduced.

3.1 HISTORICAL INTRODUCTION

LWAs have been firstly discovered and analyzed by W. W. Hansen in 1946 through the use of a slotted rectangular wave-guide [12]. Unfortunately, only from 1950s they have been hardly investigated developing multiple types and methods to analyze them. The basic physical concepts of leaky modes have been set by Marcuvitz in [13] while the operation of LWAs based on rectangular wave-guides have been explained in [14] by Arthur A. Oliner.

In the meanwhile, multiple structures have been analyzed. Starting from a closed wave-guide with leaking long uniform slits, main reason for the radiation, this slots were then replaced by a series of closely spaced holes [15] in order to obtain much narrower beams. With further researches, it has been found by Rotman and colleagues that an open guide structure, even if it wouldn't radiate because of its symmetry, can leak adding some asymmetries at the design [16].

Just in 1960s an organic and elegant explanation of leaky waves have been performed by Oliner [17, 18] that, some decades after, in 1980s, published a summary of the work performed with his co-workers on one-dimensional (1-D) LWAs [19].

The first concept of 2-D LWAs has been introduced by von Trentini [20] where a partially reflective mirror has been used over a ground plane to increase the directivity at broadside obtaining in this way a pencil beam. This configuration is the one that by then will be called FPC antenna. Other investigations on 2-D LWAs have been performed using dielectric superstrate layer over a substrate one [21, 22], even if not recognized as leaky wave, then on the same configuration but as leaky wave [23, 24]. Thanks to the work of Feresidis and Vardaxoglou, [25], 2-D LWAs have been examined in detail using reflecting screens consisting of various elements, like dipoles or patches, which set the seeds for following researches and investigations [26, 27]. From these two latest works published at the beginning of this century till now, novel FPC structures have been developed trying to obtain wider or even narrower beam at broadside [7, 8, 28].

3.2 GENERAL INTRODUCTION

A *LWA* is basically a wave-guiding structure with continuous or periodic discontinuities that allow energy leakage nearby. They are characterized by a low fabrication complexity, in fact no complicated beam forming network is required as in a phased array antenna, and by narrow beam. For these reasons they have become attractive for MilliMeter-Wave (*MMW*) and microwave frequency range applications [29].

Moreover, highly directive beams can be obtain with this structure obtaining a low-side level due to a tapered aperture distribution. In general the phase constant of the leaky wave controls the beam angle while the attenuation constant affects on the beam-width. In terms of geometry, *LWAs* can be mainly classified into two structure: one-dimensional and two-dimensional. After a brief discussion about the physics behind *LWA*, the focus will be on *FPC* resonator.

3.2.1 Principle of Operation

A leaky wave antenna supports a fast wave with $\beta < k_0$. In order to understand how it works, consider the radiated field from the structure as presented in Fig. 3.1.

$$\Psi(\vec{r}) = \Psi(\vec{\rho})e^{-jk_z\hat{z}}. \quad (3.1)$$

The wave-guiding structure extends along the z axis and $\vec{\rho} = x\hat{x} + y\hat{y}$ represents the position vector. The presence of apertures, that may be continuous, discontinuous, and/or periodic, allows radiation and so energy leakage. For this reason, the propagation wave-number is complex and consisting of both terms:

$$k_z = \beta - j\alpha, \quad (3.2)$$

where β and α are real numbers. Substituting expression (3.2) into Eq. (3.1) led to the following relation:

$$\Psi(\vec{r}) = \Psi_0(\vec{\rho})e^{-j(\beta-j\alpha)\hat{z}} = \Psi_0(\vec{\rho})e^{-j\beta\hat{z}-\alpha\hat{z}}. \quad (3.3)$$

But what do these two constants mean? β is the modal phase, or propagation, constant and α is the leakage, or attenuation, one and they depend on frequency. So, an higher α means that a larger amount of energy leaks from the structure: so it depends on the leakage per unit length along the wave-guide.

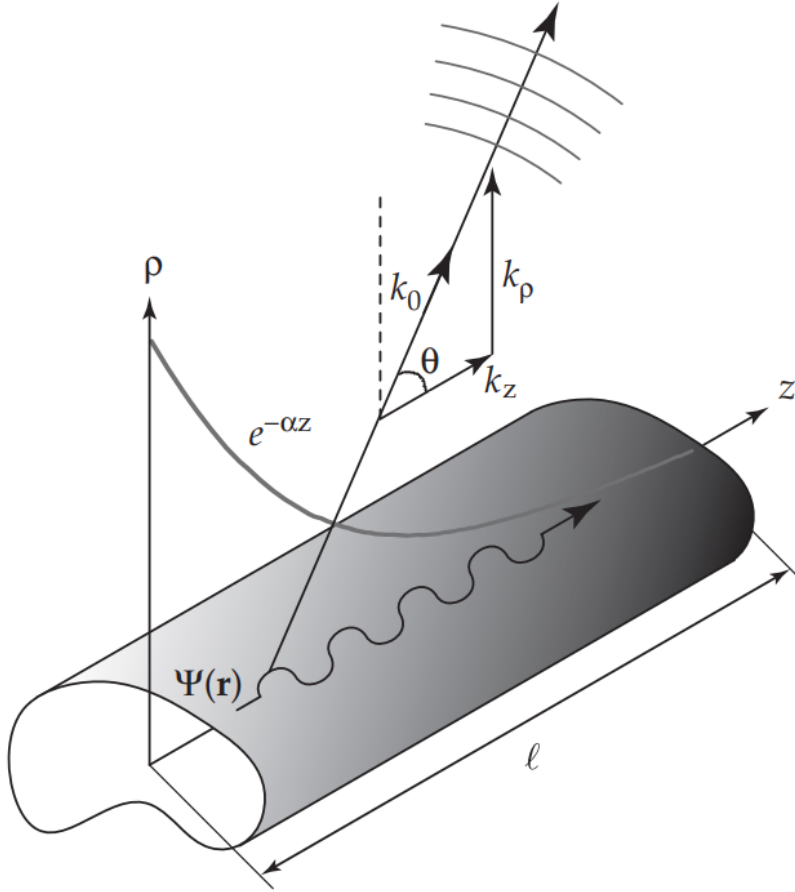


Figure 3.1: Radiation and generic representation of a LWA. (Adapted from Fig. 9-1 of [30])

The general field outside the structure can then be expressed as a plane-wave using the wave-number vector $\vec{k} = k_\rho \hat{\rho} + k_z \hat{z} = k_0 \hat{n}$ that is continuous at the interface with free space along the apertures. In free space, the waveform above the structure is dependent from z , as in Eq. (3.3), and the fields outside the waveguide can be written as:

$$\Psi(\vec{r}) = \Psi_0 e^{-jk_\rho \hat{\rho}} e^{-jk_z \hat{z}} = \Psi_0 e^{-jk_\rho \hat{\rho}} e^{-j\beta \hat{z} - \alpha \hat{z}}. \quad (3.4)$$

By using Eq. (3.2) in the magnitude expression of \vec{k} , the transverse propagation constant k_ρ can be derived:

$$k_\rho = \sqrt{k_0^2 - k_z^2} = \sqrt{k_0^2 - (\beta - j\alpha)^2}. \quad (3.5)$$

Usually in antenna design, $\alpha \ll \beta$ which means that Eq. (3.5) becomes $k_\rho \approx \sqrt{k_0^2 - \beta^2}$ and so k_ρ can only be purely imaginary or real. These two possible cases are listed below:

- If $\beta > k_0$ or, similarly, the phase velocity $v_p = \frac{\omega}{\beta}$ is smaller than the speed of light $c = \frac{\omega}{k_0}$, the wave is called *slow*. For this reason k_ρ is purely imaginary and the wave in free space decays exponentially away from the structure;

- If $\beta < k_0$ or, similarly, the phase velocity v_p is higher than the speed of light c , the wave is called *fast*. For this reason k_ρ is purely real;

If k_ρ is real, the radiation in free space will have the main beam directed along the angle θ with respect to \hat{z} .

$$\begin{aligned}
 k_z = k_0 \sin(90^\circ - \theta) &\longrightarrow \cos(\theta) = \frac{k_z}{k_0} \\
 &\longrightarrow \theta = \cos^{-1} \left(\frac{k_z}{k_0} \right) \\
 &\longrightarrow \theta = \cos^{-1} \left(\frac{\beta}{k_0} \right) \\
 &\longrightarrow \theta = \cos^{-1} \left(\frac{c\beta}{\omega} \right). \quad (3.6)
 \end{aligned}$$

Remembering that β is in function of frequency, Eq. (3.6) will become:

$$\theta(\omega) = \cos^{-1} \left[\frac{c\beta(\omega)}{\omega} \right]. \quad (3.7)$$

The radiation efficiency R_{eff} is defined as [30, 31]:

$$R_{eff} = 1 - e^{-2\alpha L}. \quad (3.8)$$

While the beam-width $\Delta\theta$ can be evaluated with the following approximated formula where the numerator factor 0.91 assumes a radiation efficiency of 90%, which is quite typical in LWAs [30]:

$$\Delta\theta \approx \frac{0.91}{\frac{l}{\lambda_0} \sin(\theta)}, \quad (3.9)$$

where the length l is the antenna one while $\lambda_0 = \frac{2\pi}{k_0}$ is the wavelength in free space.

3.3 2-D LEAKY-WAVE ANTENNAS

This class of LWAs is based on a planar structure, excited by a small source, that can provide a highly directive beam. This small source generates a radially propagating 2-D leaky wave. Its phase fronts are shown in Fig. 3.2 by dashed lines along the planar interface where the source is placed.

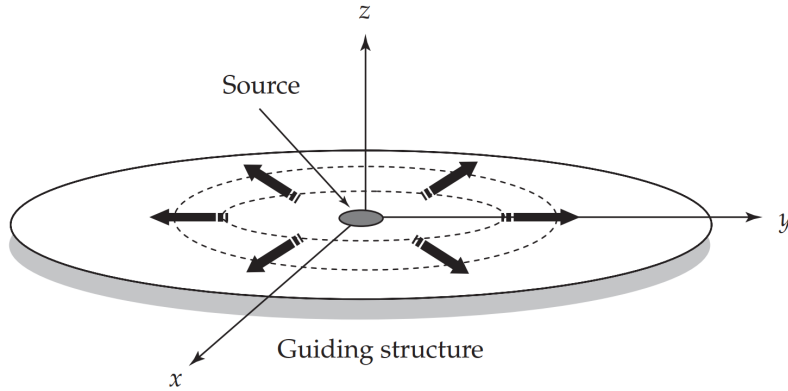


Figure 3.2: Geometry of a 2-D radially-propagating leaky wave that propagates outward the source along the guiding structure. (Fig. 9-16 of [30])

Depending on the source type, two different radiation beams can be produced. The first case, Fig. 3.3a, is a narrow pencil beam pointing at broadside ($\theta_0 = 0^\circ$) while the second, Fig. 3.3b, is a conical beam pointing at any desired scan angle $\theta > 0^\circ$. A conical beam has usually a fairly omnidirectional pattern for small angles θ , but the E - and H -plane beam-widths typically differ more and more as the scan angle increases. As it is true for all LWA, Eq. (3.7), the beam angle is frequency sensitive.

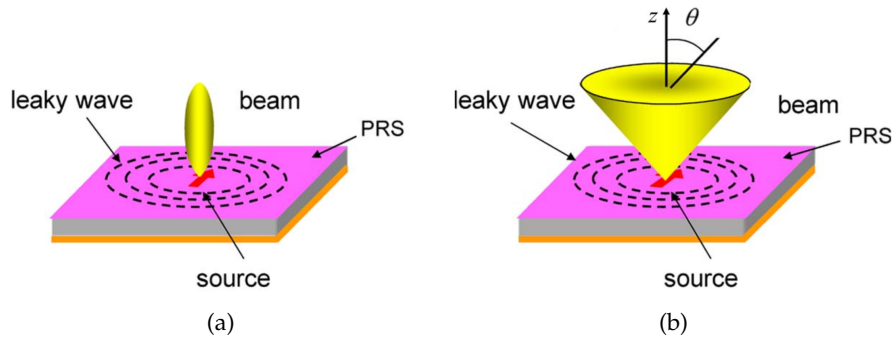


Figure 3.3: Beam types that may be generated from a 2-D LWA: (a) pencil beam at broadside or (b) conical pointing at an angle greater than zero. (Fig. 4 of [11])

Usually a single source, either equivalent vertical dipole or horizontal one, can be used as model to excite the guiding structure. The first category can produce above it only a conical beam, while the second one can generate both pencil and conical beams.

As said before, this kind of 2-D LWAs are planar by nature. They consist of a grounded substrate, with the dielectric that can even be air, of thickness h , where the source is placed, with a planar PRS layer on top. This kind of structure also resembles the Fabry-Pérot interferometer cavity where, one side of the cavity, there is a perfect reflective (ground)

plane. For this reason, they are often referred to Fabry-Pérot cavity antennas. The structure cross section is showed in Fig. 3.4.

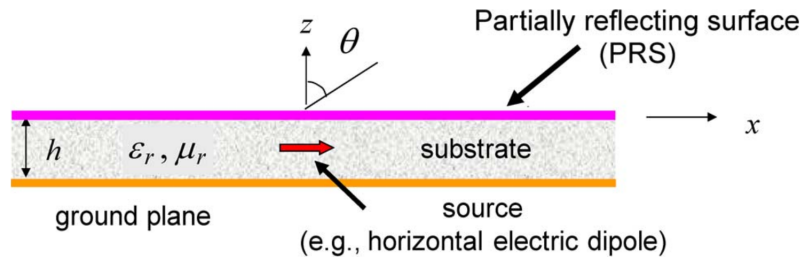


Figure 3.4: Cross section of a PRS antenna excited by a simple source, as a horizontal dipole, inside the dielectric. (Fig. 1 of [11])

The source, in practical, can be a slot antenna placed on the ground plane and wave-guide fed. Otherwise, a patch antenna, placed on a grounded substrate, or a wire one, excited from below the ground plane, can be used. Moreover, the type of feed strongly influences the level of radiation from the structure and it has also a significant effect on the input resistance or conductance seen at the feed terminals. However, it plays a minor role for the radiation pattern shape. The substrate and PRS properties, on the other hand, are of fundamental importance for the radiation characteristics.

For example, to model the radiation pattern, a simple source such as an electric or a magnetic dipole is considered. If the source is a Horizontal Electric Dipole (HED) placed in the middle of the cavity, it can produce a pencil beam at broadside or a conical beam focused at a scan angle θ_0 , as shown in Fig. 3.3. The source place directly affects radiated power, that in turn influences the input resistance seen by a practical feed, and not the beam shape. In particular, the optimum place for the source to maximize the radiated power is in the substrate midpoint, since the horizontal electric field of the leaky mode is maximum there. In the Horizontal Magnetic Dipole (HMD) case, the radiated power is maximized when the source is placed on the ground plane. If the HED is y-axis oriented or the HMD is x-axis oriented, the plane defined by $\phi = 90^\circ$ is the antenna E-plane while $\phi = 0^\circ$ is the H-plane. For what concerns the Vertical Electric Dipole (VED) and Vertical Magnetic Dipole (VMD) cases, radiated power is maximum when they are placed on the ground plane and in the substrate midpoint, respectively. Moreover, as already said before, the pattern is omnidirectional in azimuth.

Various solutions for the partially reflective, or transparent, layer are presented in Fig. 3.5:

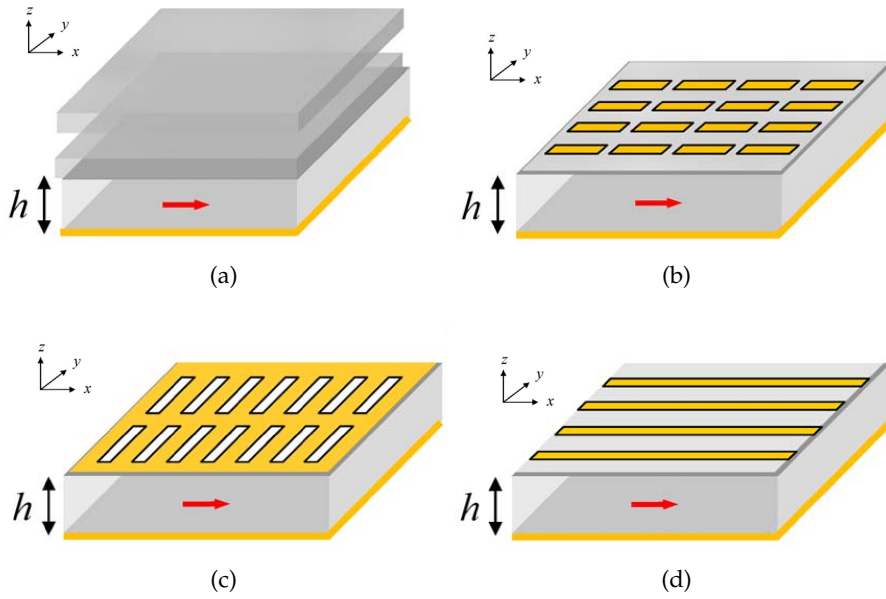


Figure 3.5: Examples of various PRS-based LWAs: (a) The PRS is based on a stack of multiple dielectric layers. (b) The PRS is formed by an array of periodic metal patches. (c) The PRS consists of an array of periodic slots. (d) The PRS is based on a periodic array of closely spaced wires. In each case the excitation source is placed inside the grounded substrate. (Fig. 5 of [11])

In particular, Fig. 3.5b and 3.5c show complementary structures and the slots are 90° rotated from the corresponding patches in order to have the same E - and H -planes. In all cases, the thickness h of the substrate directly controls the beam angle θ and determines whether the beam is broadside, $\theta = 0^\circ$, or conical, $\theta_0 > 0^\circ$. On the other hand, the PRS geometrical properties control the radiation beam-width.

3.3.1 Principle of Operation and Wide-band analysis for FPC antenna

As introduced before, FPC antennas are highly directive and exhibit a narrow beam. In order to obtain a wider beam, various investigations have been done and in [7] a theoretical analysis has been proposed. In this section, a review of this theory is presented to better understand the design process showed in Chapter 5.

In Fig. 3.6, a planar FPC antenna is considered and it is formed by a thick periodic PRS with infinite transverse extent.

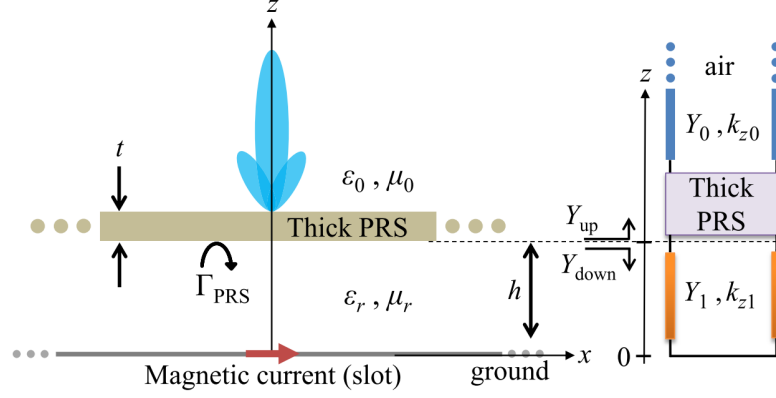


Figure 3.6: Cross section of a FPC antenna composed by a thick PRS and excited by a slot on the ground plane. The slot is modeled with an equivalent x-directed magnetic current on the ground plane. By using TEN model, the thick PRS can be modeled as a two-port network. (Fig. 1 of [7])

The PRS is characterized by a reflection coefficient $\Gamma_{PRS} = |\Gamma_{PRS}|e^{j\phi_{PRS}}$ seen from the bottom substrate side, as showed in Fig. 3.6. Its phase typically increases with frequency in a given band. Moreover, considering a PRS with infinite transverse extent allows to model the structure with the Transverse Equivalent Network (TEN), Fig. 3.6. This model is useful to analyze the antenna as a receiver, illuminated by a plane wave with transverse wave-number k_ρ . It can be also useful to study the same antenna as a transmitter where, for example, a dipole is exciting the structure and the principal interest is the interaction between the source plane wave and PRS. Moreover, it can be used to investigate the leaky modes propagating radially inside the FPC.

3.3.1.1 Radiation intensity Formulas

By using the ray tracing model, the radiation intensity equation can be derived. An antenna source can be, for example, a HMD placed in $z = 0$ with magnetic moment $M_m = I_m l$, where I_m is the magnetic current and l the dipole length. By using the reciprocity theorem, the antenna electric field E_y , at broadside, is related to the magnetic field H_x at source location due to a test y-align electric dipole with moment $M_e = I_e l$ in far field.

$$E_y(z = r = R + h + t) \times (I_e l) = -H_x(z = 0) \times (M_m), \quad (3.10)$$

where R is a distance above the PRS. As showed in Fig.3.6, h and t are the cavity and PRS height, respectively.

The FPC structure, so, is dashed by an incident plane wave that inside the cavity has a real transverse wave-number k_ρ . The characteristic

wave admittances, Y_0 and $Y_1 = Y_0\sqrt{\varepsilon_r/\mu_r}$, for TE modes are defined as:

$$Y_0^{\text{TE}} = k_{z0}/(\omega\mu_0) \quad \text{and} \quad Y_1^{\text{TE}} = k_{z1}/(\omega\mu_0\mu_r), \quad (3.11)$$

while for TM modes:

$$Y_0^{\text{TM}} = \omega\varepsilon_0/k_{z0} \quad \text{and} \quad Y_1^{\text{TM}} = \omega\varepsilon_0\varepsilon_r/k_{z1}. \quad (3.12)$$

The vertical wave-numbers in the air and cavity by using TEN are $k_{z0} = \sqrt{k_0^2 - k_\rho^2}$ and $k_{z1} = \sqrt{k_0^2\mu_r\varepsilon_r - k_\rho^2}$, respectively. These values can be expressed in function of the spherical angle θ when incoming plane waves in this direction impinge the structure: so $k_{z0} = k_0 \cos \theta$ and $k_{z1} = k_0\sqrt{\mu_r\varepsilon_r - k_\rho^2/k_0^2} = k_0\sqrt{\mu_r\varepsilon_r - \sin^2 \theta}$ [32].

The electric dipole generates an E -field:

$$E_y = E_0 M_e \left(\frac{e^{-jk_0 R}}{R} \right), \quad (3.13)$$

where $E_0 = \frac{j\omega\mu_0}{4\pi}$. In far field, $R \approx r$, the incident radiation intensity U^{inc} on top of the PRS can be evaluated from Eq. (2.1):

$$\begin{aligned} U^{\text{inc}} &= \frac{|E_y|^2}{2Z_0} r^2 \quad \longrightarrow \quad U^{\text{inc}} = \left| E_0 M_e \left(\frac{e^{-jk_0 r}}{r} \right) \right|^2 \frac{1}{2Z_0} r^2 \\ &\longrightarrow \quad U^{\text{inc}} = |E_0 M_e|^2 \left(\frac{1}{r^2} \right) \frac{1}{2Z_0} r^2 \\ &\longrightarrow \quad U^{\text{inc}} = \frac{|E_0|^2}{2Z_0} |M_e|^2. \end{aligned} \quad (3.14)$$

where $\eta = Z_0$ because, above the PRS, there is air. The PRS can be modeled as a two port network where the first port is above it and the second one below between its bottom face and the short circuited TL. The transmitted power through the reflective surface is:

$$U^{\text{TX}} = U^{\text{inc}} |S_{21}|^2. \quad (3.15)$$

From reciprocity and energy conservation for a lossless PRS, the following relations hold: $S_{21} = S_{12}$ and $|S_{12}|^2 = 1 - |S_{22}|^2$. Moreover, since $S_{22} = \Gamma_{\text{PRS}}$:

$$U^{\text{TX}} = U^{\text{inc}} |\Gamma_{\text{PRS}}|^2. \quad (3.16)$$

The magnetic field, that dashes against the PRS, is defined as:

$$H_x^{\text{TX}} = \sqrt{\xi_r} \sqrt{\frac{2U^{\text{TX}}}{Z_0 r^2}} e^{j\phi^{\text{TX}}}. \quad (3.17)$$

Where $\xi_r \equiv \sqrt{\varepsilon_r/\mu_r}$. The ϕ^{TX} term takes into account the plane wave phase change through the PRS. The magnetic field then bounces in the cavity and so, the total one at the magnetic dipole location is:

$$H_x(0) = 2H_x^{TX} e^{-jk_{z1}h} \left(\frac{1}{1 + \Gamma_{PRS}} e^{-j2k_{z1}h} \right). \quad (3.18)$$

By combining Eq. (3.15) and (3.18):

$$H_x(0) = 2\sqrt{\zeta_r} \sqrt{\frac{2U^{inc}}{Z_0 r^2}} e^{j(\phi^{TX} - k_{z1}h)} \left(\frac{\sqrt{(1 - |\Gamma_{PRS}|^2)}}{1 + \Gamma_{PRS} e^{-j2k_{z1}h}} \right). \quad (3.19)$$

By inserting Eq. (3.19) in (3.10), the electric field results to be:

$$E_y(r) = -\frac{2M_m \sqrt{\zeta_r}}{M_e} \sqrt{\frac{2U^{inc}}{Z_0 r^2}} e^{j(\phi^{TX} - k_{z1}h)} \left(\frac{\sqrt{(1 - |\Gamma_{PRS}|^2)}}{1 + \Gamma_{PRS} e^{-j2k_{z1}h}} \right). \quad (3.20)$$

The resulting radiation at broadside, with Eq. (3.14) and (3.20), is given by:

$$U(\omega, \theta) = \frac{|E_y|^2}{2Z_0} r^2 = \frac{2\zeta_r}{Z_0^3} |E_0|^2 |M_m|^2 \frac{(1 - |\Gamma_{PRS}|^2)}{|1 + \Gamma_{PRS} e^{-j2k_{z1}h}|^2}. \quad (3.21)$$

Then, remembering that $\Gamma_{PRS} = |\Gamma_{PRS}| e^{j\phi_{PRS}}$ and considering $U^+ = \frac{2|E_0|^2 \zeta_r^2 |M_m|^2}{Z_0^3}$, Eq. (3.21) will become:

$$\begin{aligned} U(\omega, \theta) &= \frac{2\zeta_r |E_0|^2 |M_m|^2}{Z_0^3} \frac{(1 - |\Gamma_{PRS}|^2)}{|1 + \Gamma_{PRS} e^{-j2k_{z1}h}|^2}, \\ \longrightarrow U(\omega, \theta) &= \frac{U^+}{\zeta_r} \frac{1 - |\Gamma_{PRS}|^2}{|1 + |\Gamma_{PRS}| e^{j(\Phi_{PRS} - 2k_{z1}h)}|^2}, \\ \longrightarrow U(\omega, \theta) &= \frac{U^+}{\zeta_r} \frac{1 - |\Gamma_{PRS}|^2}{|1 - |\Gamma_{PRS}| e^{j(\Phi_{PRS} - 2k_{z1}h)} e^{-\pi}|^2}, \\ \longrightarrow U(\omega, \theta) &= \frac{U^+}{\zeta_r} \frac{1 - |\Gamma_{PRS}|^2}{|1 - |\Gamma_{PRS}| e^{j(\Phi_{PRS} - 2k_{z1}h - \pi)}|^2}. \end{aligned} \quad (3.22)$$

An equivalent formula can be obtained also by using TEN. In Fig. 3.6 the values of Y_{up} and Y_{down} , whose derivations are presented in Appendix B, are:

$$Y_{up} = Y_0(\hat{g} + j\hat{b}) \quad \text{and} \quad Y_{down} = -j\zeta_r Y_0 \cot(k_{z1}h),$$

where $Y_0 \equiv 1/Z_0 = \sqrt{\epsilon_0/\mu_0}$, $\hat{g} = g/Y_0$ and $\hat{b} = b/Y_0$. With these information, Γ_{PRS} can be written as:

$$\Gamma_{PRS} = \frac{1 - \left(\frac{g}{Y_1} + j\frac{b}{Y_1}\right)}{1 + \left(\frac{g}{Y_1} + j\frac{b}{Y_1}\right)} = \frac{1 - \left(\frac{g}{\zeta_r Y_0} + j\frac{b}{\zeta_r Y_0}\right)}{1 + \left(\frac{g}{\zeta_r Y_0} + j\frac{b}{\zeta_r Y_0}\right)} = \frac{\zeta_r - (\hat{g} + j\hat{b})}{\zeta_r + (\hat{g} + j\hat{b})}. \quad (3.23)$$

By combining Eq. (3.22) and (3.23), taking into account the following geometrical relationships $e^{\pm jx} = \cos(x) \pm j\sin(x)$, $\cos(2x) = \cos^2(x) - \sin^2(x)$ and $\sin(2x) = 2\sin(x)\cos(x)$, the radiation intensity is:

$$U(\omega, \theta) = \frac{U^+}{\sin^2(k_{z1}h)} \frac{\hat{g}}{\left|\zeta_r \cot(k_{z1}h) - \hat{b} + j\hat{g}\right|^2}. \quad (3.24)$$

3.3.1.2 Cavity height evaluation

The condition of maximum power at broadside allows to evaluate the cavity height value by knowing the PRS reflection coefficient phase [25].

$$\phi_{PRS}(\theta = 0^\circ) = 2k_{z1}h + \pi(2n - 1), \quad n = 0, \pm 1, \pm 2 \dots \quad (3.25)$$

This relation, obtained by using the ray tracing model, gives a direct connection between the PRS reflection phase and frequency. Usually, FPC antennas are narrow-band because Eq. (3.6) is satisfied for a single frequency. The phase $\phi_{PRS}(\omega)$ should be a monotonic function, in accordance with Foster's theorem, for a lossless load. However, the PRS is lossy because of the radiation of top of it, and for this reason there is a variation of the phase derivative vs. frequency. Usually this derivative is negative and the phase decreases with respect to frequency. On the other hand, k_{z1} increases making possible to satisfy Eq. (3.6) only at one frequency. In order to obtain a wide-band operation, the PRS reflection phase has to closely satisfy the resonance condition over a wide-band frequency region for a given cavity height at broadside, $\theta = 0^\circ$:

$$\phi_{PRS}(\omega) = 2k_{z1}h + \pi(2n - 1), \quad n = 0, \pm 1, \pm 2 \dots \quad (3.26)$$

Then the cavity height will be expressed as:

$$h = \frac{1}{2k_0\sqrt{\mu_r\epsilon_r}} [\phi_{PRS}(\omega) - \pi(2n - 1)], \quad n = 0, \pm 1, \pm 2 \dots \quad (3.27)$$

The resonance condition can be satisfied in a frequency range if the phase ϕ_{PRS} does not follow the typical Foster-like frequency dependence, $\partial\phi_{PRS}/\partial\omega < 0$, but it shows a phase increase within the bandwidth of operation. This phase response is possible since the structure radiates acting like as a loss mechanism for the cavity resonator.

So, the choice of optimum PRS reflection properties allows a cavity resonant condition for a wider frequency band and in this way a wider radiated power bandwidth can be obtained. The optimized PRS exhibits a positive slope in the plot of reflection phase vs. frequency in the band of interest while the magnitude shows a depth. Moreover, the PRS reflection coefficient has to be chosen in order to avoid a splitting of the wide-band response into a narrow multi-band one.

3.3.1.3 Attenuation and propagation constant

The radiation intensity formula can be expressed also by using the leaky wave parameters β and α by linking them to the PRS admittance variables, g and b , and to the PRS complex reflection coefficient, $|\Gamma_{PRS}|$ and ϕ_{PRS} .

Longitudinal wave-numbers in both cavity and air can be normalized with respect to k_0 and defined with this notation $\hat{k}_{z0} = k_{z0}/k_0$ and $\hat{k}_{z1} = k_{z1}/k_0$:

$$\hat{k}_{z0} = \hat{\beta}_{z0} - j\hat{\alpha}_{z0} = \sqrt{1 - \hat{k}_\rho^2}, \quad (3.28)$$

$$\hat{k}_{z1} = \hat{\beta}_{z1} - j\hat{\alpha}_{z1} = \sqrt{\mu_r \epsilon_r - \hat{k}_\rho^2}, \quad (3.29)$$

where the transverse wave-number is normalized too:

$$\hat{k}_\rho \equiv \frac{k_\rho}{k_0} = \frac{\beta}{k_0} - j\frac{\alpha}{k_0} = \hat{\beta} - j\hat{\alpha}. \quad (3.30)$$

By considering the maximum radiation in broadside region, where $\hat{\alpha} \ll 1$ and $\hat{\beta} \ll 1$, Eq. (3.28) and (3.29) can be approximated as:

$$\begin{aligned} \hat{\beta}_{z0} &\simeq \frac{\hat{\alpha}^2 - \hat{\beta}^2 + 2}{2}, \\ \hat{\alpha}_{z0} &\simeq -\hat{\alpha}\hat{\beta}, \end{aligned} \quad (3.31)$$

$$\begin{aligned} \hat{\beta}_{z1} &\simeq \frac{\hat{\alpha}^2 - \hat{\beta}^2 + 2n_1^2}{2n_1}, \\ \hat{\alpha}_{z1} &\simeq -\frac{\hat{\alpha}\hat{\beta}}{n_1}, \end{aligned} \quad (3.32)$$

where $n_1 = \sqrt{\epsilon_r \mu_r}$. The TEN model allows to relate the transverse wave-number \hat{k}_ρ with frequency at point $z = h$ for the dominant leaky mode:

$$Y_{tot}^{TE/TM}(k_\rho) = Y_{up}^{TE/TM}(k_\rho) + Y_{down}^{TE/TM}(k_\rho) = 0, \quad (3.33)$$

where

$$Y_{up}(k_\rho) = Y_1 \frac{1 - \Gamma_{PRS}}{1 + \Gamma_{PRS}} \quad \text{and} \quad Y_{down}(k_\rho) = Y_1 \frac{1 + e^{-j2k_{z1}h}}{1 - e^{-j2k_{z1}h}}. \quad (3.34)$$

The reflection coefficient can be evaluated by using the leaky wave parameters; combining Eq. (3.34) in (3.33):

$$|\Gamma_{PRS}| = e^{-2|\hat{\alpha}_{z1}|k_0h}, \quad (3.35)$$

$$\phi_{PRS} = 2\hat{\beta}_{z1}k_0h + \pi(2n - 1), \quad n = 0, \pm 1, \pm 2 \dots \quad (3.36)$$

From Eq. (3.35) and (3.36) the leaky wave parameter can be express in terms of the PRS reflection coefficient variables:

$$\hat{\alpha} = \frac{n_1}{2k_0h} \frac{-\ln |\Gamma_{PRS}|}{\hat{\beta}}, \quad (3.37)$$

$$\hat{\beta} = \sqrt{\frac{n_1}{2k_0h} (\sqrt{\Phi^2 + \ln^2 |\Gamma_{PRS}|} - \Phi)}, \quad (3.38)$$

where Φ represents the total phase change of the wave as sum of all the phase changes caused by the reflections between ground plane and PRS.

$$\Phi = \phi_{PRS} - \pi(2n - 1) - 2n_1k_0h \quad n = 0, \pm 1, \pm 2 \dots \quad (3.39)$$

The admittance Y_{up} is related to the PRS reflection coefficient:

$$Y_{up}^{TE/TM} = Y_0^{TE/TM}(\hat{g} + j\hat{b}) = Y_1^{TE/TM} \frac{1 - \Gamma_{PRS}}{1 + \Gamma_{PRS}}. \quad (3.40)$$

If the transmission lines admittances have a negligible variation with respect to frequency compared with the Γ_{PRS} around the resonant one, they can be considered frequency independent and their ratio almost fixed $Y_1^{TE/TM}/Y_0^{TE/TM} \approx \zeta_r$. By combining Eq. (3.35) and (3.36) in (3.40), \hat{Y}_{up} can be expressed as:

$$\hat{Y}_{up} = \hat{g} + j\hat{b} = \zeta_r \frac{\sinh(2\hat{\alpha}_{z1}k_0h) - j \sin(2\hat{\beta}_{z1}k_0h)}{\cos(2\hat{\beta}_{z1}k_0h) - \cosh(2\hat{\alpha}_{z1}k_0h)}. \quad (3.41)$$

To obtain Eq. (3.32), $\hat{\alpha} \ll 1$ and $\hat{\beta} \ll 1$ have been considered and this led to $\hat{\alpha}_{z1} \ll 1$ and $\hat{\beta}_{z1} \ll 1$. Therefore, Eq. (3.42) can be approximated due to the small trigonometric function arguments:

$$\hat{Y}_{up} = \hat{g} + j\hat{b} \simeq \zeta_r \frac{-\hat{\alpha}_{z1}k_0h + j(\hat{\beta}_{z1}k_0h - \pi)}{(\hat{\alpha}_{z1}k_0h)^2 + (\pi - \hat{\beta}_{z1}k_0h)^2}. \quad (3.42)$$

From Eq. (3.32) and (3.43) another relationship between the PRS conductance or susceptance and the wave-number of the leaky mode can be written:

$$\hat{g} \simeq \frac{\hat{\alpha}\hat{\beta}_r n_1 k_0 h}{(\hat{\alpha}\hat{\beta} k_0 h)^2 + (2\pi n_1 - (\hat{\alpha}^2 - \hat{\beta}^2 + 2n_1^2) k_0 h)^2 / 4}, \quad (3.43)$$

$$\hat{b} \simeq \frac{\xi_r n_1 ((\hat{\alpha}^2 - \hat{\beta}^2 + 2n_1^2) k_0 h - 2\pi n_1) / 2}{(\hat{\alpha}\hat{\beta} k_0 h)^2 + (2\pi n_1 - (\hat{\alpha}^2 - \hat{\beta}^2 + 2n_1^2) k_0 h)^2 / 4}. \quad (3.44)$$

Starting from this link between the admittances and the propagation and attenuation constants, the radiation intensity formula can be rewritten. Starting from Eq. (3.24), after some manipulation with Taylor series expansions for trigonometric functions:

$$U(\omega, \theta) \simeq \frac{U^+}{(k_{z1}h - \pi)^2} \left(\frac{\hat{g}}{\hat{g}^2 + \left(\hat{b} - \xi_r / (k_{z1}h - \pi) \right)^2} \right), \quad (3.45)$$

where $\sin(k_{z1}h) \simeq -(k_{z1}h - \pi)$, $\cot(k_{z1}h) \simeq 1 / (k_{z1}h - \pi)$ and $k_{z1} \simeq k_0 (n_1 - (\sin^2 \theta) / (2n_1))$. By using Eq. (3.43) and (3.44) in (3.45), the radiation intensity formula in function of $\hat{\alpha}$ and $\hat{\beta}$ is obtained:

$$U(\omega, \theta) = \frac{4n_1}{\xi_r k_0 h} \left(\frac{\hat{\alpha}\hat{\beta}}{4\hat{\alpha}^2\hat{\beta}^2 + (\hat{\alpha}^2 - \hat{\beta}^2 + \sin^2 \theta)^2} \right). \quad (3.46)$$

SOURCES

As introduced in the previous section, various radiating sources can be used to excite the PRS structure such as dipoles, slots or patches. In this chapter, a briefly introduction on these last two type of sources is proposed with a particular attention on their design formulas.

4.1 SLOT ANTENNA

These kind of antennas consists of a flat metal surface with one or multiple holes on it. They are quite popular because they can be cut out of whatever surface they are to be mounted on. Moreover, they have a radiation pattern that is roughly omnidirectional.

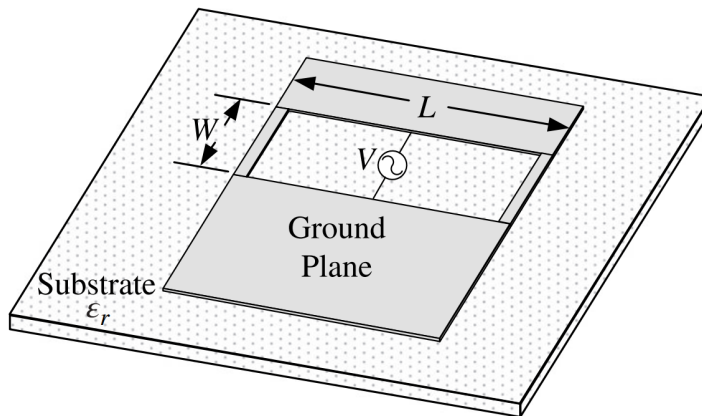


Figure 4.1: Example of slot antenna with voltage excitation. (Fig. 14-49 of [10])

To radiate properly, the slot length should be around half a wavelength:

$$L \approx \frac{\lambda_0}{2}. \quad (4.1)$$

While the width typically should be:

$$W \leq (0.05 - 0.1)\lambda_0. \quad (4.2)$$

The radiation pattern depends on the type of feeding together with the conductive plane geometry on which the slot is placed. This happens because the radiation mainly contribution is the current flowing on this conducting plane. However, if this plane is large enough compared with the wavelength, the slot radiation pattern is determined only by the its geometry and feeding. The slot input impedance can be obtained from the following equation:

$$Z_s Z_c = \frac{Z_0^2}{4}, \quad (4.3)$$

where Z_s is the slot input impedance, Z_c is the dipole one and Z_0 is characteristic impedance of free space. This relation comes from the Babinet's principle together with its extension proposed by Booker [10, 33, 34]. They showed that a rectangular slot antenna with dimensions L and W is complementary to a planar dipole antenna with the same geometry, Fig. 4.2.

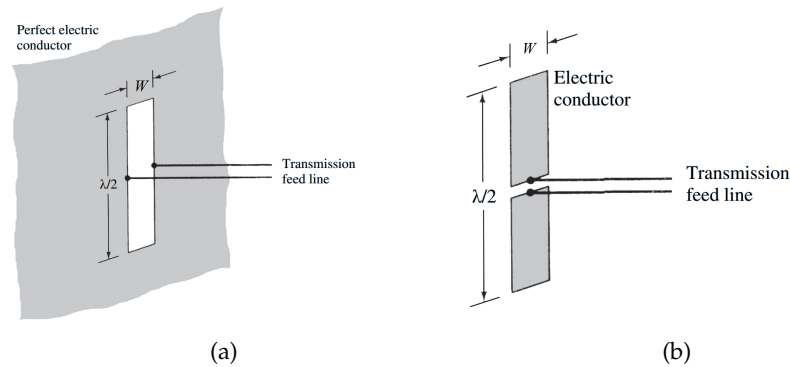


Figure 4.2: Half wavelength slot and complementary flat dipole. (Fig. 12-24 of [10])

4.2 PATCH ANTENNA

These kind of antennas consists in a metal sheet of various shape on a grounded substrate that can be fed for example through a microstrip line, Fig. 4.3.

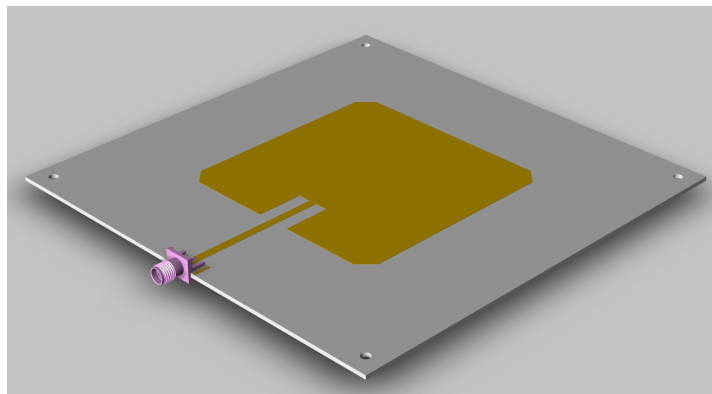


Figure 4.3: Example of an inset fed Patch antenna. This kind of feeding allows to have a better control on the impedance matching instead of attaching the transmission line to the patch edge. (From public domain)

They are low profile and they can easily be printed and then integrated on the board with the rest of the circuit. Moreover, they are

inexpensive to manufacture and, when mounted on a rigid surface, they are mechanically robust [10]. Patch antennas are hardly used combined together on the same substrate to make high gain or phased arrays and the final structure still remains not expensive to fabricate. Although they are low efficient and narrow band, this problems can be overcome with particular designs.

The patch can be seen as two magnetic dipole that radiate in phase:

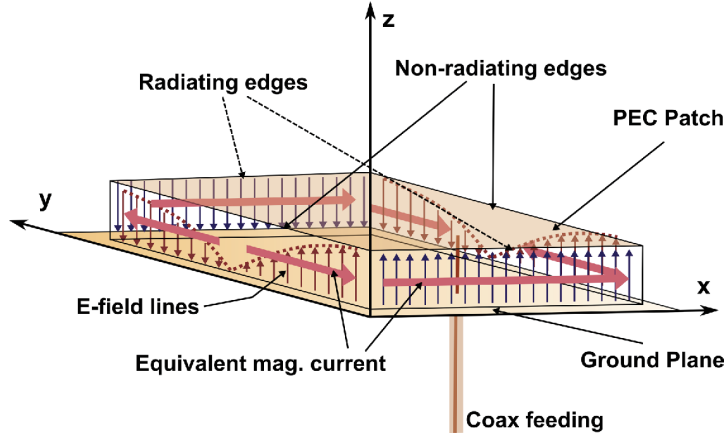


Figure 4.4: Resonant cavity model of the patch. (Fig. 1 of [35])

4.2.1 Design

For an efficient radiator, a practical width that leads to good radiation efficiencies can be obtain from the following expression:

$$W = W_{opt} = \frac{c}{2f_r} \sqrt{\frac{2}{\epsilon_r + 1}}, \quad (4.4)$$

where f_r is the resonant frequency of interest. By computing W in Eq. (4.5), the effective dielectric constant can be then valuated by:

$$\epsilon_{r,eff} = \frac{\epsilon_r + 1}{2} + \frac{\epsilon_r - 1}{2} \left[1 + 12 \frac{h}{W} \right]^{-1/2}, \quad (4.5)$$

where h is the dielectric substrate height. Due to the fringing effect, the patch dimension along the E-plane is extended by a value ΔL , whose practical and common relation is:

$$\frac{\Delta L}{h} = 0.412 \frac{(\epsilon_{r,eff} + 0.3) \left(\frac{W}{h} + 0.264 \right)}{(\epsilon_{r,eff} - 0.258) \left(\frac{W}{h} + 0.8 \right)}. \quad (4.6)$$

Since the patch length has been extended by ΔL on both side, the effective length of the patch can be defined as:

$$L = L_{eff} - 2\Delta L, \quad (4.7)$$

where $L_{eff} = \frac{\lambda_g}{2}$ and $\lambda_g = \frac{\lambda_0}{\sqrt{\epsilon_{r,eff}}} = \frac{c}{f_r \sqrt{\epsilon_{r,eff}}}$.

4.2.2 Input impedance and feeding location

Through the patch equivalent circuit obtained by using the TL model, the patch input impedance can be evaluated. The conductances represent the two magnetic dipoles, while the presence of capacitors is due to the fringing field effect, Fig. 4.5.

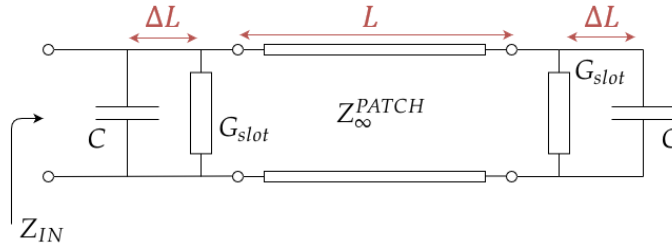


Figure 4.5: Patch equivalent circuit considering the magnetic dipole conductances G_{slot} and the electric extension due to fringing field effect modeled by two C .

The value of Z_{∞}^{PATCH} can be evaluated from the microstrip line formula where the width considered is the patch one:

$$Z_{\infty}^{PATCH} = \begin{cases} \frac{60}{\sqrt{\epsilon_{r,eff}}} \ln \left[\frac{8h}{W} + \frac{W}{4h} \right], & \frac{W}{h} \leq 1 \\ \frac{120\pi}{\sqrt{\epsilon_{r,eff}} \left[\frac{W}{h} + 1.393 + 0.667 \ln \left(\frac{W}{h} + 1.444 \right) \right]}, & \frac{W}{h} > 1 \end{cases} \quad (4.8)$$

The equivalent circuit after enlarging the patch to eliminate the fringing field effect will be without the capacitors:

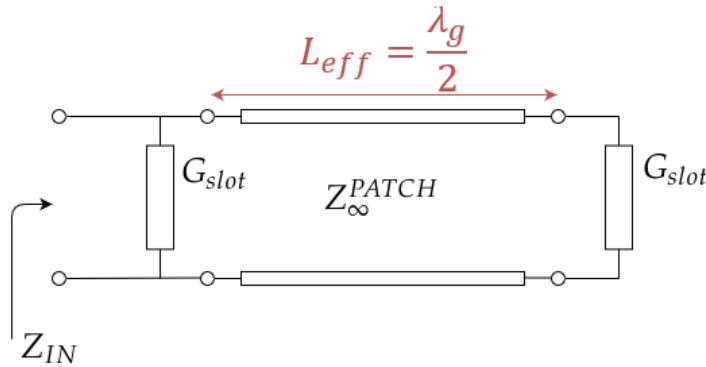


Figure 4.6: Patch TL model .

Because the two conductances are $\frac{\lambda_g}{2}$ spaced, moving toward generator on the Smith Chart means that the right G_{slot} remains unchanged. So the equivalent circuit is:

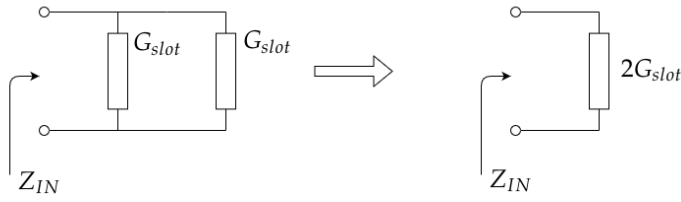


Figure 4.7: Patch equivalent circuit after applying transmission line theory. The input impedance is related to the sum of the two magnetic dipoles conductances.

The input impedance will then be:

$$Z_{IN} = \frac{1}{2G_{slot}}, \tag{4.9}$$

where the conductance is defined:

$$G_{slot} = \frac{W}{120\lambda_0} \left[1 - \frac{1}{24} \left(2\pi \frac{h}{\lambda_0} \right)^2 \right]. \tag{4.10}$$

The capacitors, on the other hand, can be evaluated with the following expression:

$$C = \frac{W}{120\lambda_0} \left[1 - 0,636 \ln \left(2\pi \frac{h}{\lambda_0} \right) \right]. \tag{4.11}$$

In this way, however, Z_{IN} can be sometimes too high. To have a better control on the input impedance, the insert fed solution can be used. It can be implemented by choosing the point for the coaxial cable pin or by inserting a microstrip line in the patch at a particular location, Fig. 4.8.

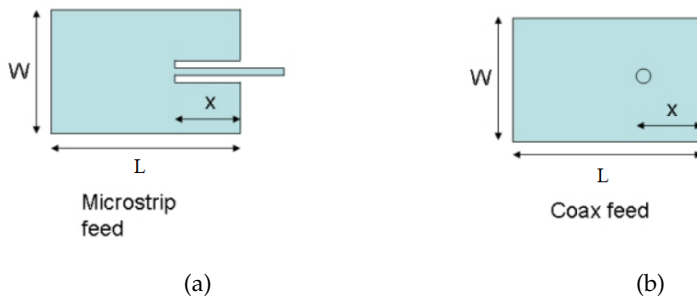


Figure 4.8: The microstrip patch feeding can be done by doing a recess feeding, (a), or with a coax feed, (b).

By looking at the antenna equivalent circuit, at distance x_0 the input impedance is smaller than before and it is be equal to the feeding line characteristic impedance. This time the slot will be considered having a complex impedance Z_{slot} .

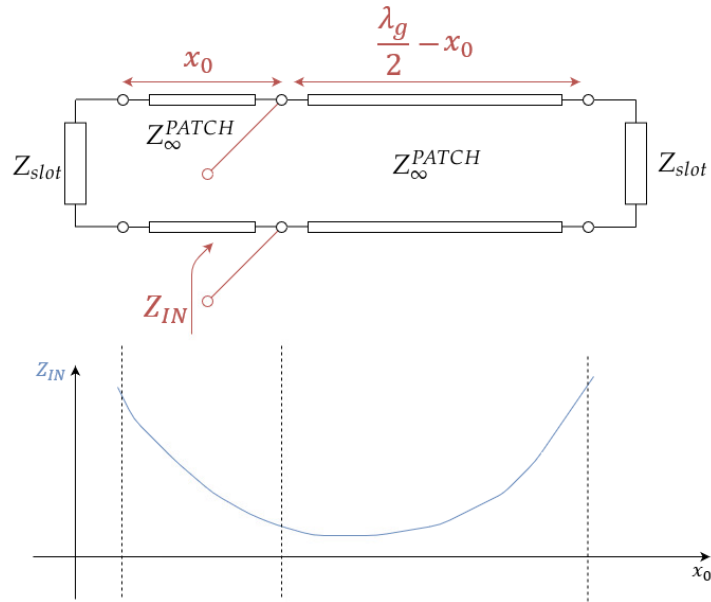


Figure 4.9: TL model can be used to find the position x_0 for the feeding line. By varying the value of x_0 , as shown in the bottom part of the figure, the input impedance will change and it can match the feeding line impedance.

The input impedance Z_{IN} is always real because, looking at the Smith Chart, the first normalized slot impedance move along a circle toward generator by a length kx_0 while the other one by $k(\lambda_g/2 - x_0)$ that is complementary. By solving the equivalent circuit using the transmission line basic formulas, the distance x_0 is:

$$x_0 = \frac{L}{\pi} [\cos^{-2} (Z_{IN} 2G_{slot})] . \quad (4.12)$$

Part III

SIMULATIONS

UNIT CELL DESIGN

In this chapter various solutions for the basic PRS unit cell are proposed. After a comparison between all cases, the best result is chosen considering the best trade off between a wide bandwidth and a higher gain. As mentioned in Chapter 3, the PRS can be excited easily by a slot on the ground plane that is modeled as an equivalent magnetic current. In this way too, due to the fact WR42 wave-guides are available in the laboratory and one goal is to test the antenna after fabrication, the frequency range chosen for the structure is 18 – 28GHz.

5.1 UNIT CELL GEOMETRY SOLUTIONS

Different geometries for the unit cell have been explored in order to find the right unit cell parameters that allow to obtain a wider radiated power bandwidth, Fig. 5.1.

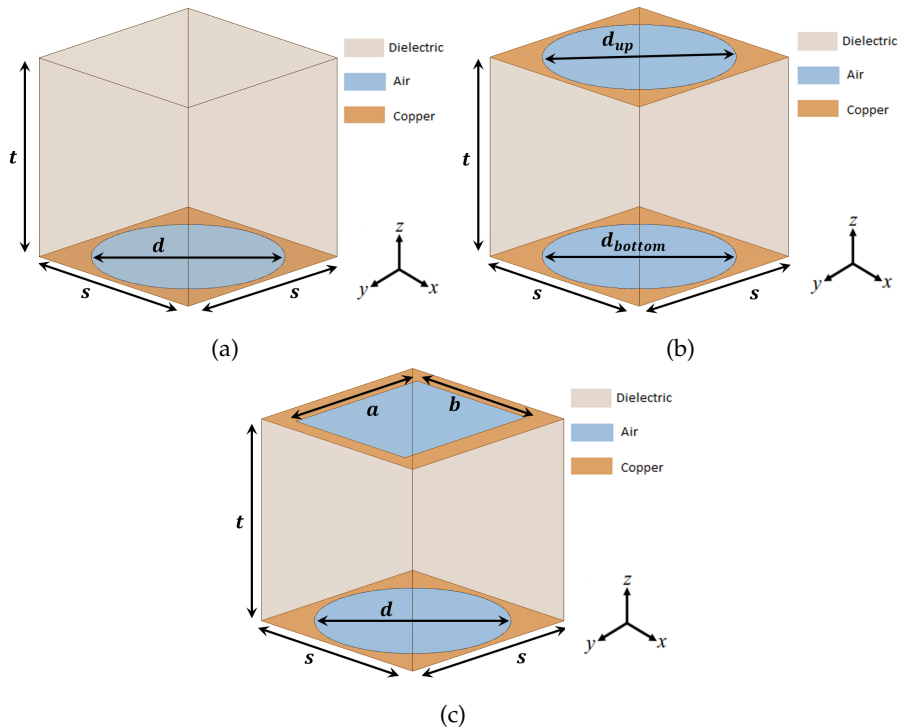


Figure 5.1: In (a) the unit cell of a periodic PRS is composed by a dielectric layer over a periodically copper sheet patterned with circular holes. In (b) and (c), a copper slab is also added on top of the dielectric with circular or rectangular holes respectively.

A cubic unit cell is shown in Fig. 5.1a. It has lateral side s , dielectric layer thickness t and a copper sheet on the bottom patterned with a circular hole of diameter d . However, the dielectric thickness t is constrained by the manufacturer available samples as discussed in Appendix C, D and E. More degree of freedom can be added to the PRS unit cell by putting a copper slab on top of it. In Fig. 5.1b, the upper copper sheet is patterned by a circular hole of diameter d_{up} that can be equal or not to the diameter d_{bottom} of the bottom circular hole. Another solution, proposed in Fig. 5.1c, uses a rectangular hole on top with dimensions a and b .

5.1.1 PRS reflection coefficient comparison

Starting from the three unit cell geometries described before, the reflection coefficient magnitude and phase have been investigated for different dielectric materials. The reflection coefficient knowledge is necessary to find the resonance cavity height as defined in Eq. (3.27). The magnitude and phase of Γ_{PRS} , due to a normally incident plane wave dashing against the PRS at $\theta = 0^\circ$, have been simulated. The best solutions, between the dielectric materials presented in Appendix C, are reported as follows:

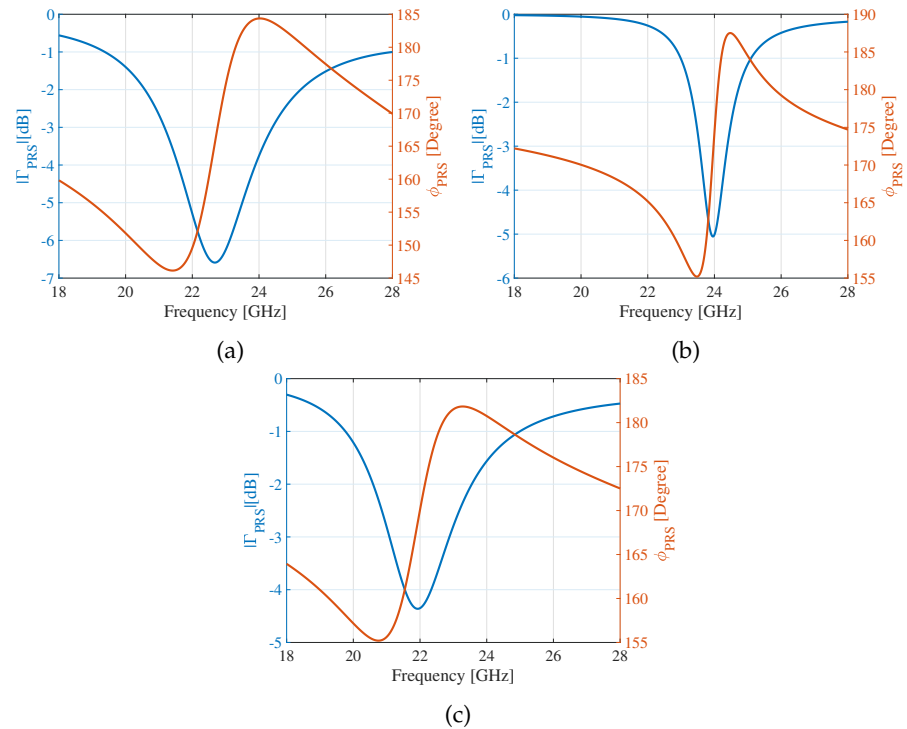


Figure 5.2: PRS reflection coefficient magnitude and phase related to the geometries, shown in Fig. 5.1, are presented. (a) uses RO3010 dielectric with a geometry shown in Fig. 5.1a. (b) is related to TMM10i dielectric whose geometry is in Fig. 5.1b. (c) is obtained from RO3210 and the geometry employed is shown in Fig. 5.1c.

Fig. 5.1a is related to the single circular hole structure whose dielectric material is RO3010. The unit cell parameters are: $s = 2.5\text{mm}$, $t = 2.56\text{mm}$ and $d = 2.3\text{mm}$. The positive slope of ϕ_{PRS} , combined with a wide magnitude reflection coefficient depth, is the main cause of a wide-band operation as shown in Fig. 5.4a.

For the RO3210 case, Fig. 5.1b, that considers a geometry with a circular and rectangular holes, the considerations are analogous. In this case the unit cell parameters are: $s = 1.5\text{mm}$, $t = 1.28\text{mm}$, $d = 1.4\text{mm}$ and $a = b = 1.4\text{mm}$.

The unit cell geometry with two circular holes uses TMM10i as dielectric substrate and its reflection coefficient behavior is showed in Fig. 5.1c. In this case, ϕ_{PRS} presents a steep slope in the interested frequency range and $|\Gamma_{PRS}|$ a deeper drop that are the main reason of high gain but narrow power radiated bandwidth as shown in Fig. 5.4b.

5.1.2 PRS resonance height comparison

The reflection coefficient magnitude and phase values obtained previously by full wave simulation, have been used in Eq. (3.27) to compute the resonance cavity height:

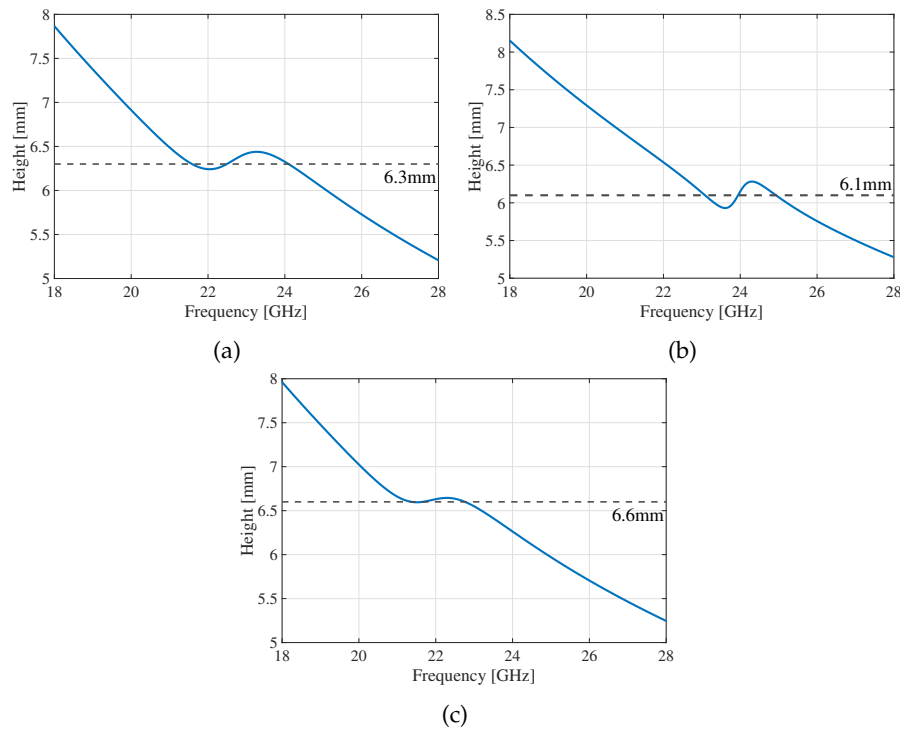


Figure 5.3: PRS cavity heights related to the geometries shown in Fig. 5.1 are presented. In (a) the substrate used is RO3010, while the geometry is shown in Fig. 5.1a. (b) is related to TMM10i dielectric whose geometry is in Fig. 5.1b. (c) is obtained from RO3210 and the geometry employed is shown in Fig. 5.1c.

For each of these curves, a value that is more or less constant with respect to frequency has been chosen. This value is the center of non-Foster region, as explained in Chapter 3, which means that choosing a fixed height may lead to wide-band operation. In the RO3010 case, the chosen cavity height is $h = 6.3\text{mm}$. On the other hand, for TMM10i and RO3210 $h = 6.3$ and $h = 6.6\text{mm}$, respectively.

5.1.3 Radiation intensity comparison

The radiated power bandwidth can be estimated by combining in Eq. (3.22) the cavity height values chosen previously with the simulated reflection coefficient magnitude and phase:

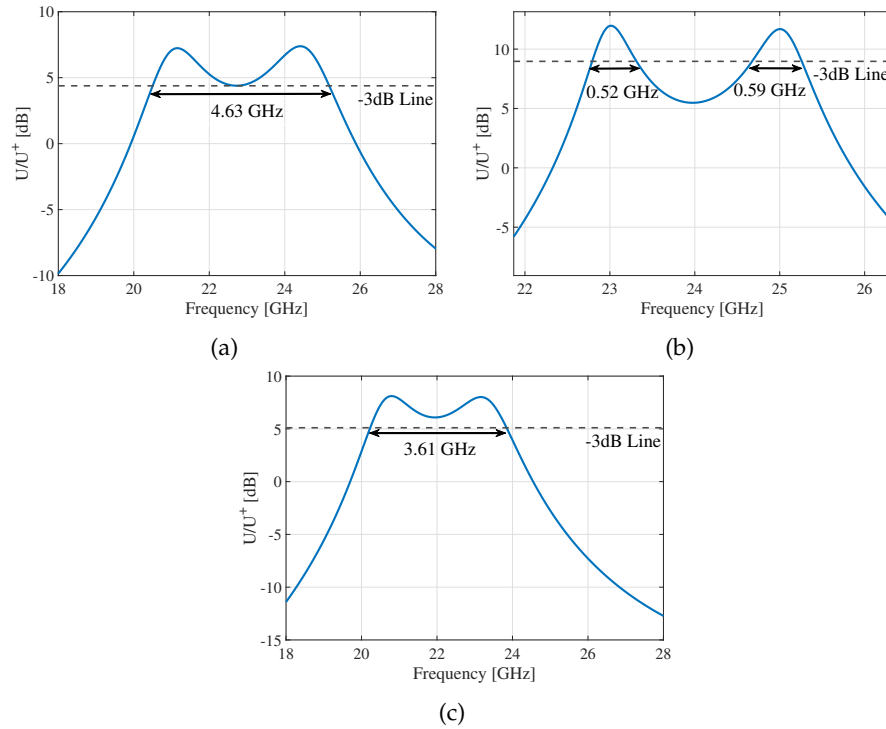


Figure 5.4: PRS radiation intensity graphs related to the geometries shown in Fig. 5.1 are presented. In (a) the substrate used is RO3010, while the geometry is shown in Fig. 5.1a. (b) is related to TMM10i dielectric whose geometry is in Fig. 5.1b. (c) is obtained from RO3210 and the geometry employed is shown in Fig. 5.1c.

Fig. 5.4a shows the best bandwidth value among the three cases: $BW = 4.63\text{GHz}$. The substrate used is RO3010 with a unit cell having a single circular hole. As already mentioned, the TMM10i case shows a really high gain but two narrow bandwidth due to the steep reflection coefficient phase slope.

5.2 PRS WITH CIRCULAR HOLE ON THE BOTTOM

Between the three PRS analyzed before, the one with a circular hole on the bottom and composed by a RO3010 dielectric substrate has shown the best solution in terms of gain and radiated power bandwidth, Fig. 5.5b. However, the chosen dielectric thickness is not available from the manufacturer, Appendix D. To obtain a thickness $t = 2.56\text{mm}$, two layer with $t = 1.28\text{mm}$ can be glued together.

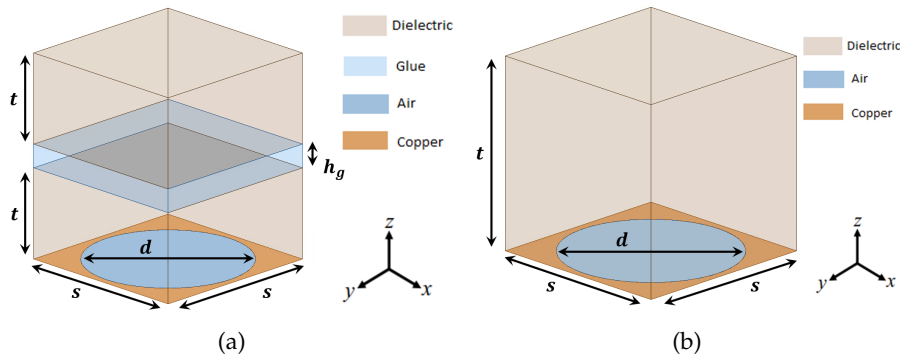


Figure 5.5: On the left, PRS unit cell geometry having a glue substrate of thickness h_g is shown. On the right, previously presented PRS unit cell with a hole in the bottom is showed.

However, this solution has to take care of the glue effects on the structure. A parametric simulation has been done changing the height of the glue thickness from $0\mu\text{m}$ to $100\mu\text{m}$ and considering in first case $\epsilon_r = 1$ and then $\epsilon_r = 3$. Using $\epsilon_r = 1$, it means that the dielectric layers are one above the other one with just a bit of glue on the corner: in the major part of the surface there is air between the two layers. In case $\epsilon_r = 3$, the glue is uniformly distributed along the two dielectric surfaces.

5.2.1 Reflection coefficient comparison

The reflection coefficient magnitude and phase variations due to the glue are reported in Fig. 5.6 and 5.7 respectively. If the glue has $\epsilon_r = 1$, the magnitude reflection coefficient shift down in frequency. If $\epsilon_r = 3$, the magnitude not only shift down in frequency but the drop increases also a bit. The phase, on the other hand, shows just a shifting down in frequency.

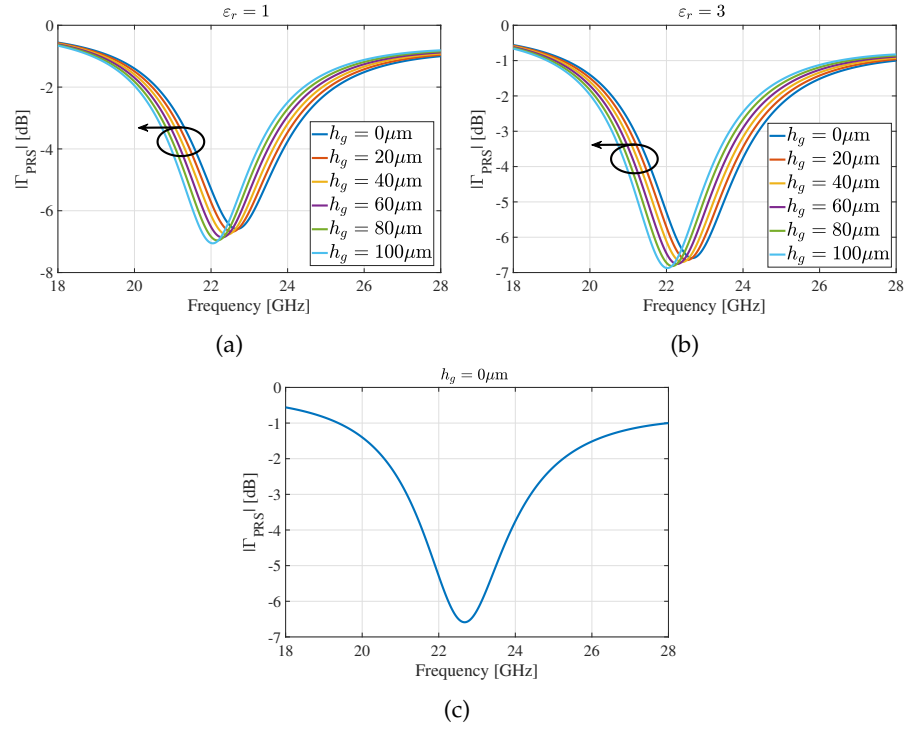


Figure 5.6: $|\Gamma_{PRS}|$ variation due to the glue with $\epsilon = 1$, in (a), then with $\epsilon = 3$, in (b), are reported. In (c) the case with $h_g = 0$ is considered.

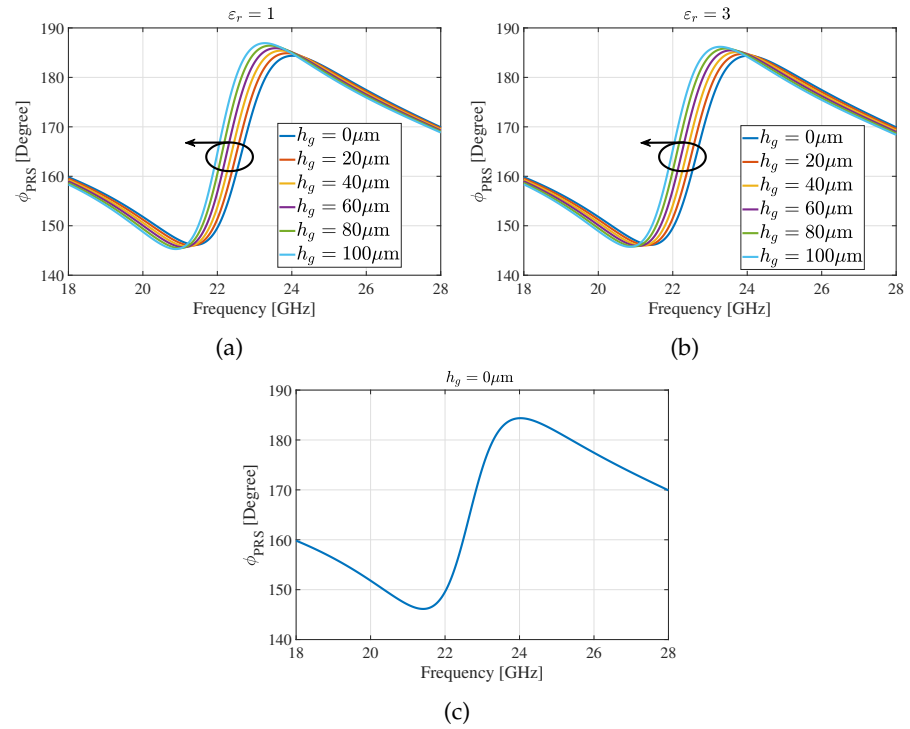


Figure 5.7: ϕ_{PRS} variation due to the glue with $\epsilon = 1$, in (a), then with $\epsilon = 3$, in (b), are reported. In (c) the case with $h_g = 0$ is considered.

5.2.2 Resonance height comparison

Either with $\epsilon_r = 1$ and $\epsilon_r = 3$, the cavity height graph shows more or less the same frequency shift.

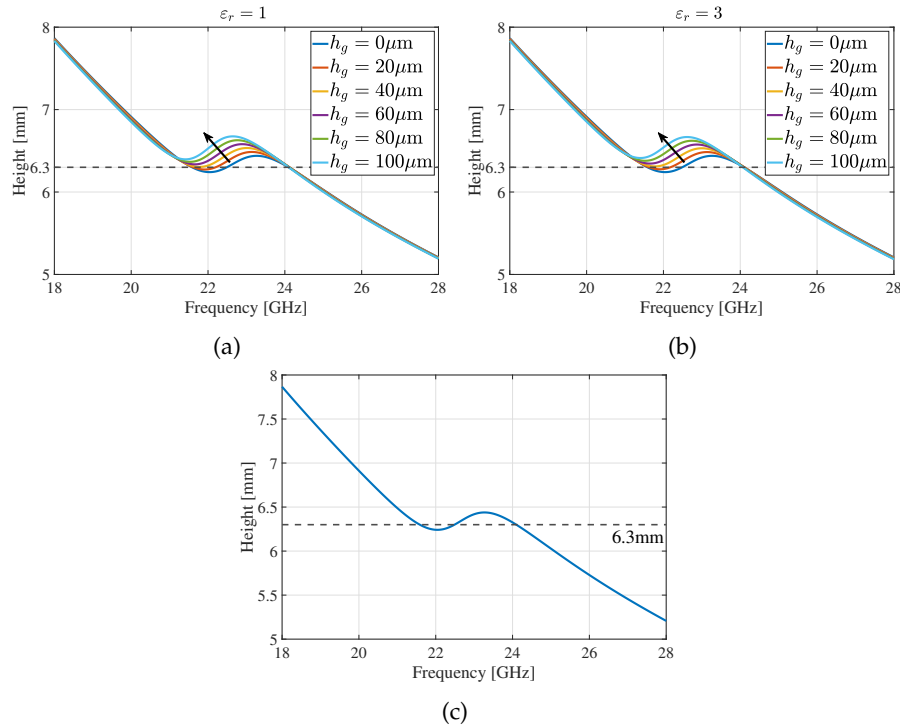


Figure 5.8: Cavity height variation due to the glue with $\epsilon = 1$, in (a), then with $\epsilon = 3$, in (b), are reported. In (c) the case with $h_g = 0$ is considered.

5.2.3 Radiation intensity comparison

The radiation intensity obtained by combining the values of reflection coefficient and cavity height in Eq. (3.22), shows different behaviors if the glue has $\epsilon = 1$ or $\epsilon = 3$. For $\epsilon = 1$, a variation in the glue thickness decreases a radiation intensity peak and increases the other one, Fig. 5.9a. By considering $\epsilon = 3$, a shift down in frequency, in addition to the peak variations, is present, Fig. 5.9b.

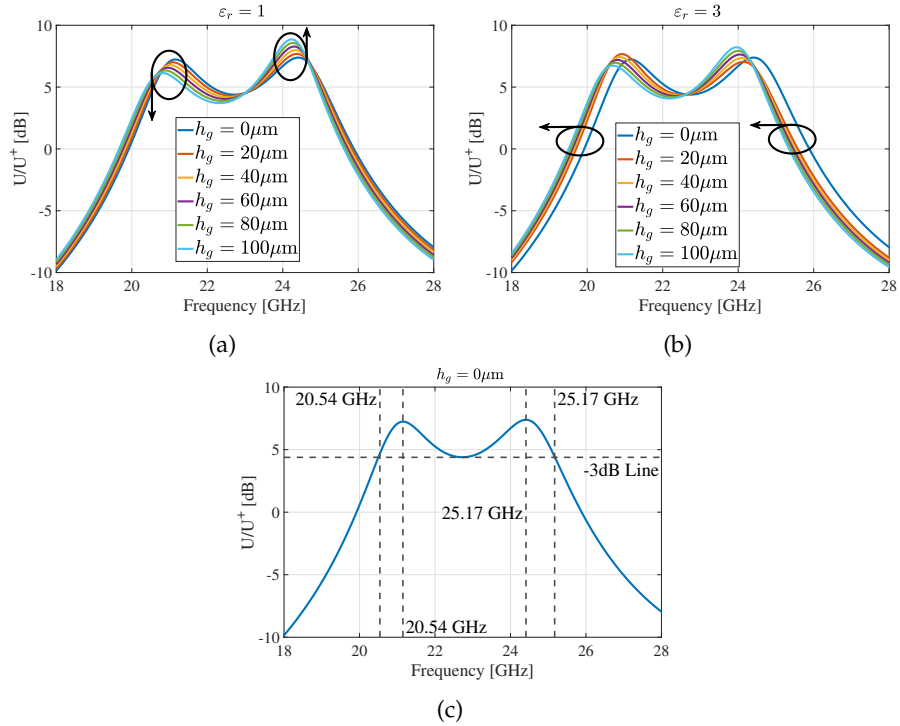


Figure 5.9: Radiation intensity variation due to the glue with $\epsilon = 1$, in (a), then with $\epsilon = 3$, in (b), are reported. In (c) the case with $h_g = 0$ is considered.

5.3 OPTIMIZED SOLUTION

Although the previous solution shows a really wide radiated power bandwidth, 4.63GHz, having two glued layers affects too much the PRS reflection coefficient and so the peaks in the radiated power intensity graph. For this reason, other investigations have been done and the following structure with just one layer of RO3010 has been obtained:

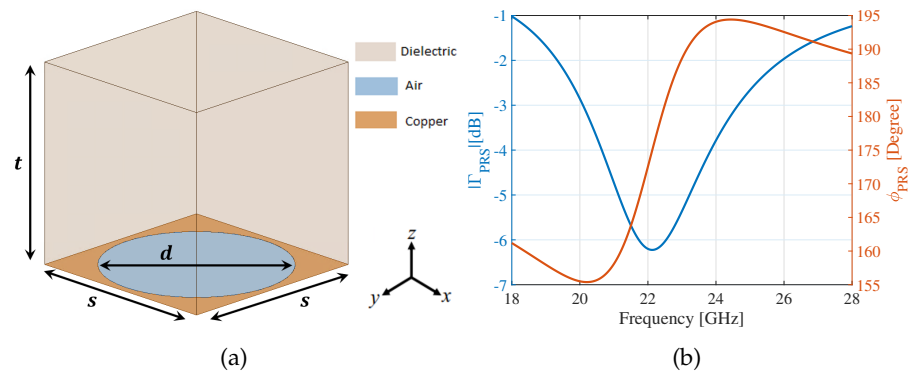


Figure 5.10: (a) shows the optimized PRS unit cell geometry using RO3010 as dielectric substrate. In (b) the reflection coefficient phase and magnitude are shown.

The unit cell, having $t = 0.64\text{mm}$, $s = 5\text{mm}$ and $d = 3.1\text{mm}$, shows the reflection coefficient behavior in Fig. 5.10. The value of the cavity height can be computed by using these values of magnitude and phase in Eq. (3.25):

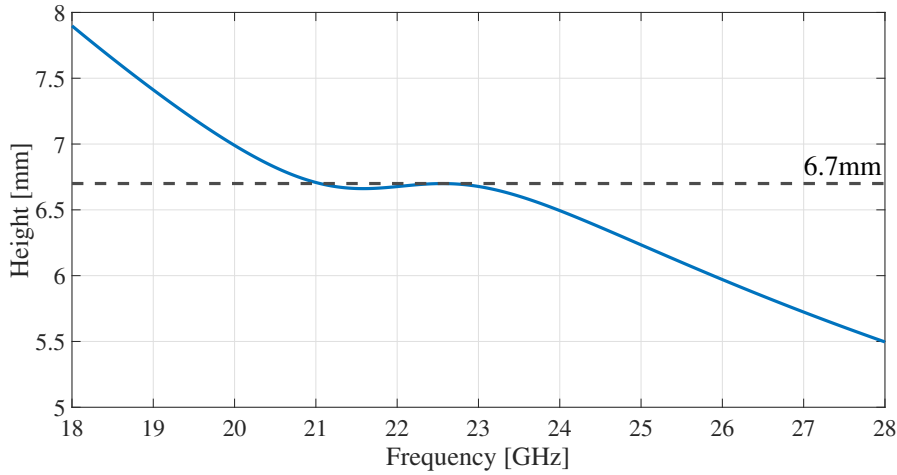


Figure 5.11: A fixed cavity height has to be chosen to obtain a wide-band operation. Choosing $h \approx 6.7\text{mm}$ ensures the height requirement in order to have the largest possible band.

In the region between 22 – 23GHz, the height is more or less constant with respect to frequency that is also at the center of non-Foster region which means that choosing a fixed height as 6.7mm may lead to wide-band operation.

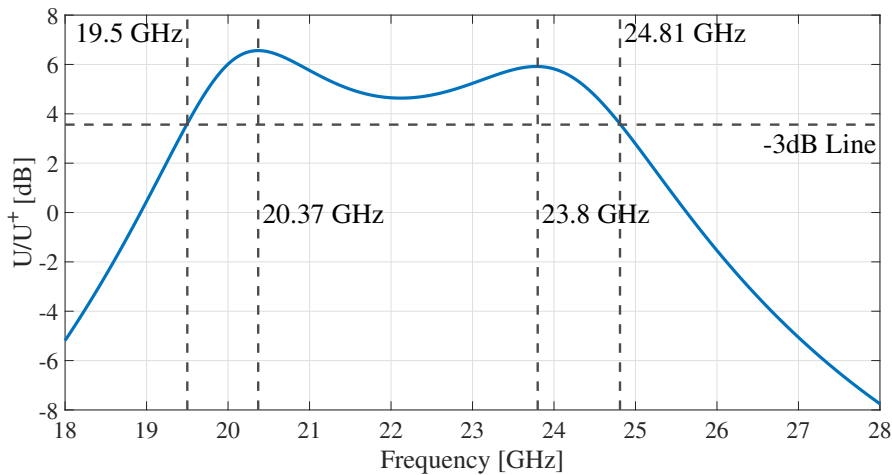


Figure 5.12: The radiation intensity graph for the proposed geometry is presented. It shows two peaks: one at 20.37GHz and one at 23.8GHz. The -3dB bandwidth is limited below by 19.5GHz and above by 24.81GHz.

From Fig. 5.12, it can be seen that the band is relatively wide: $BW = 24.81\text{GHz} - 19.95\text{GHz} = 5.31\text{GHz}$. At the peaks frequencies of 20.37GHz

and 23.8GHz the gain has the maximum values. By using the reflection coefficient magnitude and phase in Eq. 3.39, 3.38 and 3.37, the values of attention and propagation constant have been evaluated:

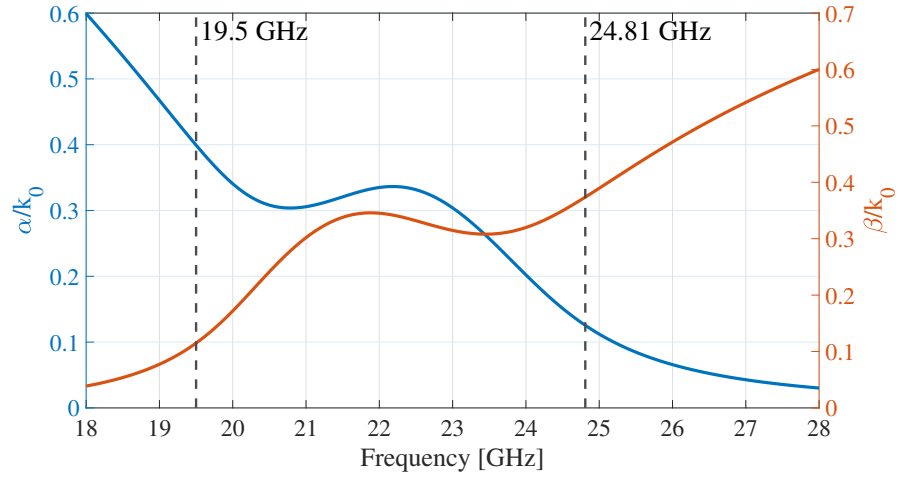


Figure 5.13: Dispersion diagram for the normalized leaky wave attenuation and propagation constants.

The values of α at the $-3dB$ bandwidth limits have been evaluated to find the truncated antenna length defined as distance from the feeding point to the FPC structure edge:

$$\alpha_{19.5 \text{ GHz}} = \hat{\alpha}_{19.5 \text{ GHz}} * k_0 = 163.63 \text{ [1/m]}, \quad (5.1)$$

$$\alpha_{24.81 \text{ GHz}} = \hat{\alpha}_{24.81 \text{ GHz}} * k_0 = 65.22 \text{ [1/m]}. \quad (5.2)$$

From this two results, the truncated length of the FPC antenna can be evaluated using Eq. (3.8):

$$R_{eff} = 1 - e^{-2\alpha L}, \quad (5.3)$$

where R_{eff} is the radiation efficiency, L is the truncated FPC antenna length and α is the attenuation constant. Considering $R_{eff} = 95\%$, the final length is:

$$\begin{aligned} R_{eff} - 1 &= -e^{-2\alpha L} \longrightarrow 0.05 = e^{-2\alpha L} \\ &\longrightarrow -2\alpha L = \ln(0.05) \\ &\longrightarrow L = \frac{-\ln(0.05)}{2\alpha}. \end{aligned}$$

So, the truncated length at $\alpha_{19.5 \text{ GHz}}$ is $L = 9.2\text{mm}$, while at $\alpha_{24.81 \text{ GHz}}$ is $L = 23\text{mm}$. Considering the greatest value of L in order to obtain a higher gain, the total dimension of the array is $46\text{mm} \times 46\text{mm}$ (because $2L = 46\text{mm}$). The unit cell length is 5mm so the final PRS layer is

composed by 10x10 unit cells.

On the other hand, considering $R_{eff} = 99\%$ the final length will be:

$$R_{eff} - 1 = -e^{-2\alpha L} \longrightarrow L = \frac{-\ln(0.01)}{2\alpha}.$$

The truncated length at $\alpha_{19.5 \text{ GHz}}$ is $L = 14.1\text{mm}$, while at $\alpha_{24.81 \text{ GHz}}$ is $L = 35.3\text{mm}$. Considering the greatest value of L in order to obtain an higher gain, the total dimension of the array is $70.6\text{mm} \times 70.6\text{mm}$ (because $2L = 70.6\text{mm}$). The unit cell length is 5mm so the final PRS layer is composed by 14×14 unit cells.

In order to evaluate approximately the antenna directivity, the plot of the radiation efficiency versus θ angle has been evaluated at five different frequencies:

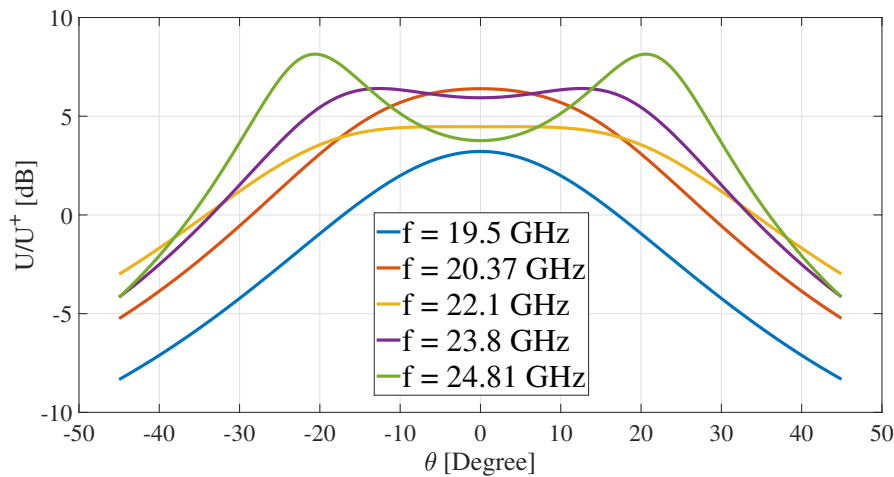


Figure 5.14: Normalized radiation intensity graph as function of θ for five different frequencies.

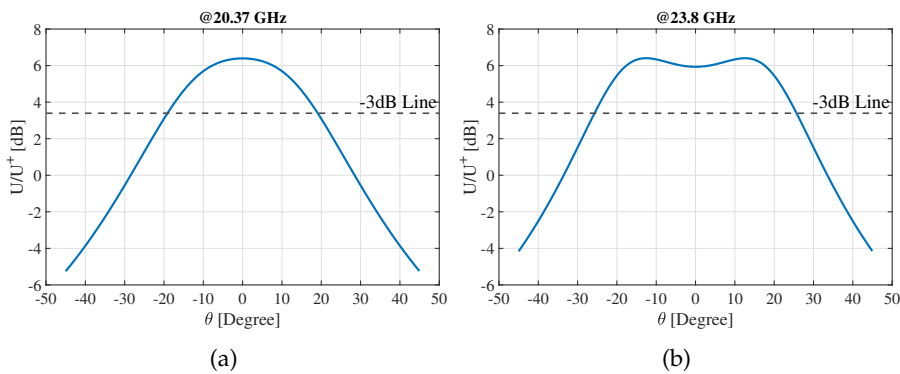


Figure 5.15: The radiation intensity graph at the two frequencies that show a peak in Fig 5.12 are reported. By considering the -3dB bandwidth limits, a directivity approximated value can be computed.

In particular the red and purple curves in Fig. 5.12 refer to the two peaks. From this two trends, the directivity can be estimated. The

directivity can be estimated using the formula Eq. (2.5). For the radiation intensity at 20.37GHz, the $-3dB$ beam-width is equal to 33° . Assuming the half power beam-width in the two main planes almost equal, the maximum antenna directivity is:

$$D = \frac{41.253}{HP_{E^\circ} * HP_{H^\circ}} = \frac{41.253}{38^\circ * 38^\circ} = 28.57,$$

$$D_{dB} = 10\log(D) = 14,56dB.$$

Regarding the radiation intensity at 23.8GHz, the $-3dB$ beam-width cannot be estimated properly because of the main beam splitting.

DESIGNED FPC ANTENNA

The FPC antenna is formed by a 14×14 unit cell PRS layer, that allows to obtain $R_{eff} = 99\%$, and an air filled cavity of height $h = 6.7\text{mm}$. The PRS has been excited by different radiating elements and in this section both slots and patches have been used analyzed. The radiating elements have to resonate at 20.37GHz and 23.8GHz , peak frequencies in Fig. 5.12. At this central values, the two antennas have to be matched in a band of at least 1GHz .

6.1 SLOT FEEDING

The analysis done in Chapter 5 is based on the fact that an equivalent magnetic source is located on the ground plane. For this reason and for its design simplicity, the slot antenna has been considered at the beginning as radiating source for the FPC structure.

6.1.1 Slot Design

Eq. (4.1) and (4.2) have been used to find the length and width of each slots at the two operating frequencies of 20.37GHz and 23.8GHz :



Figure 6.1: Slot antenna fed by a WR42 waveguide.

$$L \approx \frac{\lambda_0}{2} = 7.36\text{mm} \quad \text{and} \quad W = 0.07\lambda_0 = 0.52\text{mm},$$

$$L \approx \frac{\lambda_0}{2} = 6.3\text{mm} \quad \text{and} \quad W = 0.07\lambda_0 = 0.88\text{mm}.$$

After various simulations, changing L and W , a around 4GHz band matching at -10dB has been obtained:

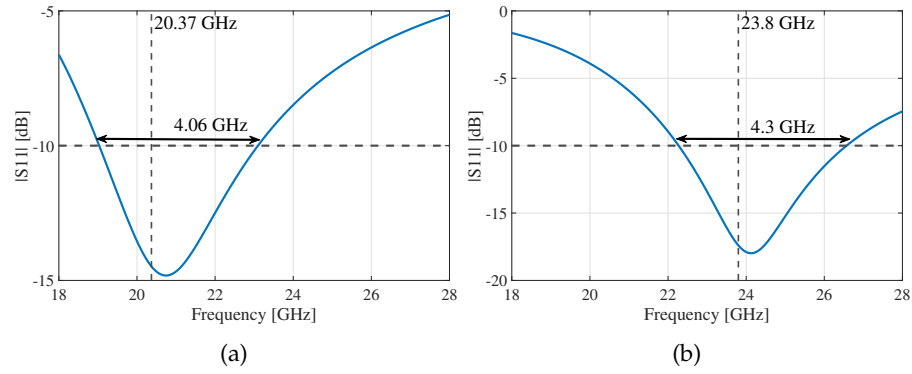


Figure 6.2: S_{11} of each slot matched at its working frequency.

The values for the slot resonating at 20.37GHz are $L = 7.1\text{mm}$ and $W = 1.28\text{mm}$. On the other hand, the slot resonating at 23.8GHz has $L = 6.1\text{mm}$ and $W = 1.1\text{mm}$.

6.1.2 Single feeding FPC

By adding the PRS on top of the ground plane, where the slot is located, at distance $h = 6.7\text{mm}$, the reflection coefficient changes and for this reason the structure has to be matched again by playing on the slot length and width. In Fig. 6.4 and 6.5 various matching results for $L = 6.9$ are reported.

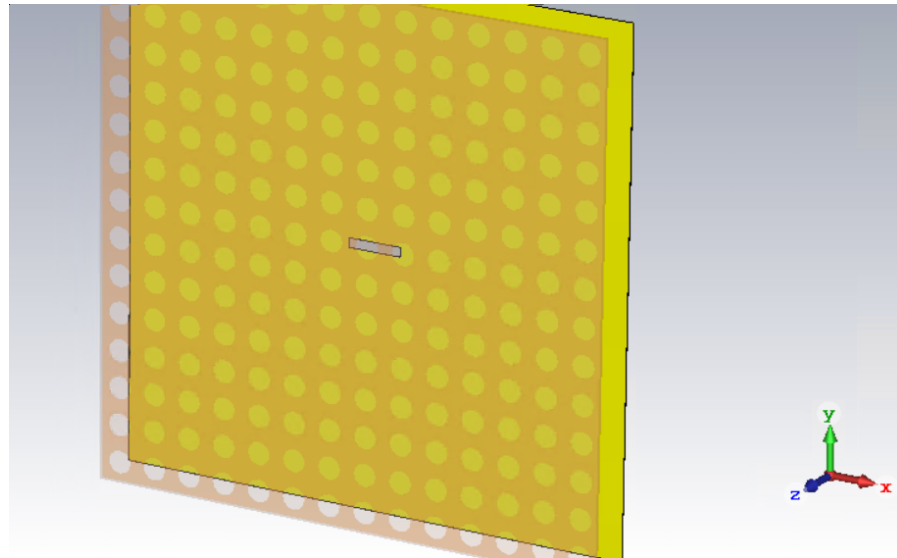


Figure 6.3: A perspective view of the single fed slot FPC antenna is shown.

The S_{11} , obtained from the simulation, has been optimized by changing the slot width. For a slot with $L = 6.9\text{mm}$ and $W = 4\text{mm}$, a matching of -15dB has been obtained in a wide frequency band.

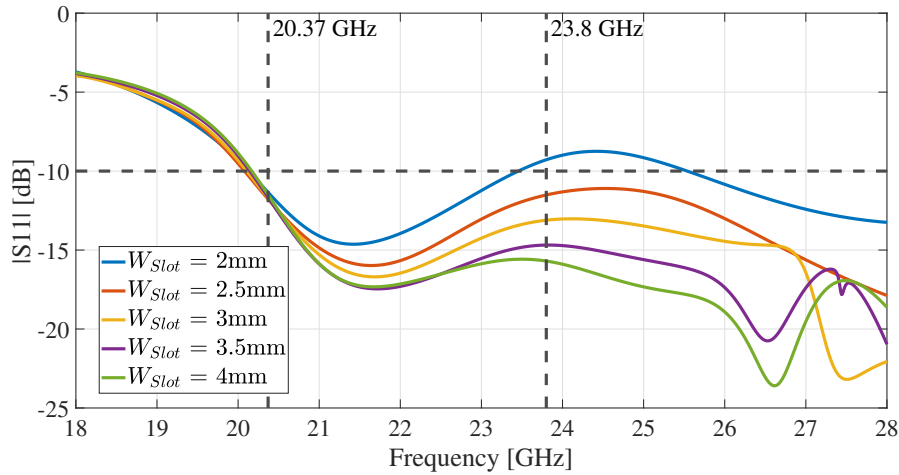


Figure 6.4: Matching improvement for the 23.8GHz resonating slot. By enlarging the width of the slot the matching can be even better than -15dB .

However, even if the matching is good for 23.8GHz, at the central frequency of 20.4GHz the -10dB band should at least 1GHz wide. To obtain this, further simulations have been done sweeping the slot length and width:

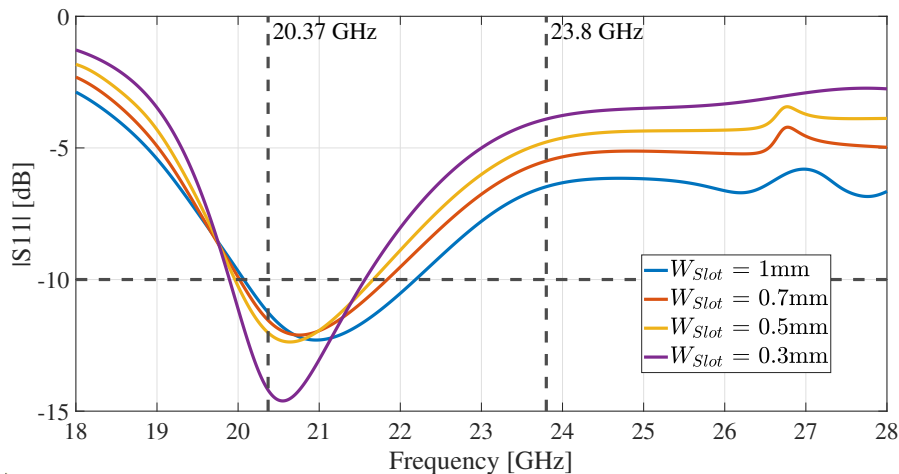


Figure 6.5: Matching improvement for 20.37GHz resonating slot. By shrinking the width of the slot the matching can arrive almost at -15dB .

A good result has been obtained still for $L = 6.9\text{mm}$, but with $W = 0.3\text{mm}$. However, this solution can't be accepted because of the fabrication constraint: the slot would be cut by hand in the lab and so the imprecision would be too high.

6.2 PATCH FEEDING

Patch antennas can be used as radiating elements as well as slots. In order to check if their behavior is the same as the slot one, reciprocity

theorem has been used and the radiation intensity plot has been evaluated.

6.2.1 Unit Cell Analysis

Fig. 6.6 shows the FPC antenna cross section considering a patch source instead of a slot. The chosen dielectric substrate for the patch is RO5880, whose characteristics are reported in Appendix E.

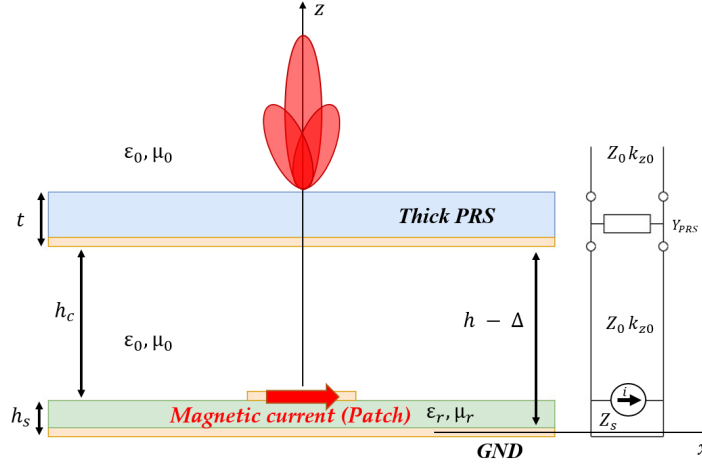


Figure 6.6: Cross section of a FPC antenna composed by a thick PRS and excited by a patch on a grounded dielectric substrate. The patch antenna is modeled with an equivalent x-directed magnetic current. By using TEN model, the thick PRS can be modeled as a two-port network.

The cavity height usually is equal to $h = \lambda_0/2$; considering the central frequency band around $f = 22\text{GHz}$:

$$h = \frac{\lambda_0}{2} = \frac{3 * 10^8}{22 * 10^9 * 2} \approx 6.8\text{mm}.$$

However, when the dielectric of thickness h_s is present, the cavity height becomes equal to $h_c = h - \Delta - h_s$. Delta is a correction factor defined as [8]:

$$\Delta = \frac{\lambda_0}{2\pi} \arctan \left[\frac{1}{\sqrt{\epsilon_s}} \tan \left(\frac{2\pi}{\lambda_0} \sqrt{\epsilon_s} h_s \right) \right] - h_s, \quad (6.1)$$

where ϵ_s is the relative dielectric constant of the substrate on which the patch is located. Solving Eq. (6.1), $\Delta = 39.1\mu\text{m}$ that is such a small value that can be considered negligible with respect to $h = 6.8\text{mm}$.

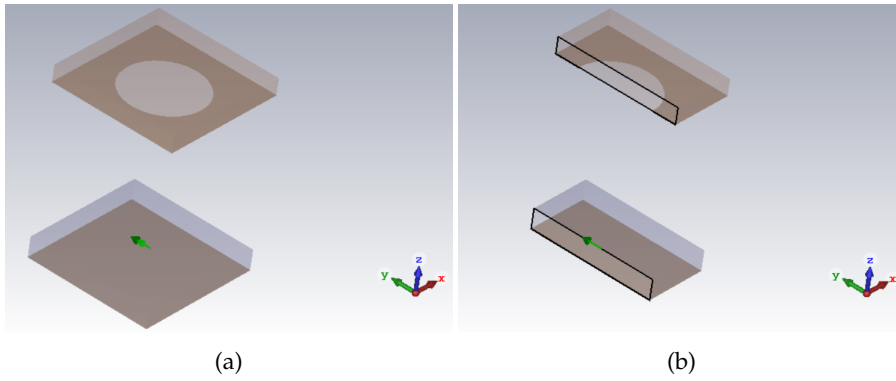


Figure 6.7: The unit cell chosen in Chapter 5 has been simulated by adding a grounded substrate at distance h_c . An electric probe on top of the RO5880 substrate and in the center, 6.7b, has been used to evaluate the electric field.

The electric field value is necessary to evaluate the radiated power. So, an electric probe oriented along y -axis has been placed in the center and on top of the RO5880 substrate. The probe is along the y -axis because the patch magnetic dipoles are along the x -axis as for the slot case.

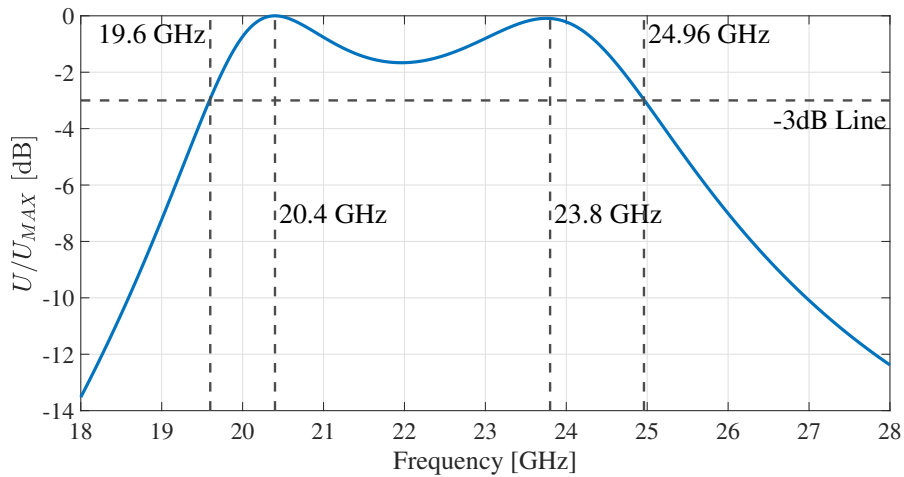


Figure 6.8: The radiated power has been normalized to his maximum. It shows behavior similar to the one obtained considering the slot as a source.

The incident radiation intensity on top of the PRS can be evaluated with Eq. (3.14) and, by normalizing it with respect to its maximum, it has been plot in Fig. 6.8. The behavior is similar to the one obtained considering a slot source and the two peak frequencies are 20.4GHz and 23.8GHz. The same consideration holds for the radiation intensity graph vs. angle θ .

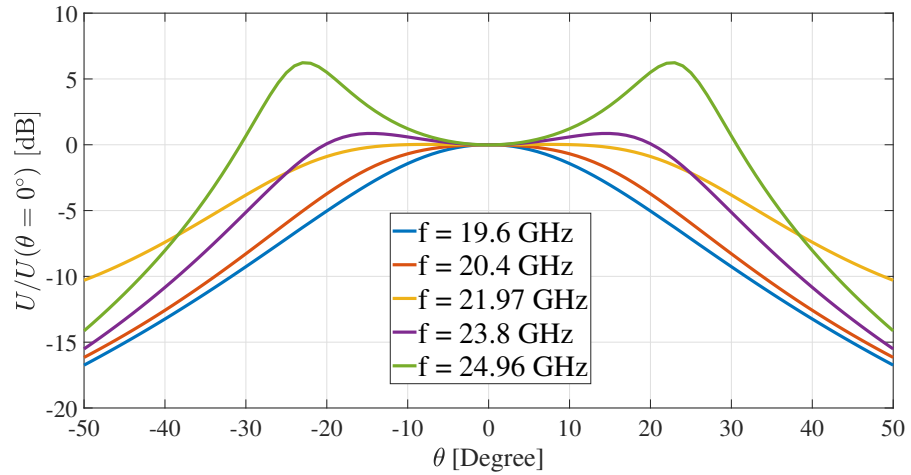


Figure 6.9: The radiated power for each frequency has been normalized to his value at $\theta = 0^\circ$ and it shows a similar behavior to the one obtained considering the slot as a source.

6.2.2 Patch Design

Two patches have been designed considering the formulas presented in Chapter 4. The first one is resonating at 20.4GHz while the second at 23.8GHz. The SubMiniature version A (SMA) connector has been used to feed the patch and its characteristic are reported in Appendix F.

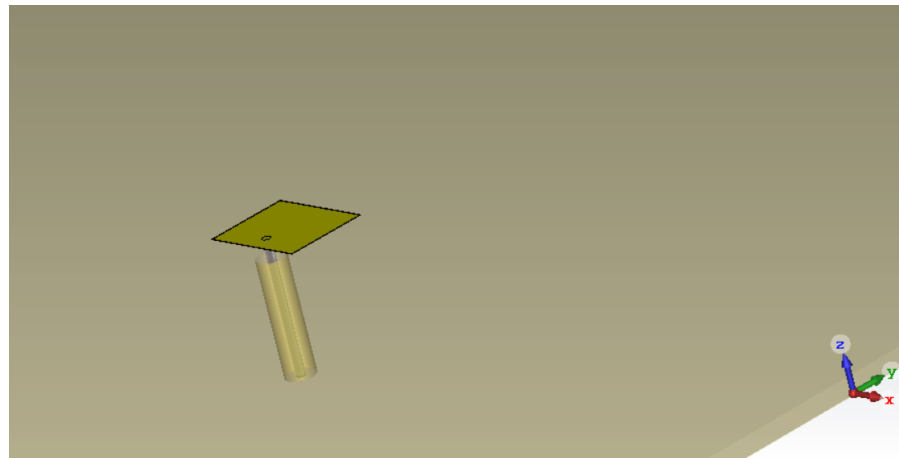


Figure 6.10: Patch antenna with coaxial feeding.

The patch that resonates at 20.4GHz has the following characteristics: $L = 4.3\text{mm}$, $W = 5.6\text{mm}$ and $x_0 = 1\text{mm}$, where x_0 is the distance between the coaxial cable pin to the closest width edge. On the other hand, the patch resonating at 23.8GHz has $L = 3.7\text{mm}$, $W = 4.6\text{mm}$ and $x_0 = 0.8\text{mm}$. With respect to the slot, they show a narrower -10dB bandwidth in accordance with theory.

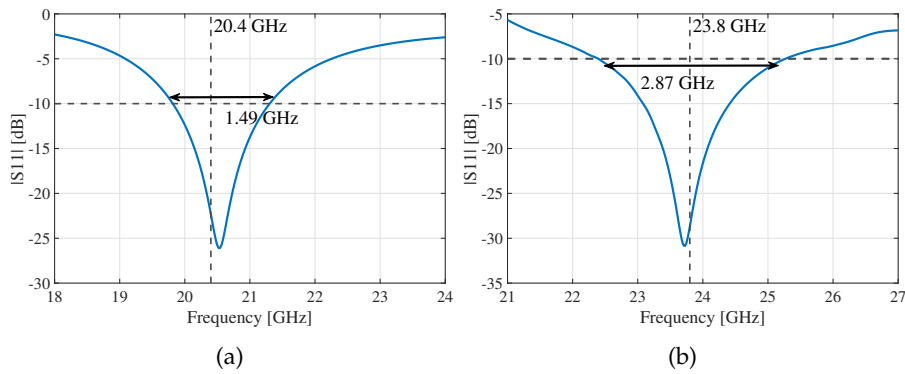


Figure 6.11: The reflection coefficients for both patches are reported.

6.2.3 Single port

The resulting matching, after putting the PRS on top of the patch at distance h_c , has been checked. The lengths and widths of the two patches have been changed to obtain again a good matching at the two operating frequencies.

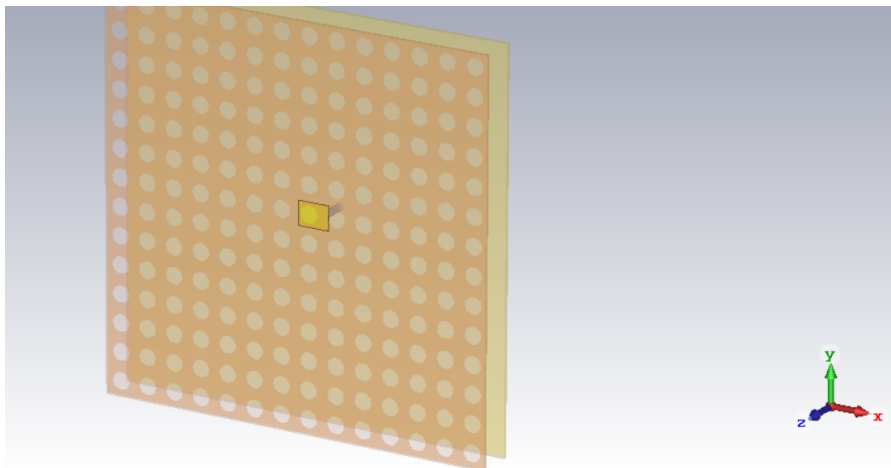


Figure 6.12: Structure of a single patch fed FPC antenna.

The parameters of the patch resonating at 20.4GHz changed to $L = 4.2\text{mm}$, $W = 5.6\text{mm}$ and $x_0 = 0.8\text{mm}$. On the other hand, the patch resonating at 23.8GHz has the following values: $L = 3.6\text{mm}$, $W = 4\text{mm}$ and $x_0 = 0.7\text{mm}$. With respect to the previous case, the matching bandwidth at -10dB is improved a bit.

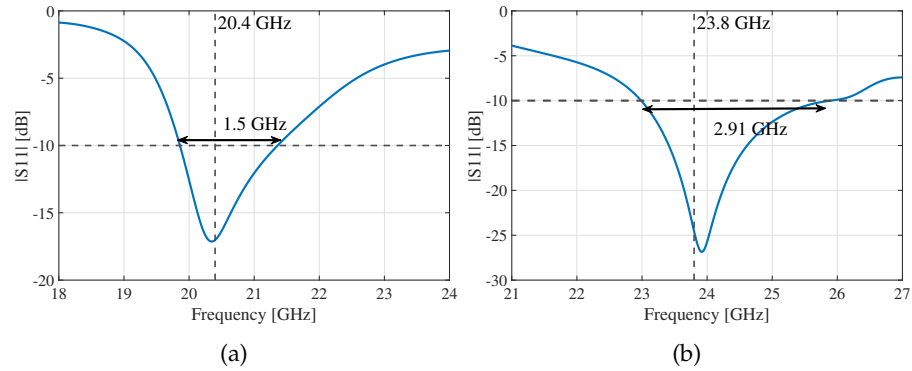


Figure 6.13: Reflection coefficients for the single patch fed FPC antenna at each resonant frequency .

6.3 FPC FED BY TWO PATCHES

Starting from the one feed structure, both patch antennas have been placed on the RO5880 substrate, Fig. 6.14.

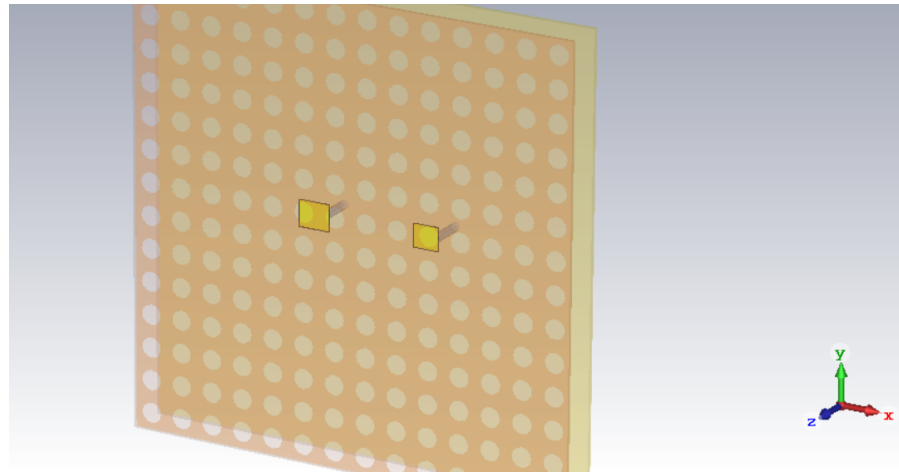


Figure 6.14: Perspective view of the double patch fed FPC antenna.

To maintain a good matching, the patch parameters have been changed again. The patch resonating at 20.4GHz has length $L = 4.1\text{mm}$, width to $W = 4.8\text{mm}$ and feeding distance to $x_0 = 0.8\text{mm}$. On the other hand, the one resonating at 23.8GHz has $L = 3.6\text{mm}$, $W = 4\text{mm}$ and $x_0 = 0.7\text{mm}$.

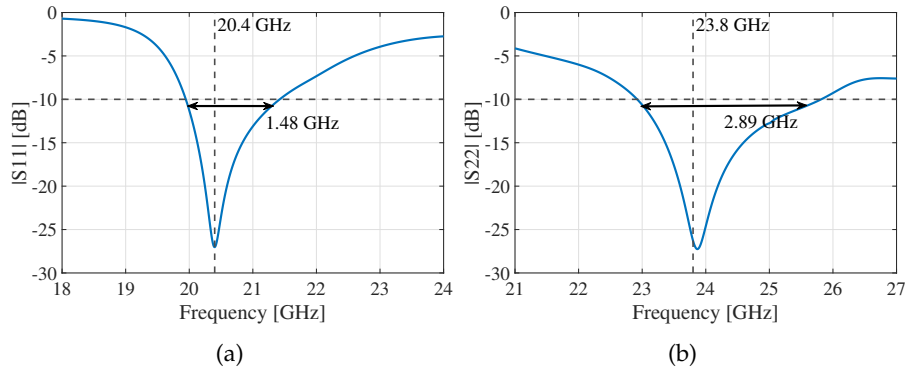


Figure 6.15: S_{11} and S_{22} of the double fed FPC antenna.

The broadside gain, however, shows a different height in the two peaks and the presence of a third one on the right. This last one is probably due to the wave reflections inside the cavity or to the coupling effect between the two patches.

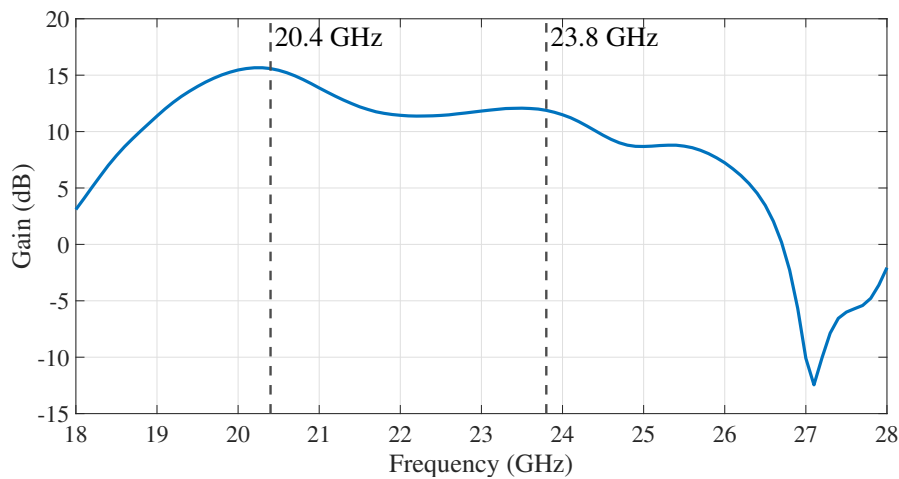
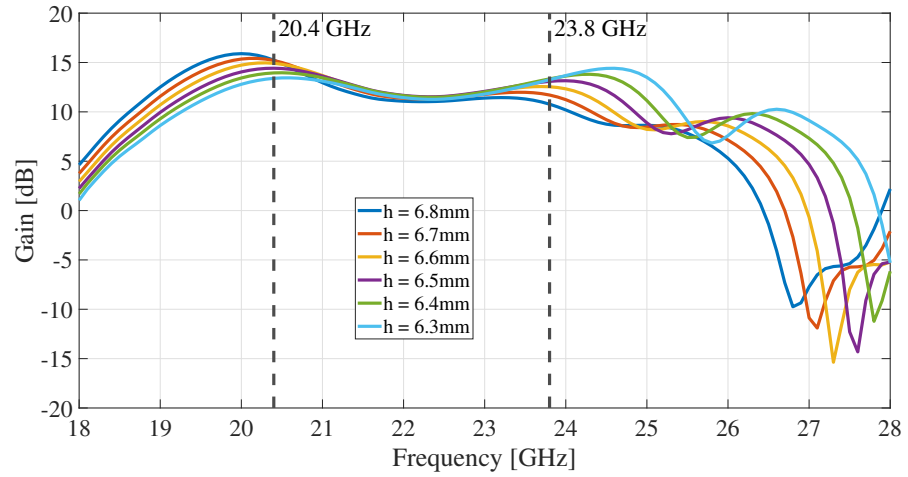


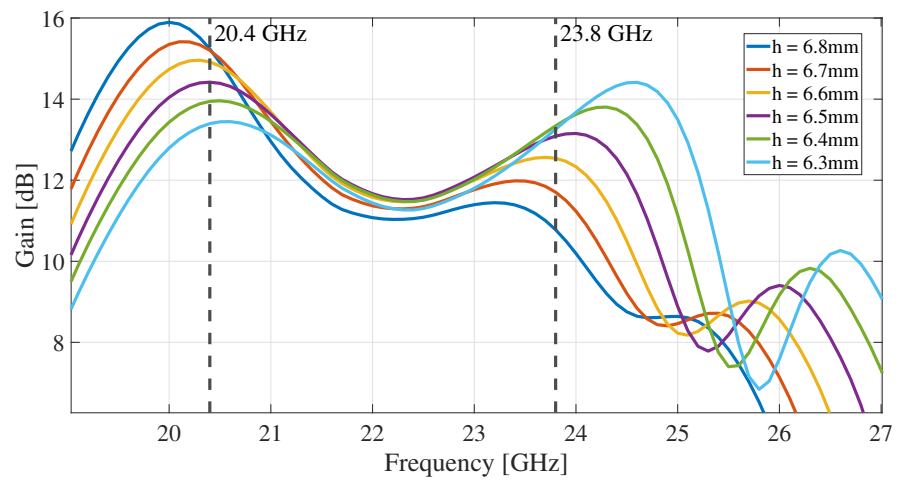
Figure 6.16: Broadside gain of the double fed FPC antenna. It shows an higher peak at lower frequency while the one at higher frequency is lowered.

6.3.0.1 Cavity height tuning

In order to have the same amount of radiated power at the two operating frequencies defined by the peaks, the cavity height has been changed. Decreasing the cavity height, as shown in Fig. 6.17b, reduces the peak at lower frequency and raises the one at the higher causing also its shift up in frequency. However, this height variation implies also an increase on the right side peak, Fig. 6.17a. The best cavity height has been obtained for $h = 6.4\text{mm}$, where the peaks at 20.4GHz and the one that was at 23.8GHz are more or less at the same level.



(a)



(b)

Figure 6.17: (a) shows how the second and third peaks increase by lowering the FPC antenna cavity height. (b) is a zoom on the two main peaks variation.

6.3.0.2 Distance between feedings

The distance D between feeding lines has been changed to check if it would have lowered the side peak probably generated by the coupling effect between the patches.

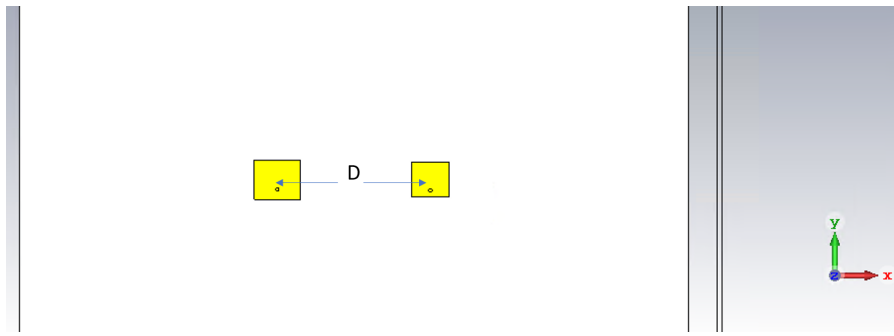
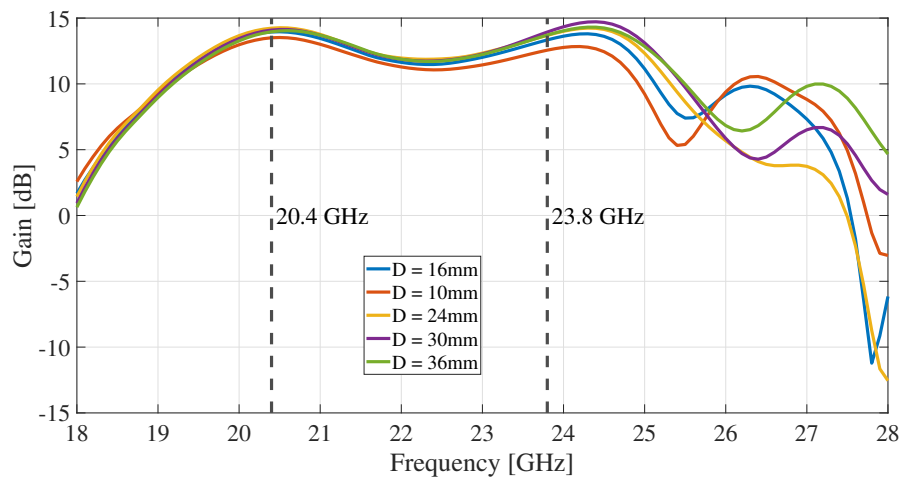
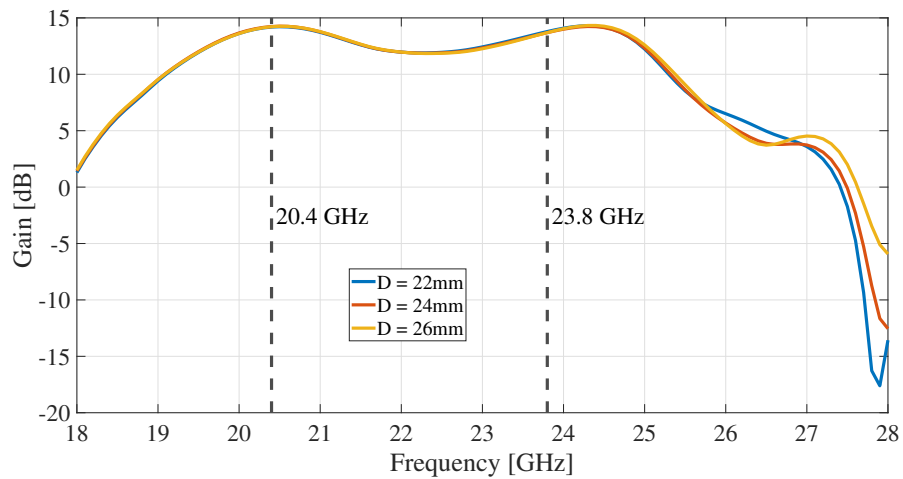


Figure 6.18: Definition of the distance between the two feeding lines.

Starting from the optimum cavity height of $h = 6.4\text{mm}$ obtained before, the following curves have been simulated by sweeping D :



(a)



(b)

Figure 6.19: (a) shows how the the third peak level changes by varying the distance D between the feeding coaxial cable pins. (b) shows values around $D = 24\text{mm}$.

Decreasing D from 16mm to 10mm, the peak shows an increase. On the other hand, increasing D from 16mm to 24mm lowers but from 30mm above the peak increasing again, Fig. 6.19a. The best behavior is for $D = 24$ mm.

6.3.1 Final structure

The structure with $D = 24$ mm and $h = 6.4$ mm has then been simulated and, as showed by blue lines in Fig.6.20, the matching got worse. The parameters of the two patches have then been tuned obtaining a good matching as showed by red lines. The patch resonating at 20.6GHz has $L = 4$ mm, $W = 4.8$ mm and $x_0 = 0.9$ mm. On the other hand, the one resonating at 24.3GHz has $L = 3.5$ mm, $W = 4$ mm and $x_0 = 0.7$ mm.

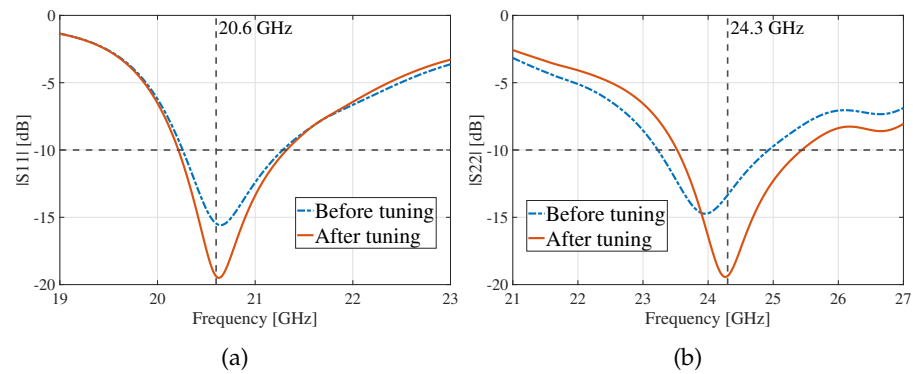


Figure 6.20: On the left, S_{11} is showed while on the right S_{22} . The blue curves shows the matching before the re-tuning while the red ones after.

Differently from the matching, the broadside gain remained almost the same as before the patches re-tuning.

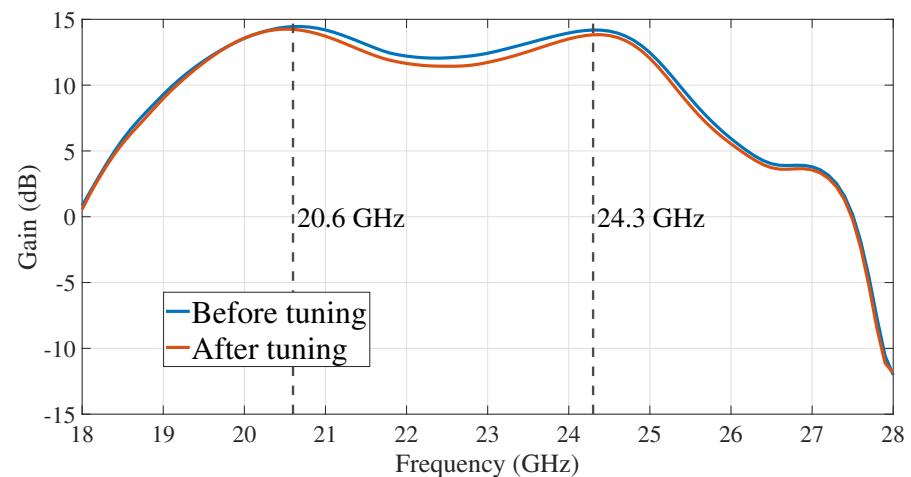


Figure 6.21: Broadside gain before and after the re-tuning of the patch dimensions.

6.3.1.1 Single port analysis

The structure has then been simulated considering one port excited at a time while the other one is closed on 50Ω .

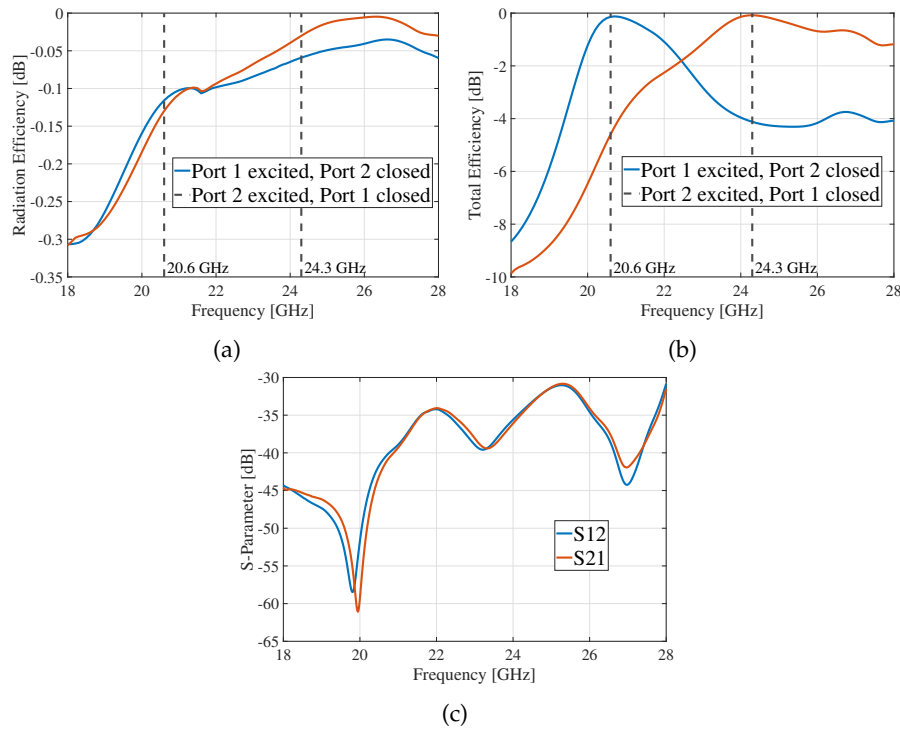


Figure 6.22: In (c) S_{12} and S_{21} are presented. Radiation efficiency and total efficiency are presented in (a) and (b), respectively.

The coupling effect between the sources has been simulated, S_{12} and S_{21} , showing in Fig. 6.22c a good value that is below -30 dB. The total efficiency is really high at resonant frequencies, almost 100% as shown in Fig. 6.22b. The radiation efficiency graph shows good results too: around 99%, as designed. The broadside gain when a port is excited and the other one is closed on 50Ω shows the behavior presented in Fig. 6.23a and Fig. 6.23b. The peak at the resonant frequency of the excited patch is higher than the other one. On the other hand, the realized gain has been plotted considering Eq. (2.9) with $\Gamma = S_{11}$. So, it can be equal or lower to the antenna gain. The realized gain curve satisfies the expected behavior because it is almost equal to the broadside gain in the matched frequency band.

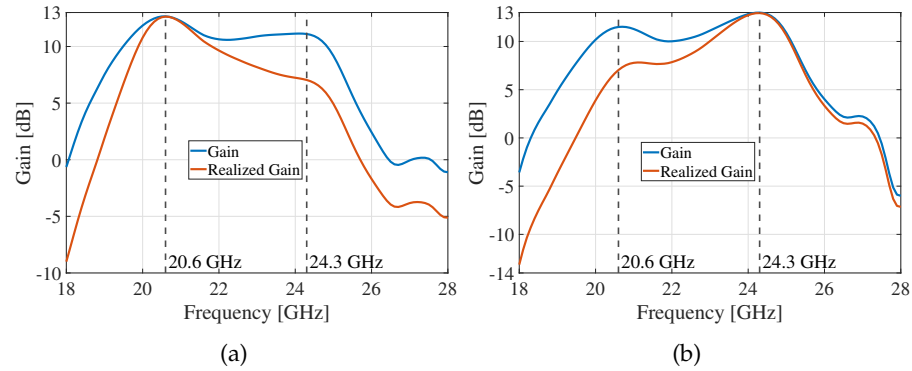


Figure 6.23: Gain and realized one at broadside when a radiated source is excited and the other one is closed on 50Ω .

6.3.1.2 14x14 vs. 20x20

Simulation for the 20x20 unit cell PRS have been performed to see if a better broadside gain could be obtained. However, after optimizing the cavity height and the distance between feedings, the broadside gain curve still shows a third low peak at higher frequencies.

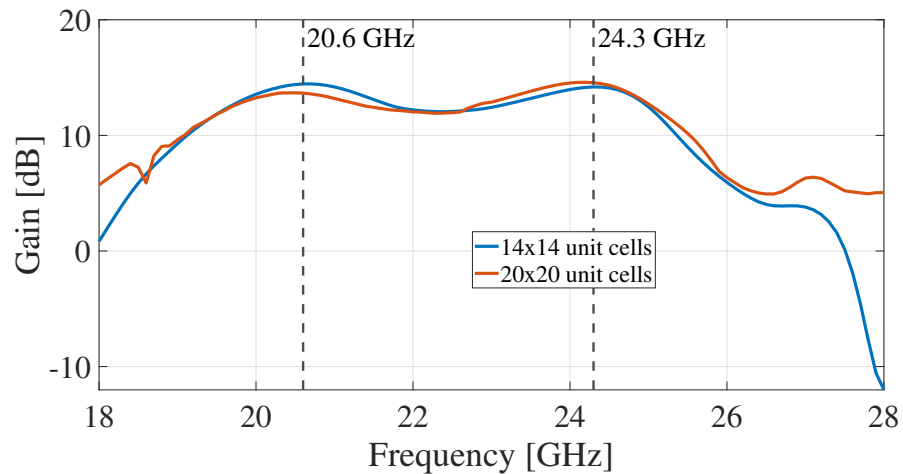


Figure 6.24: The broadside gain curves shows more or less the same behavior except for the third peak that is higher in FPC antenna formed by the 20x20 PRS.

In Fig. 6.24, the comparison between the FPC antenna with a 14x14 unit cell PRS and the 20x20 one is reported. The curves are more or less the same except for the fact the 14x14 has the lower third peak and so it is better than its bigger version.

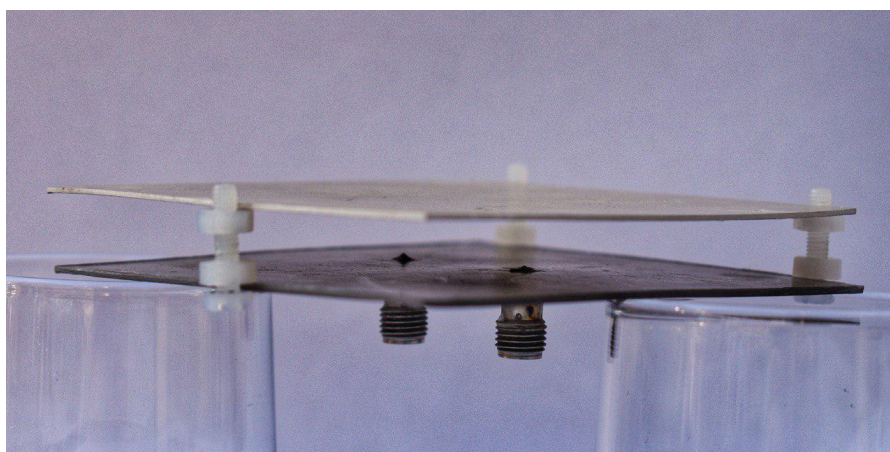
Part IV

FABRICATION AND CONCLUSION

FABRICATION AND TEST

7.1 FABRICATION

The FPC antenna formed by a 14x14 unit cell PRS and an air filled cavity with height 6.4mm has then been fabricated. The PRS layer and the patches antennas are showed in Fig.7.1:



(a)



(b)

Figure 7.1: (The fabricated antenna is shown in (a). On the other hand, (b) shows the bottom side of the thick PRS and the two patches.

The SMA connector used for the patches and its datasheet are reported in Appendix F. Instead of using a typical SMA that works till 18GHz,

due to the fact the pin has a diameter too big $d = 1.25\text{mm}$, a connector that can work till 26GHz has been used.

7.2 TEST

The scattering parameters of the realized structure have been computed using a R&S®ZVA Vector Network Analyzer. At first, the difference between the presence or not of the PRS on top of the radiating elements has been analyzed:

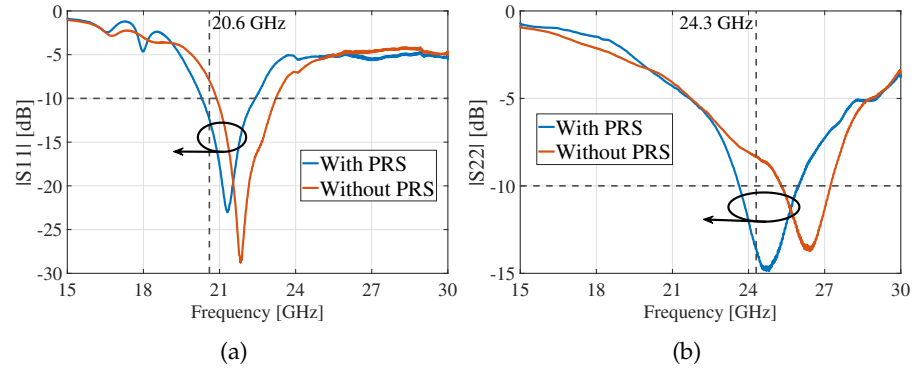


Figure 7.2: S_{11} and S_{22} with and without the PRS on top of them have been measured and reported. The graph shows a big shift down in frequency when adding the PRS structure.

As reported in Fig.7.2, a shift down in frequency is caused by adding the PRS on top of the air filled cavity. In Fig.7.3 the comparison between the simulated and measured S_{11} and S_{22} is reported.

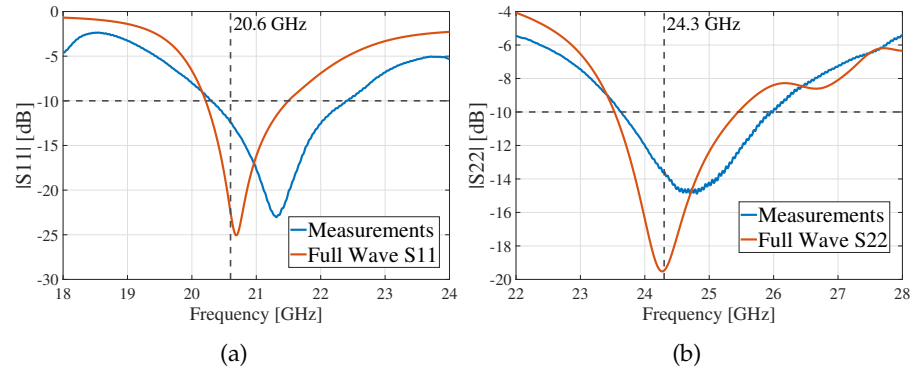


Figure 7.3: In (a) and (b) the S_{11} and S_{22} comparison between the measurements and the full wave simulations are reported. Although at 24.3GHz the matching is quite good, at 20.6GHz is shifted up in frequency probably due to fabrication inaccuracies.

The inaccuracy of both the curves is probably due to the fact they have been fabricated in laboratory where the precision is not so high considering also that working on mm and μm scales requires high precision. Then, the antenna gain referred to each single port with the

other one closed on 50Ω has been computed by using the formula presented in [36]:

$$G_{LWA} = G_{SGH} + 20 \log \left| S_{21}^{LWA} / S_{21}^{SGH} \right|, \quad (7.1)$$

where S_{21}^{LWA} and S_{21}^{SGH} are the transmission coefficients when the LWA or the Standard Gain Horn (SGH) antenna is used as the receiver, respectively. In Fig. 7.4, the comparison between measured and simulated broadside gain for the patch resonating at 20.6GHz is presented.

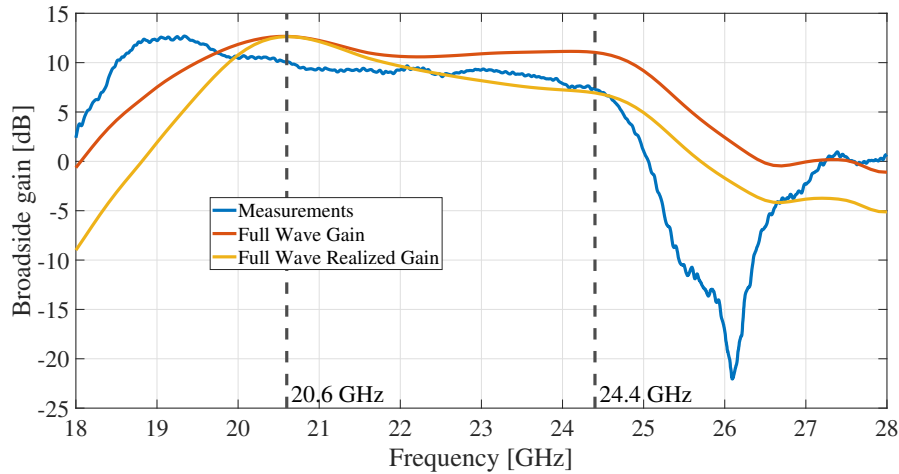


Figure 7.4: Large patch broadside gain

On the other hand, in figure 7.5 the comparison between measured and simulated broadside gain for the patch resonating at 24.3GHz is presented.

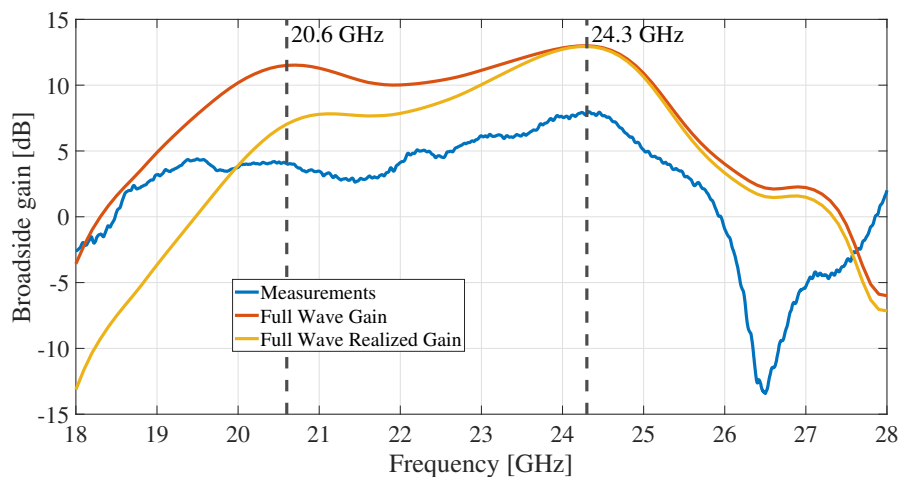


Figure 7.5: Small patch broadside gain

The large patch broadside gain shows comparison a good agreement between the simulation results and the measurements, except for the peak shifted down in frequency. This is probably due to fabrication

imprecision, measurements inaccuracy or the dielectric constant of the RO3010 substrate that could be bigger than the one used in the simulations, Appendix D. On the other hand, the small patch broadside gain is just lowered with respect to the simulation results. This result could be caused by fabrication imprecision or measurements inaccuracy as for the previous case. The radiation pattern in the principal planes, Fig. 7.6, shows a good agreement between the measurements and the simulation.

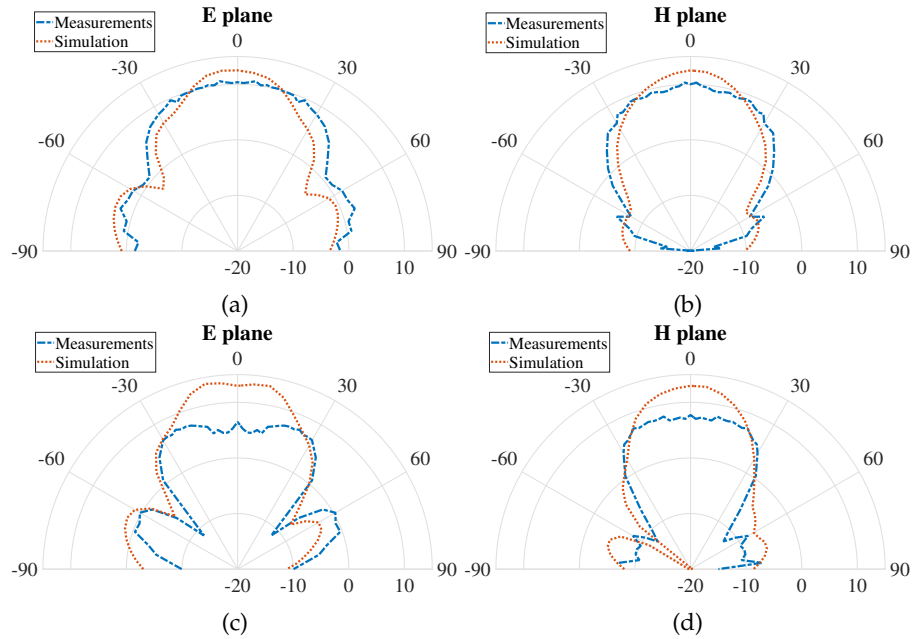


Figure 7.6: The comparison between measurements and simulations at the two resonance frequencies is presented for radiation pattern in the E - and H -plane. In (a) and (b), the E - and H -plane at 20.6GHz are shown. On the other hand, E - and H -plane at 24.3GHz are reported in (c) and (d).

CONCLUSIONS

In this thesis, after a review on LWAs, a wide-band FPC antenna fed by two patches has been designed. Starting from the elementary unit cell forming the PRS, various geometries and dielectric materials have been investigated. The optimum solution has then been chosen in terms of radiated power bandwidth and maximum gain. Afterwards, the FPC antenna consisting of a 14x14 unit cell PRS separated by air from two radiating patches, has been simulated. The distance between the two feedings and the cavity height have been optimized to have the lowest feeds coupling effect and the same gain value at the two resonance frequencies.

The final structure has been fabricated in the laboratory and various measurements has been taken. Although for the lowest resonance frequency, the broadside gain results is shifted down in frequency, its behavior and the one of at the higher resonance agree with the simulations.

8.1 FUTURE ANALYSIS

Some extra measurements has to be done to evaluate the correct ϵ_r of RO3010 that is probably the main cause in the broadside gain down-shifting for the larger patch. Moreover, other measurements are necessary for the smaller patch to obtain a better curve for the broadside gain.

Part V

APPENDIX

ATMOSPHERIC ABSORPTION AT EHF

The electromagnetic energy transmitted by an antenna in the space is attenuated by its passage in the atmosphere. This energy loss is in part due to the scattering with airborne particles, snow and rain and in part to atmospheric absorption [37]. The major compounds responsible for the signal absorption are oxygen (O_2) and water vapor (H_2O). In the following

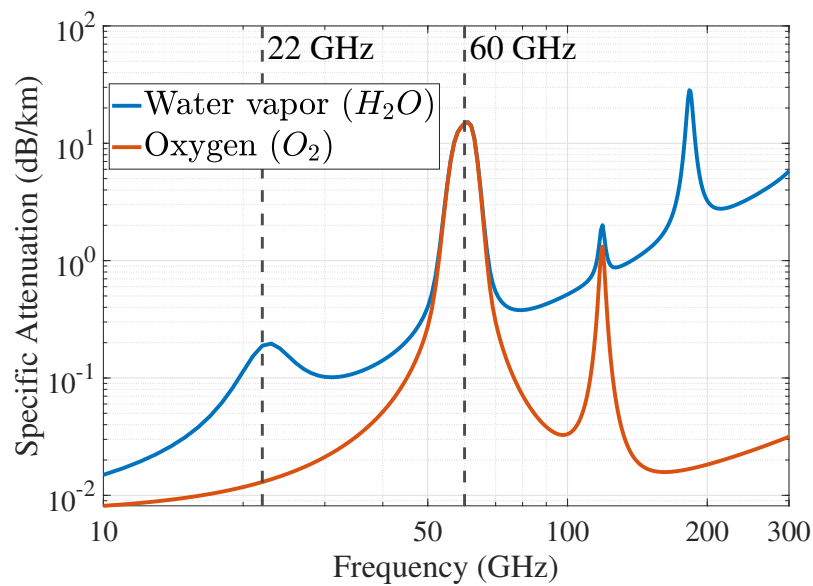


Figure A.1: The attenuation spectrum for water vapor, with density 7.5g/m, and oxygen is reported following the instructions presented in [37].

The attenuation spectrum showed in Fig. A.1 belongs to 10 – 300GHz frequency range with an atmospheric pressure of 101.300kPa and a temperature of 15°. By looking at the figure the first peak occurs at 22 GHz due to water vapor, while the second at 60 GHz due to oxygen. For this reason, signals using millimeter-wave spectrum suffers of higher atmospheric absorption than lower frequency signals.

TEN MODEL ADMITTANCES DERIVATION

This chapter presents the evaluation of Y_{down} and Y_{up} showed in Fig.3.6. To do so, the basic transmission line theory has been employed [38].

B.1 EVALUATION OF Y_{down}

In Fig.B.1, the TL model considers the part below PRS of the TEN model in Fig.3.6.

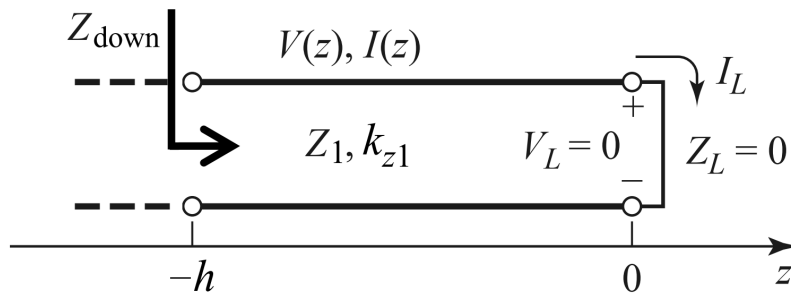


Figure B.1: TL model from PRS bottom port till the magnetic equivalent source located on the ground plane.

The generic voltage in any point of the line is defined as:

$$V(z) = V_o^+ e^{-jk_{z1}z} + V_o^- e^{jk_{z1}z}. \quad (\text{B.1})$$

Similarly, the total current is expressed as:

$$I(z) = \frac{V_o^+}{Z_1} e^{-jk_{z1}z} - \frac{V_o^-}{Z_1} e^{jk_{z1}z}. \quad (\text{B.2})$$

The load impedance is defined by the ratio between the total voltage and current at section $z = 0$. From this relation, the forward or backward wave can be expressed in function of the impedance:

$$Z_L = \frac{V(0)}{I(0)} = \frac{V_o^+ + V_o^-}{V_o^+ - V_o^-} Z_1 \quad \longrightarrow \quad V_o^- = \frac{Z_L - Z_1}{Z_L + Z_1} V_o^+.$$

The reflection coefficient is defined as the ratio between the reflected voltage wave and the incident one:

$$\Gamma = \frac{V_o^-}{V_o^+} = \frac{Z_L - Z_1}{Z_L + Z_1}. \quad (\text{B.3})$$

The total voltage and current on the line can then be rewritten as:

$$V(z) = V_o^+ \left(e^{-jk_{z1}z} + \Gamma e^{jk_{z1}z} \right),$$

$$I(z) = \frac{V_o^+}{Z_1} \left(e^{-jk_{z1}z} - \Gamma e^{jk_{z1}z} \right).$$

When the transmission line is short circuited, $Z_L = 0$, the reflection coefficient is equal to -1 using B.3. Moreover, due to the following relations $\cos(x) = \frac{e^{jx} + e^{-jx}}{2}$ and $\sin(x) = \frac{e^{jx} - e^{-jx}}{2j}$, the generic voltage and current on the line becomes:

$$V(z) = V_o^+ \left(e^{-jk_{z1}z} - e^{jk_{z1}z} \right) = -2jV_o^+ \sin k_{z1}z,$$

$$I(z) = \frac{V_o^+}{Z_1} \left(e^{-jk_{z1}z} + e^{jk_{z1}z} \right) = \frac{2V_o^+}{Z_1} \cos k_{z1}z.$$

The impedance Z_{down} , seen at $z = -h$, is:

$$Z_{down} = \frac{V(-h)}{I(-h)} \longrightarrow Z_{down} = \frac{-2jV_o^+ \sin(k_{z1}(-h))}{\frac{2V_o^+}{Z_1} \cos(k_{z1}(-h))},$$

$$\longrightarrow Z_{down} = \frac{2jV_o^+ \sin(k_{z1}h)}{\frac{2V_o^+}{Z_1} \cos(k_{z1}h)},$$

$$\longrightarrow Z_{down} = jZ_1 \tan(k_{z1}h). \quad (\text{B.4})$$

The admittance Y_{down} , considering that $Y_1 = Y_0 \sqrt{\frac{\epsilon_r}{\mu_r}} = Y_0 \xi_r$, then is:

$$Y_{down} = \frac{1}{Z_{down}} \longrightarrow Y_{down} = \frac{1}{jZ_1 \tan k_{z1}h},$$

$$\longrightarrow Y_{down} = -jY_1 \cot(k_{z1}h),$$

$$\longrightarrow Y_{down} = -j\xi_r Y_0 \cot(k_{z1}h). \quad (\text{B.5})$$

B.2 EVALUATION OF Y_{up}

On the other hand, Y_{up} can be evaluated by using the TL model that considers the PRS plus air in the TEN model in Fig.3.6.

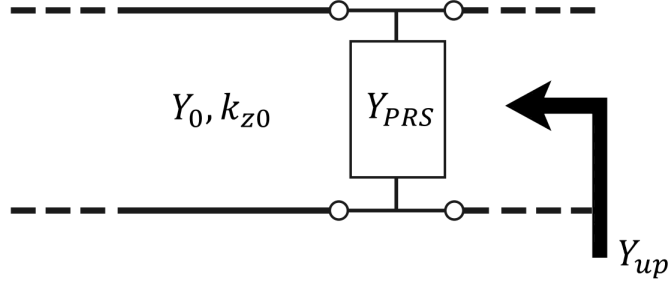


Figure B.2: TL model seen from the bottom PRS port looking up. It is formed by a load, PRS, and an infinite transmission line that models the air.

If the PRS is lossless, the unit substrate admittance is $Y_{PRS} = jB_s$. Otherwise, considering the losses, $Y_{PRS} = G + jB_s$.

The line that models air is infinite long so, the TL model will become:

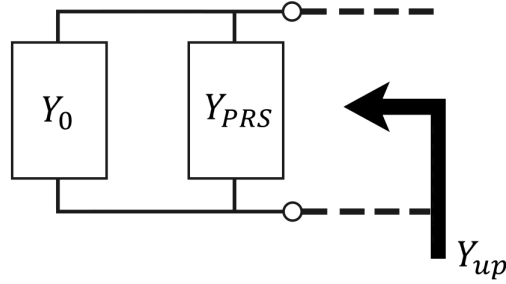


Figure B.3: Equivalent TL model of Fig. ?? where the infinite transmission line is modeled by a load with characteristic impedance equal to the one of the line itself.

The value of Y_{up} is:

$$Y_{up} = Y_{PRS} + Y_0 = G + Y_0 + jB_s = g + jb, \quad (\text{B.6})$$

where $g = G + Y_0$ and $B_s = b$. In the lossless case, $G = 0$. The admittance Y_{up} can be also written as:

$$Y_{up} = Y_0(\hat{g} + j\hat{b}), \quad (\text{B.7})$$

where $\hat{g} = g/Y_0$ and $\hat{b} = b/Y_0$.

ROGER SUBSTRATE THICKNESS LIMITATIONS

In Chapter 5, different dielectric substrates have been used to evaluate the PRS reflection coefficient while in Chapter 6 the RO5880 has been introduced for the patch design. Manufacturer thickness limitations of these material are reported in this appendix, except for RO3010 and RO5880 whose characteristics are presented respectively in Appendix D and E. The meaning of cladding values, for all the dielectric layers, are listed as follows:

DIELECTRIC THICKNESS	CLADDING THICKNESS
HH/HH	17 μ m
H1/H1	35 μ m
5E/5E	17 μ m
1E/1E	35 μ m
2E/2E	70 μ m
1R/1R	35 μ m

Table C.1: Roger Cladding Thickness Notation

C.1 RO3210

Further information about the dielectric characteristics can be found on its datasheet [39].

DIELECTRIC THICKNESS	CLADDING THICKNESS
0.025inch = 0.64mm	H1/H1
	HH/HH
0.05inch = 1.28mm	H1/H1
	HH/HH

Table C.2: RO3210 dielectric and cladding thickness limitations

C.2 RO4360G2

Further information about the dielectric characteristics can be found on its datasheet [40].

DIELECTRIC THICKNESS	CLADDING THICKNESS
0.008inch = 0.203mm	5E/5E
0.012inch = 0.305mm	1E/1E 5E/5E
0.02inch = 0.508mm	1E/1E 5E/5E
0.032inch = 0.813mm	1E/1E 5E/5E
0.06inch = 1.524mm	1E/1E 5E/5E

Table C.3: RO4360G2 dielectric and cladding thickness limitations

C.3 TMM13I AND TMM10I

Further information about these two dielectric characteristics can be found on their datasheet [41].

DIELECTRIC THICKNESS	CLADDING THICKNESS
0.05inch = 1.27mm	H1/H1 HH/HH
0.075inch = 1.905mm	HH/HH
0.1inch = 2.54mm	HH/HH
0.15inch = 3.81mm	H1/H1

Table C.4: TMM13i dielectric and cladding thickness limitations

DIELECTRIC THICKNESS	CLADDING THICKNESS
0.01inch = 0.254mm	H1/H1
0.015inch = 0.381mm	H1/H1 HH/HH
0.02inch = 0.508mm	H1/H1 HH/HH
0.025inch = 0.635mm	H1/H1 HH/HH
0.03inch = 0.762mm	H1/H1 HH/HH
0.05inch = 1.27mm	H1/H1 HH/HH
0.06inch = 1.524mm	H1/H1
0.125inch = 3.175mm	H1/H1
0.15inch = 3.810mm	H1/H1
0.25inch = 6.350mm	H1/H1

Table C.5: TMM10i dielectric and cladding thickness limitations

C.4 RO4350B

DIELECTRIC THICKNESS	CLADDING THICKNESS
0.004inch = 0.101mm	1E/1E
	5E/5E
0.0066inch = 0.168mm	1E/1E
	5E/5E
0.01inch = 0.254mm	1E/1E
	2E/2E
	5E/5E
0.0133inch = 0.338mm	1E/1E
0.0166inch = 0.422mm	5E/5E
	HH/HH
0.02inch = 0.508mm	1E/1E
	2E/2E
	5E/5E
0.03inch = 0.762mm	1E/1E
	5E/5E
0.06inch = 1.524mm	1E/1E
	5E/5E

Table C.6: RO4350B dielectric and cladding thickness limitations

DATASHEET RO₃₀₁₀

Roger RO₃₀₁₀ substrate has been used in the design process of the PRS structure to evaluate its reflection coefficient. Because of the good results achieved in the simulations, then it has been used to fabricate the structure.

The RO₃₀₁₀ available sample thickness are reported below:

DIELECTRIC THICKNESS	CLADDING THICKNESS
0.005 inch = 0.13 mm	H1/H1
	HH/HH
0.01 inch = 0.25 mm	H1/H1
	HH/HH
0.02 inch = 0.508 mm	HH/HH
0.025 inch = 0.64 mm	H1/H1
	HH/HH
0.05 inch = 1.28 mm	H1/H1
	HH/HH

Table D.1: RO₃₀₁₀ thickness limitations

The cladding thickness notation meaning is reported in Appendix C. Starting from these limitations, the unit cell parameters have been chosen in order to obtain a wide radiated power bandwidth. In particular, this material shows two different values for the dielectric constant. One is defined as *design* and the other one as *process*. They differs in the method they have been evaluated and for the frequency range they are valid in. The first one is equal to 11.2 while the second around 10.2. CST microwave studio uses the *design* value instead of the *process*. More information on RO₃₀₁₀ is reported in the datasheet shown in the following pages.



RO3000® Series Circuit Materials

RO3003™, RO3006™, RO3010™ and RO3035™

High Frequency Laminates

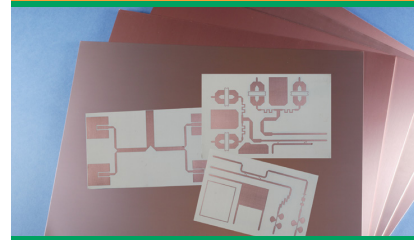
RO3000® high frequency circuit materials are ceramic-filled PTFE composites intended for use in commercial microwave and RF applications. This family of products was designed to offer exceptional electrical and mechanical stability at competitive prices.

RO3000 series laminates are ceramic-filled PTFE based circuit materials with mechanical properties that are consistent regardless of the dielectric constant selected. This allows the designer to develop multi-layer board designs that use different dielectric constant materials for individual layers, without encountering warpage or reliability problems.

RO3000 materials exhibit a coefficient of thermal expansion (CTE) in the X and Y axis of 17 ppm/°C. This expansion coefficient is matched to that of copper, which allows the material to exhibit excellent dimensional stability, with typical etch shrinkage (after etch and bake) of less than 0.5 mils per inch. The Z-axis CTE is 24 ppm/°C, which provides exceptional plated through-hole reliability, even in severe thermal environments. The dielectric constant versus temperature for RO3003™ and RO3035™ materials is very stable (Chart 1).

RO3000 series laminates can be fabricated into printed circuit boards using standard PTFE circuit board processing techniques, with minor modifications as described in the application note "Fabrication Guidelines for RO3000 Series High Frequency Circuit Materials."

Data Sheet



Features and Benefits:

Low dielectric loss (RO3003™ laminates)

- Laminates can be used in applications up to 77 GHz.

Excellent mechanical properties versus temperature

- Reliable stripline and multi-layer board constructions.

Uniform mechanical properties for a range of dielectric constants

- Ideal for multi-layer board designs with a range of dielectric constants
- Suitable for use with epoxy glass multi-layer board hybrid designs

Stable dielectric constant versus temperature and frequency (RO3003 laminates)

- Ideal for band pass filters, microstrip patch antennas, and voltage controlled oscillators.

Low in-plane expansion coefficient (match to copper)

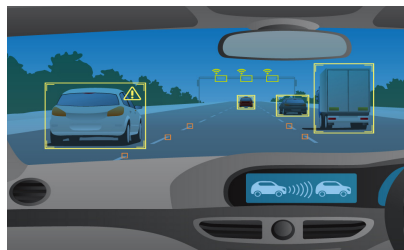
- Allows for more reliable surface mounted assemblies
- Ideal for applications sensitive to temperature change
- Excellent dimensional stability

Volume manufacturing process

- Economical laminate pricing

Some Typical Applications:

- Automotive radar applications
- Global positioning satellite antennas
- Cellular telecommunications systems - power amplifiers and antennas
- Patch antenna for wireless communications
- Direct broadcast satellites
- Datalink on cable systems
- Remote meter readers
- Power backplanes



Advanced Connectivity Solutions

100 S. Roosevelt Avenue, Chandler, AZ 85226
Tel: 480-961-1382 Fax: 480-961-4533 www.rogerscorp.com

Chart 1: RO3003 and RO3035 Laminate Dielectric Constant vs. Temperature

The data in Chart 1 demonstrates the excellent stability of dielectric constant over temperature for RO3003 & RO3035 laminates, including the elimination of the step change in dielectric constant, which occurs near room temperature with PTFE glass materials. The data in Chart 2 shows the

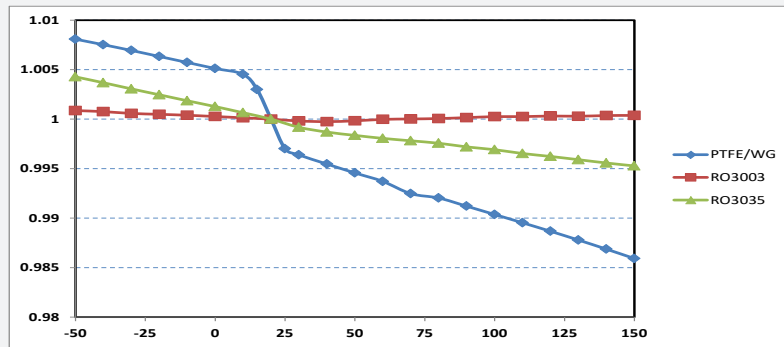


Chart 2: RO3003 and RO3035 Dissipation Factor

distribution of dissipation factor for RO3003 and RO3035 materials.

Test Method: IPC-TM-650 2.5.5.5
Condition: 10 GHz 23° C

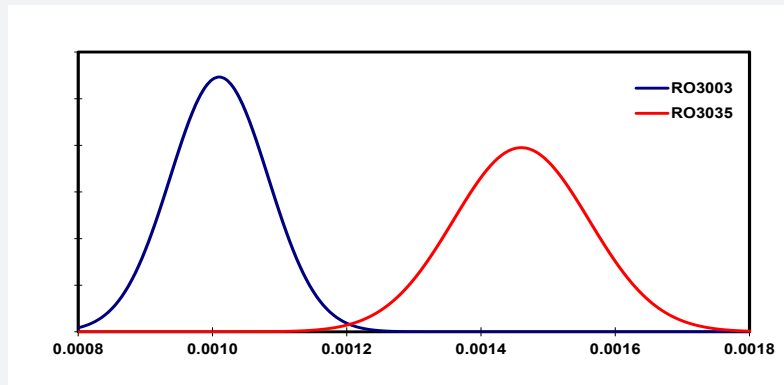
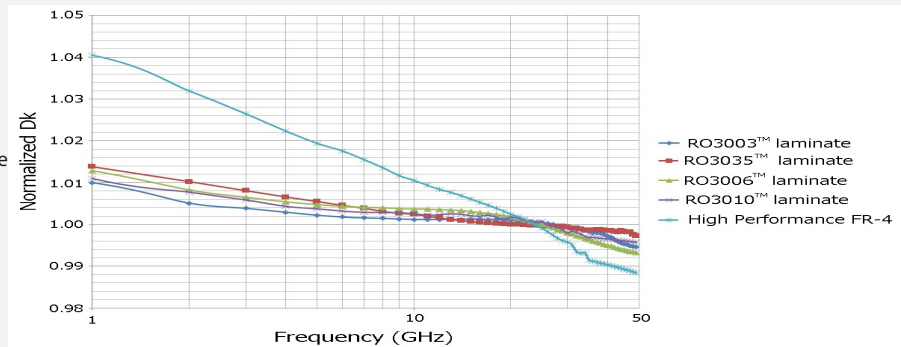


Chart 3: Normalized Dk vs. Frequency using microstrip differential phase length method 50 ohm microstrip circuits based on ~20mil thick laminates

Chart 3 demonstrates the stability of dielectric constant for RO3000 series products over frequency. This stability simplifies the design of broadband components as well as allowing the materials to be used in a wide range of applications over a very broad range of frequencies.



Property	Typical Value ⁽¹⁾				Direction	Unit	Condition	Test Method
	RO3003	RO3035	RO3006	RO3010				
Dielectric Constant, ϵ_r , Process	3.00 ± 0.04	3.50 ± 0.05	6.15 ± 0.15	10.2 ± 0.30	Z	-	10 GHz 23°C	IPC-TM-650 2.5.5.5 Clamped Stripline
⁽²⁾ Dielectric Constant, ϵ_r , Design	3.00	3.60	6.50	11.20	Z	-	8 GHz - 40 GHz	Differential Phase Length Method
Dissipation Factor, tan δ	0.0010	0.0015	0.0020	0.0022	Z	-	10 GHz 23°C	IPC-TM-650 2.5.5.5
Thermal Coefficient of ϵ_r	-3	-45	-262	-395	Z	ppm/°C	10 GHz -50 to 150°C	IPC-TM-650 2.5.5.5
Dimensional Stability	-0.06 0.07	-0.11 0.11	-0.27 -0.15	-0.35 -0.31	X Y	mm/m	COND A	IPC-TM-650 2.2.4
Volume Resistivity	10 ⁷	10 ⁷	10 ⁵	10 ⁵		MΩ-cm	COND A	IPC 2.5.17.1
Surface Resistivity	10 ⁷	10 ⁷	10 ⁵	10 ⁵		MΩ	COND A	IPC 2.5.17.1
Tensile Modulus	930 823	1025 1006	1498 1293	1902 1934	X Y	MPa	23°C	ASTM D638
Moisture Absorption	0.04	0.04	0.02	0.05	-	%	D48/50	IPC-TM-650 2.6.2.1
Specific Heat	0.9		0.86	0.8		J/g/K		Calculated
Thermal Conductivity	0.50	0.50	0.79	0.95	-	W/m/K	50°C	ASTM D5470
Coefficient of Thermal Expansion	17 16 25	17 17 24	17 17 24	13 11 16	X Y Z	ppm/°C	-55 to 288°C	ASTM D3386-94
Td	500	500	500	500		°C TGA		ASTM D3850
Density	2.1	2.1	2.6	2.8		gm/cm ³	23°C	ASTM D792
Copper Peel Strength	12.7	10.2	7.1	9.4		lb/in	1 oz. EDC After Solder Float	IPC-TM-2.4.8
Flammability	V-0	V-0	V-0	V-0				UL 94
Lead Free Process Compatible	YES	YES	YES	YES				



NOTES:

(1) Typical values are a representation of an average value for the population of the property. For specification values contact Rogers Corporation.

(2) The design Dk is an average number from several different tested lots of material and on the most common thickness/s. If more detailed information is required, please contact Rogers Corporation or refer to Rogers' technical papers in the Roger Technology Support Hub available at <http://www.rogerscorp.com/acm/technology>.

Standard Thickness	Standard Panel Size	Available Copper Cladding
RO3003/RO3035: 0.005" (0.13mm) 0.010" (0.25mm) 0.020" (0.50mm) 0.030" (0.75mm) 0.060" (1.52mm)	12" X 18" (305 X 457mm)	¼ oz. (9µm) electrodeposited copper foil (HQ/HQ)
	24" X 18" (610 X 457mm)	½ oz. (17µm) electrodeposited copper foil (HH/HH)
RO3006/RO3010: 0.005" (0.13mm) 0.010" (0.25mm) 0.025" (0.64mm) 0.050" (1.28mm)		1 oz. (35µm) electrodeposited copper foil (H1/H1)
		2 oz. (70µm) electrodeposited copper foil (H2/H2)
		½ oz. (17µm) reverse treated electrodeposited cu foil (SH/SH)
		1 oz. (35µm) reverse treated electrodeposited cu foil (S1/S1)
		2 oz. (70µm) reverse treated electrodeposited cu foil (S2/S2)
		RO3003 & RO3035 laminates also available with ½, 1 and 2 oz. rolled copper foil
	RO3003 5 mil thick laminates also available with 6 oz. rolled copper foil and 0.040" rolled copper plate	
	Other claddings may be available. Contact customer service.	

The information in this data sheet is intended to assist you in designing with Rogers' circuit materials. It is not intended to and does not create any warranties express or implied, including any warranty of merchantability or fitness for a particular purpose or that the results shown on this data sheet will be achieved by a user for a particular purpose. The user should determine the suitability of Rogers' circuit materials for each application.

These commodities, technology and software are exported from the United States in accordance with the Export Administration regulations. Diversion contrary to U.S. law prohibited.

The Rogers' logo, Helping power, protect, connect our world, RO3000, RO3003, RO3006, R03010 and RO3035 are trademarks of Rogers Corporation or one of its subsidiaries.

©2018 Rogers Corporation, Printed in U.S.A., All rights reserved.
 Revised 1400 092518 **Publication** #92-130

Advanced Connectivity Solutions
 100 S. Roosevelt Avenue, Chandler, AZ 85226
 Tel: 480-961-1382 Fax: 480-961-4533 www.rogerscorp.com

Helping power, protect, connect our world™

DATASHEET RO5880

Roger *RO5880* substrate has been used in the design process of the two patches and in their fabrication. The *RO5880* available sample thickness are reported below:

DIELECTRIC THICKNESS	CLADDING THICKNESS
0.015inch = 0.381mm	HH/HH
0.031inch = 0.787mm	1R/1R

Table E.1: RO5880 thickness limitations

The cladding thickness notation meaning is reported in Appendix C. More information on RO5880 is reported in the datasheet shown in the following pages.



RT/duroid® 5870 /5880 High Frequency Laminates



RT/duroid® 5870 and 5880 glass microfiber reinforced PTFE composites are designed for exacting stripline and microstrip circuit applications.

The randomly oriented microfibers result in exceptional dielectric constant uniformity.

The dielectric constant of RT/duroid 5870 and 5880 laminates is uniform from panel to panel and is constant over a wide frequency range.

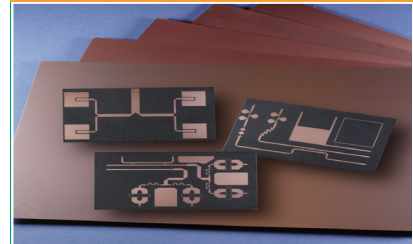
Its low dissipation factor extends the usefulness of RT/duroid 5870 and 5880 laminates to Ku-band and above.

RT/duroid 5870 and 5880 laminates are easily cut, sheared and machined to shape. They are resistant to all solvents and reagents, hot or cold, normally used in etching printed circuits or in plating edges and holes.

Normally supplied as a laminate with electrodeposited copper of $\frac{1}{2}$ to 2 ounces/ft.² (8 to 70 μ m) or reverse treated EDC on both sides, RT/duroid 5870 and 5880 composites can also be clad with rolled copper foil for more critical electrical applications. Cladding with aluminum, copper or brass plate may also be specified.

When ordering RT/duroid 5870 and 5880 laminates, it is important to specify dielectric thickness, tolerance, rolled, electrodeposited or reverse treated copper foil, and weight of copper foil required.

Data Sheet



Features:

- Lowest electrical loss for reinforced PTFE material
- Low moisture absorption
- Isotropic
- Uniform electrical properties over frequency
- Excellent chemical resistance

Some Typical Applications:

- Commercial Airline Broadband Antennas
- Microstrip and Stripline Circuits
- Millimeter Wave Applications
- Military Radar Systems
- Missile Guidance Systems
- Point to Point Digital Radio Antennas

PROPERTY	TYPICAL VALUES				DIRECTION	UNITS ^[3]	CONDITION	TEST METHOD	
	RT/duroid 5870		RT/duroid 5880						
^[1] Dielectric Constant, ϵ_r Process	2.33 2.33 ± 0.02 spec.		2.20 2.20 ± 0.02 spec.		Z Z	N/A	C24/23/50 C24/23/50	1 MHz IPC-TM-650 2.5.5.3 10 GHz IPC-TM 2.5.5.5	
^[4] Dielectric Constant, ϵ_r Design	2.33		2.20		Z	N/A	8 GHz - 40 GHz	Differential Phase Length Method	
Dissipation Factor, tan δ	0.0005 0.0012		0.0004 0.0009		Z Z	N/A	C24/23/50 C24/23/50	1 MHz IPC-TM-650, 2.5.5.3 10 GHz IPC-TM-2.5.5.5	
Thermal Coefficient of ϵ_r	-115		-125		Z	ppm/°C	-50 - 150°C	IPC-TM-650, 2.5.5.5	
Volume Resistivity	2 X 10 ⁷		2 X 10 ⁷		Z	Mohm cm	C96/35/90	ASTM D257	
Surface Resistivity	2 X 10 ⁷		3 X 10 ⁷		Z	Mohm	C/96/35/90	ASTM D257	
Specific Heat	0.96 (0.23)		0.96 (0.23)		N/A	J/g/K (cal/g/C)	N/A	Calculated	
Tensile Modulus	Test at 23 °C	Test at 100 °C	Test at 23 °C	Test at 100 °C	N/A	MPa (kpsi)	A	ASTM D638	
	1300 (189)	490 (71)	1070 (156)	450 (65)	X				
	1280 (185)	430 (63)	860 (125)	380 (55)	Y				
	ultimate stress	50 (7.3)	34 (4.8)	29 (4.2)	20 (2.9)				X
		42 (6.1)	34 (4.8)	27 (3.9)	18 (2.6)				Y
	ultimate strain	9.8	8.7	6.0	7.2				X
	9.8	8.6	4.9	5.8	Y				
Compressive Modulus	1210 (176)	680 (99)	710 (103)	500 (73)	X	MPa (kpsi)	A	ASTM D695	
	1360 (198)	860 (125)	710 (103)	500 (73)	Y				
	803 (120)	520 (76)	940 (136)	670 (97)	Z				
	ultimate stress	30 (4.4)	23 (3.4)	27 (3.9)	22 (3.2)				X
		37 (5.3)	25 (3.7)	29 (5.3)	21 (3.1)				Y
		54 (7.8)	37 (5.3)	52 (7.5)	43 (6.3)				Z
ultimate strain	4.0	4.3	8.5	8.4	X	%			
	3.3	3.3	7.7	7.8	Y				
	8.7	8.5	12.5	17.6	Z				
Moisture Absorption	0.02		0.02		N/A	%	.062" (1.6mm) D48/50	ASTM D570	
Thermal Conductivity	0.22		0.20		Z	W/m/K	80°C	ASTM C518	
Coefficient of Thermal Expansion	22 28 173		31 48 237		X Y Z	ppm/°C	0-100°C	IPC-TM-650, 2.4.41	
Td	500		500		N/A	°C TGA	N/A	ASTM D3850	
Density	2.2		2.2		N/A	gm/cm ³	N/A	ASTM D792	
Copper Peel	27.2 (4.8)		31.2 (5.5)		N/A	pli (N/mm)	1 oz (35µm) EDC foil after solder float	IPC-TM-650 2.4.8	
Flammability	V-0		V-0		N/A	N/A	N/A	UL94	
Lead-Free Process Compatible	Yes		Yes		N/A	N/A	N/A	N/A	

- [1] Specification values are measured per IPC-TM-650, method 2.5.5.5 @ ~10GHz, 23°C. Testing based on 1 oz. electrodeposited copper foil. ϵ_r values and tolerance reported by IPC-TM-650 method 2.5.5.5 are the basis for quality acceptance, but for some products these values may be incorrect for design purposes, especially microstrip designs. We recommend that prototype boards for new designs be verified for desired electrical performance.
- [2] Typical values should not be used for specification limits, except where noted.
- [3] SI unit given first with other frequently used units in parentheses.
- [4] The design Dk is an average number from several different tested lots of material and on the most common thickness/s. If more detailed information is required, please contact Rogers Corporation. Refer to Rogers' technical paper "Dielectric Properties of High Frequency Materials" available at <http://www.rogerscorp.com>.

Standard Thickness		Standard Panel Size	Standard Copper Cladding	Non-Standard Copper Cladding
0.005" (0.127mm)	0.031" (0.787mm)	18" X 12" (457 X 305mm) 18" X 24" (457 X 610mm) Non-standard sizes may be available up to 18" X 48" (457 X 1219 mm)	½ oz. (18µm) and 1 oz. (35µm) electrodeposited and rolled copper foil	¼ oz. (9 µm) electrodeposited copper foil
0.010" (0.254mm)	0.062" (1.575mm)			½ oz. (18µm), 1 oz. (35µm) and 2 oz. (70µm) reverse treat copper foil
0.015" (0.381mm)				2 oz. (70µm) electrodeposited and rolled copper foil
0.020" (0.508mm)				
Non-standard thicknesses are available				
Thick metal claddings may be available based on dielectric and plate thickness. Contact customer service for more information on available non-standard and custom thicknesses, claddings and panel sizes				

The information in this data sheet is intended to assist you in designing with Rogers' circuit materials. It is not intended to and does not create any warranties express or implied, including any warranty of merchantability or fitness for a particular purpose or that the results shown on this data sheet will be achieved by a user for a particular purpose. The user should determine the suitability of Rogers' circuit materials for each application.

These commodities, technology and software are exported from the United States in accordance with the Export Administration regulations. Diversion contrary to U.S. law prohibited.

RT/duroid, Helping power, protect, connect our world and the Rogers' logo are trademarks of Rogers Corporation or one of its subsidiaries.

© 2018 Rogers Corporation, Printed in U.S.A. All rights reserved. Revised 1402 101518 Publication #92-101

Helping power, protect, connect our world

DATASHEET SMA CONNECTOR

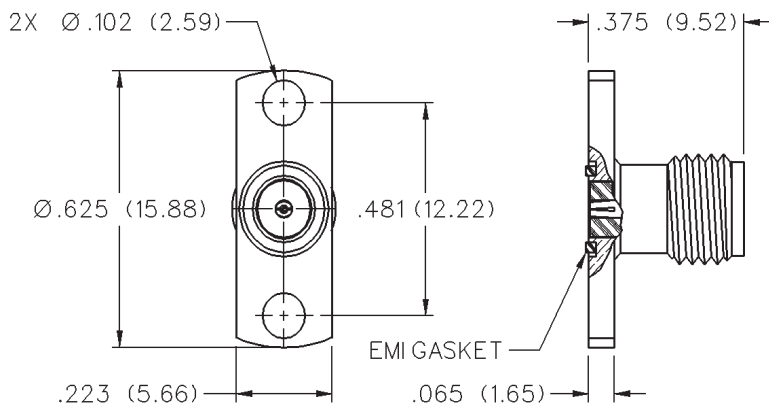
The [SMA](#) is a semi-precision connector for RF and microwave systems that has been developed in the 1960s. The connector has a 50Ω characteristic impedance and usually is designed for use from DC to 18GHz, even if sometimes till 26.5GHz as in the case reported here. For performance above this, other SMA-like connectors are used. In the following pages, the datasheet of the [SMA](#) connector used in the designed antenna is reported. It comprehends a page related to the housing, one to the hermetic seal and the rest to general notes on the 50Ω [SMA](#). Thanks to their working frequency range, from 0 – 26.5GHz, they suits the designed antenna band.

In particular, the seal used is *142-1000-002* that has a pin with radius 0.19mm

50 Ohm SMA Field Replaceable 2-Hole Flange Mount Jack Receptacle - With EMI Gasket



INCHES (MILLIMETERS)
CUSTOMER DRAWINGS AVAILABLE UPON REQUEST

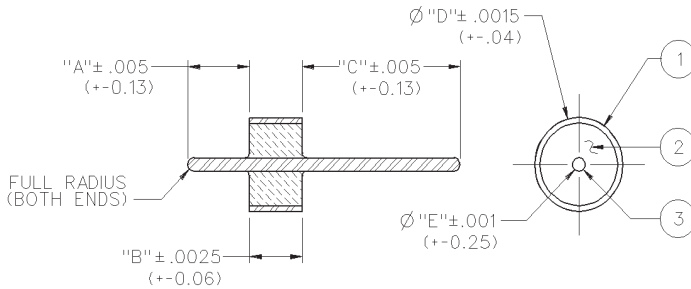


ACCEPTS PIN SIZE	FREQUENCY RANGE	GOLD PLATED	NICKEL PLATED
.015 (0.38)	0-26.5 GHz	142-1701-611	142-1701-616

Hermetic Seal Feedthrough



INCHES (MILLIMETERS)
CUSTOMER DRAWINGS AVAILABLE UPON REQUEST



Recommended Mounting Hole Detail

PART NUMBER	ITEM 1 OUTER RING	ITEM 2 INSULATOR	ITEM 3 PIN	"A"	"B"	"C"	"D"	"E"
142-1000-001	Kovar Gold pl .00005 min over Nickel pl .000005 min.	Glass Corning 7052 or equivalent	Kovar Gold pl .00005 min over Nickel pl .000005 min	.070 (1.78)	.0625 (1.59)	.180 (4.57)	.0985 (2.50)	.012 (.30)
142-1000-002	Kovar Gold pl .00005 min over Nickel pl .000005 min.	Glass Corning 7070 or equivalent	Kovar Gold pl .00005 min over Nickel pl .000005 min	.072 (1.83)	.0625 (1.59)	.180 (4.57)	.0985 (2.50)	.015 (.38)
142-1000-003	Kovar Gold pl .00005 min over Nickel pl .000005 min.	Glass Corning 7070 or equivalent	Kovar Gold pl .00005 min over Nickel pl .000005 min	.072 (1.83)	.0600 (1.52)	.180 (4.57)	.1100 (2.79)	.018 (.46)
142-1000-004	Kovar Gold pl .00005 min over Nickel pl .000005 min.	Glass Corning 7052 or equivalent	Kovar Gold pl .00005 min over Nickel pl .000005 min	.070 (1.78)	.0600 (1.52)	.203 (5.16)	.1580 (4.01)	.020 (.51)

Mounting Hole Dimensions

PART NUMBER	PIN DIAMETER	"F"	"G"	AIR	TEFLON
				"H"	"H"
142-1000-001	.012 (0.30)	.063 (1.60)	.102 (2.59)	.028 (0.71)	.039 (0.99)
142-1000-002	.015 (0.38)	.063 (1.60)	.102 (2.59)	.035 (0.89)	.049 (1.24)
142-1000-003	.018 (0.46)	.060 (1.52)	.114 (2.90)	.042 (1.07)	.059 (1.50)
142-1000-004	.020 (0.51)	.060 (1.52)	.162 (4.11)	.046 (1.17)	.065 (1.65)

Notes:

- ⚠ The hermetic seal should be mounted as flush as possible with the housing. Excessive recession will create a high impedance air gap which degrades electrical performance.
- ⚠ The use of an additional counterbore to accommodate a solder ring for seal mounting is not recommended. A slight chamfer may be used if care is taken to completely fill the area with solder - **avoid air gaps**.
- ⚠ Dimensions shown are given to achieve 50 Ohms with either air or a teflon insulator. A teflon insulator may be helpful in supporting small pin diameters.

Electrical:

Impedance: 50 Ohms
 Frequency Range: DC to 26.5 GHz
 VSWR: Dependent upon application
 Working Voltage: 250 Vrms max at sea level
 Dielectric Withstanding Voltage: 500 Vrms min at sea level
 Insulation Resistance: 5000 Megohm min
 Insertion Loss: .015F dB max (F in GHz)

Environmental:

Hermeticity: 1x10⁻⁸ cc/sec at one atmosphere
 Solderability: MIL-STD-202, Method 209
 Operating Temperature: -55° C to 165° C

Cinch Connectivity Solutions

299 Johnson Avenue SW, Waseca, MN 56093 USA • 800.247.8256 • +1 507 833 8822 • cinchconnectivity.com

SMA - 50 Ohm Connectors



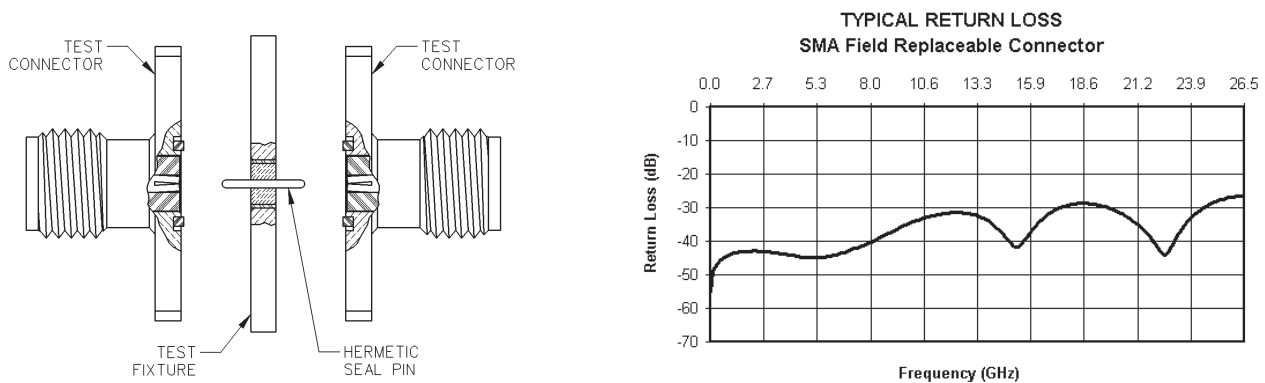
Field Replaceable - Application Notes

INCHES (MILLIMETERS)
CUSTOMER DRAWINGS AVAILABLE UPON REQUEST

The field replaceable style of connector is known by many names in the industry, such as MIC launcher, hermetic seal launcher, spark plug launcher, etc. Some types, such as those known as "spark plugs", have the hermetic seal incorporated into the connector. These types require special welding to install and can not be replaced without destroying the hermeticity of the circuit housing. True field replaceable connectors, such as those manufactured by Johnson Components™, are easy to install and replace. Because the hermetic seal is not incorporated into the connector design, the connector can be removed and replaced without destroying the hermetic seal or the hermeticity of the circuit housing.

All of the above mentioned connector types perform the same basic function - creating a transition from microstrip circuitry to a coaxial transmission line. Whenever possible, the hermetic seal pin diameter should be chosen as close as possible to the microstrip trace width. For optimum electrical performance, the transition from the hermetic seal to the microstrip trace must be properly compensated. Compensation involves adjusting the microstrip trace width to minimize any impedance discontinuities found in the transition area.

The plot shown below is representative of the typical return loss of an Johnson Components™ field replaceable connector. To produce the data shown below, a test fixture is created using the appropriate Johnson Components™ hermetic seal. The fixture consists of a suitably thick spacer plate with the hermetic seal mounted flush to both surfaces. Two connectors are mounted back to back around the fixture and the VSWR of this test assembly is measured. The return loss data shown is equivalent to the square root of the measured VSWR of the test assembly. Since the connectors tested are of identical design, it can be stated with fair accuracy that the data shown represents the response of a single field replaceable connector and its transition to the hermetic seal.



Although Johnson Components™ does not publish a VSWR specification for field replaceable connectors, typical connector VSWR can be expected to be less than $1.1 + .01f$ (f in GHz). A VSWR specification is not stated because an industry standard method for testing field replaceable connectors does not exist. The actual performance of the connector is dependent upon the application for the following reasons:

1. The choice of hermetic seal to be used by the customer is not specified by the connector manufacturer. Hermetic seals produced by different manufacturers will not have the same electrical characteristics. For optimum electrical performance, Johnson Components™ recommends the use of our standard 142-1000-001, 002, 003 and 004 hermetic seals for pin diameters of .012 (0.30), .015 (0.38), .018 (0.46) and .020 (0.51). Custom hermetic seal configurations can be quoted.
2. It is recommended that the hermetic seal be mounted flush with the circuit housing. Tolerance variations between the hermetic seal and machined housing do not always guarantee an optimum transition to the connector. Some manufacturers recommend an additional counterbore in the circuit housing to accommodate a solder washer during installation of the seal. Johnson Components™ does not recommend this type of installation because if the counterbore is not completely filled with solder, electrical discontinuities may be created.
3. The transition between the hermetic seal pin and the microstrip trace will affect electrical performance, as stated above. Several different methods of hermetic seal mounting and seal pin to microstrip trace attachment are used in the industry. Johnson Components™ can not recommend one method over the other as this is dependent upon the customer's application.

As always, quotes for non-standard field replaceable connectors and/or hermetic seals are welcome.

SMA - 50 Ohm Connectors

Specifications



INCHES (MILLIMETERS)
CUSTOMER DRAWINGS AVAILABLE UPON REQUEST

ELECTRICAL RATINGS

Impedance: 50 ohms

Frequency Range:

Dummy loads	0-2 GHz
Flexible cable connectors	0-12.4 GHz
Uncabled receptacles, RA semi-rigid and adapters	0-18.0 GHz
Straight semi-rigid cable connectors and field replaceable connectors	0-26.5 GHz

VSWR: (f = GHz)

	Straight Cabled Connectors	Right Angle Cabled Connectors
RG-178 cable	1.20 + .025f	1.20 + .03f
RG-316, LMR-100 cable	1.15 + .02f	1.15 + .03f
RG-58, LMR-195 cable	1.15 + .01f	1.15 + .02f
RG-142 cable	1.15 + .01f	1.15 + .02f
LMR-200, LMR-240 cable	1.10 + .03f	1.10 + .06f
.086 semi-rigid	1.07 + .008f	1.18 + .015f
.141 semi-rigid (w/contact)	1.05 + .008f	1.15 + .015f
.141 semi-rigid (w/o contact)	1.035 + .005f	
Jack-bulkhead jack adapter and plug-plug adapter		1.05 + .01f
Jack-jack adapter and plug-jack adapter		1.05 + .005f
Uncabled receptacles, dummy loads		N/A
Field replaceable (see page 59)		N/A

Working Voltage: (Vrms maximum)[§]

Connectors for Cable Type	Sea Level	70K Feet
RG-178	170	45
RG-316; LMR-100, 195, 200	250	65
RG-58, RG-142, LMR-240, .086 semi-rigid, uncabled receptacles, .141 semi-rigid w/o contact ...	335	85
.141 semi-rigid with contact and adapters	500	125
Dummy loads		N/A

Dielectric Withstanding Voltage: (VRMS minimum at sea level)[§]

Connectors for RG-178	500
Connectors for RG-316; LMR-100, 195, 200	750
Connectors for RG-58, RG-142, LMR-240, .086 semi-rigid, field replaceable, uncabled receptacles	1000
Connectors for .141 semi-rigid with contact and adapters	1500
Connectors for .141 semi-rigid w/o contact, dummy loads	N/A

Corona Level: (Volts minimum at 70,000 feet)[§]

Connectors for RG-178	125
Connectors for RG-316; LMR-100, 195, 200	190
Connectors for RG-58, RG-142, LMR-240, .086 semi-rigid, uncabled receptacles, .141 semi-rigid w/o contact	250
Connectors for .141 semi-rigid with contact and adapters	375
Dummy loads	N/A

Insertion Loss: (dB maximum)

Straight flexible cable connectors and adapters	0.06	\sqrt{f} (GHz), tested at 6 GHz
Right angle flexible cable connectors	0.15	\sqrt{f} (GHz), tested at 6 GHz
Straight semi-rigid cable connectors with contact	0.03	\sqrt{f} (GHz), tested at 10 GHz
Right angle semi-rigid cable connectors	0.05	\sqrt{f} (GHz), tested at 10 GHz
Straight semi-rigid cable connectors w/o contact	0.03	\sqrt{f} (GHz), tested at 16 GHz
Straight low loss flexible cable connectors	0.06	\sqrt{f} (GHz), tested at 1 GHz
Right Angle low loss flexible cable connectors	0.15	\sqrt{f} (GHz), tested at 1 GHz
Uncabled receptacles, field replaceable, dummy loads		N/A

Insulation Resistance: 5000 megohms minimum

Contact Resistance: (milliohms maximum)	Initial	After Environmental
Center contact (straight cabled connectors and uncabled receptacles)	3.0*	4.0*
Center contact (right angle cabled connectors and adapters)	4.0	6.0
Field replaceable connectors	6.0	8.0
Outer contact (all connectors)	2.0	N/A
Braid to body (gold plated connectors)	0.5	N/A
Braid to body (nickel plated connectors)	5.0	N/A

*N/A where the cable center conductor is used as a contact

RF Leakage: (dB minimum, tested at 2.5 GHz)

Flexible cable connectors, adapters and .141 semi-rigid connectors w/o contact	-60 dB
Field replaceable w/o EMI gasket	-70 dB
.086 semi-rigid connectors and .141 semi-rigid connectors with contact, and field replaceable with EMI Gasket	-90 dB
Two-way adapters	-90 dB
Uncabled receptacles, dummy loads	N/A

RF High Potential Withstanding Voltage: (Vrms minimum, tested at 4 and 7 MHz)[§]

Connectors for RG-178	335
Connectors for RG-316; LMR-100, 195, 200	500
Connectors for RG-58, RG-142, LMR-240, .086 semi-rigid, .141 semi-rigid cable w/o contact, uncabled receptacles	670
Connectors for .141 semi-rigid with contact and adapters	1000

Power Rating (Dummy Load): 0.5 watt @ + 25°C, derated to 0.25 watt @ +125°C

MECHANICAL RATINGS

Engagement Design: MIL-C-39012, Series SMA

Engagement/Disengagement Force: 2 inch-pounds maximum

Mating Torque: 7 to 10 inch-pounds

Bulkhead Mounting Nut Torque: 15 inch-pounds

Coupling Proof Torque: 15 inch-pounds minimum

Coupling Nut Retention: 60 pounds minimum

Contact Retention:

6 lbs. minimum axial force (captivated contacts)

4 inch-ounce minimum torque (uncabled receptacles)

Cable Retention:

Axial Force*(lbs) Torque (in-oz)

Connectors for RG-178	10	N/A
Connectors for RG-316, LMR-100	20	N/A
Connectors for LMR-195, 200	30	N/A
Connectors for RG-58, LMR-240	40	N/A
Connectors for RG-142	45	N/A
Connectors for .086 semi-rigid	30	16
Connectors for .141 semi-rigid	60	55

*Or cable breaking strength whichever is less.

Durability: 500 cycles minimum

100 cycles minimum for .141 semi-rigid connectors w/o contact

(Meets or exceed the applicable paragraph of MIL-C-39012)

Temperature Range: - 65°C to + 165°C

Thermal Shock: MIL-STD-202, Method 107, Condition B

Corrosion: MIL-STD-202, Method 101, Condition B

Shock: MIL-STD-202, Method 213, Condition I

Vibration: MIL-STD-202, Method 204, Condition D

Moisture Resistance: MIL-STD-202, Method 106

†Avoid user injury due to misapplication. See safety advisory definitions inside front cover.

Cinch Connectivity Solutions

299 Johnson Avenue SW, Waseca, MN 56093 USA • 800.247.8256 • +1 507 833 8822 • cinchconnectivity.com

SMA - 50 Ohm Connectors

Specifications



INCHES (MILLIMETERS)
CUSTOMER DRAWINGS AVAILABLE UPON REQUEST

MATERIAL SPECIFICATIONS

Bodies: Brass per QQ-B-626, gold plated* per MIL-G-45204 .00001" min. or nickel plated per QQ-N-290

Contacts: Male - brass per QQ-B-626, gold plated per MIL-G-45204 .00003" min.

Female - beryllium copper per QQ-C-530, gold plated per MIL-G-45204 .00003" min.

Nut Retention Spring: Beryllium copper per QQ-C-533. Unplated

Insulators: PTFE fluorocarbon per ASTM D 1710 and ASTM D 1457 or Tefzel per ASTM D 3159 or PFA 340 per ASTM

Expansion Caps: Brass per QQ-B-613, gold plated per MIL-G-45204 .00001" min. or nickel plated per QQ-N-290

Crimp Sleeves: Copper per WW-T-799 or brass per QQ-B-613, gold plated per MIL-G-45204 .00001" min. or nickel plated per QQ-N-290

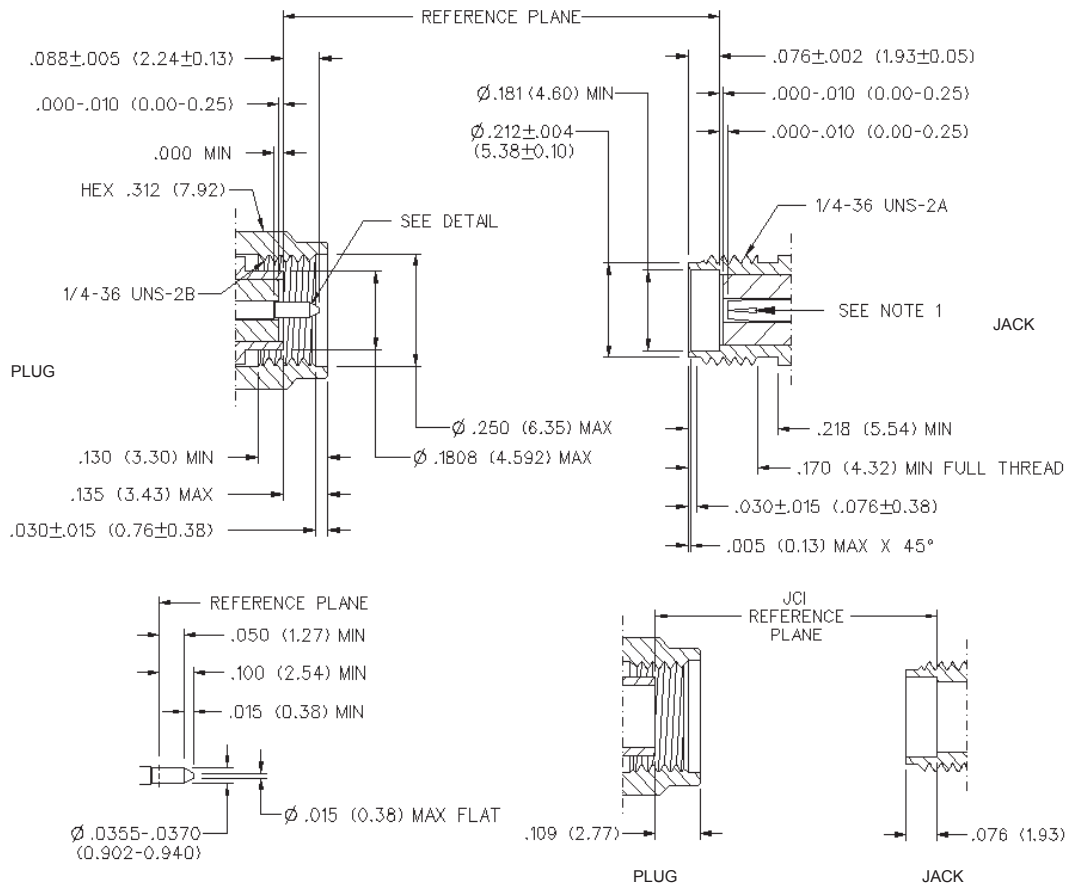
Mounting Hardware: Brass per QQ-B-626 or QQ-B-613, gold plated per MIL-G-45204 .00001" min. or nickel plated per QQ-N-290

Seal Rings: Silicone rubber per ZZ-R-765

EMI Gaskets: Conductive silicone rubber per MIL-G-83528, Type M

* All gold plated parts include a .00005" min. nickel underplate barrier layer.

Mating Engagement for SMA Series per MIL-C-39012



NOTES

1. ID OF CONTACT TO MEET VSWR, CONTACT RESISTANCE AND INSERTION WITHDRAWAL FORCES WHEN MATED WITH DIA .0355-.0370 MALE PIN.

Cinch Connectivity Solutions

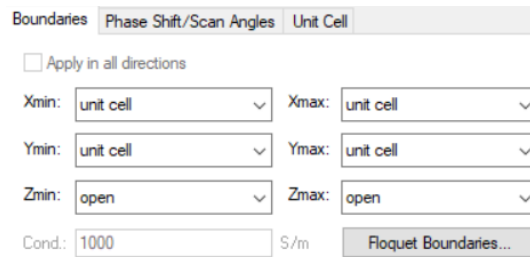
299 Johnson Avenue SW, Waseca, MN 56093 USA • 800.247.8256 • +1 507 833 8822 • cinchconnectivity.com

SIMULATION MESH AND ACCURACY

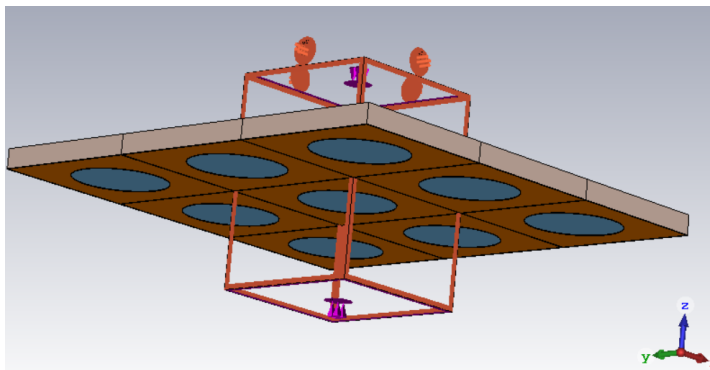
In this appendix chapter, the mesh and accuracy for the most relevant simulations, performed with the commercial software CST Microwave Studio, are reported.

G.1 UNIT CELL

To simulate the unit cell behavior, its boundary conditions have been defined. Because of the PRS periodicity along x - and y -axis, in these coordinates the conditions have been set on "unit cell", Fig. G.1a. In this way, the unit cell is infinitely repeated in the (x,y) plane as showed in Fig. G.1b.



(a)



(b)

Figure G.1: Unit cell boundary conditions. In (a) the boundary settings along x , y and z are reported. On the other hand, the model analyzed by the software is shown in (b).

Along z -axis, the boundary has been set "open" which means that it extends the touching geometry, air space above the dielectric layer, virtually to infinity by using a perfectly matched layer boundary. Waves can pass through this boundary with minimal reflections. This configuration generates two Floquet ports in the project that are

attached to the Z_{max} and Z_{min} open boundaries, Fig. G.2. These ports have a set of modes, called Floquet modes, that represents the fields on the port boundary. They are basically plane waves with the direction of propagation set by the periodic structure frequency, phasing and geometry. For these reason, this modes are analogous to the waveguide port one: they are characterized by a propagation constant and a cut-off frequency.

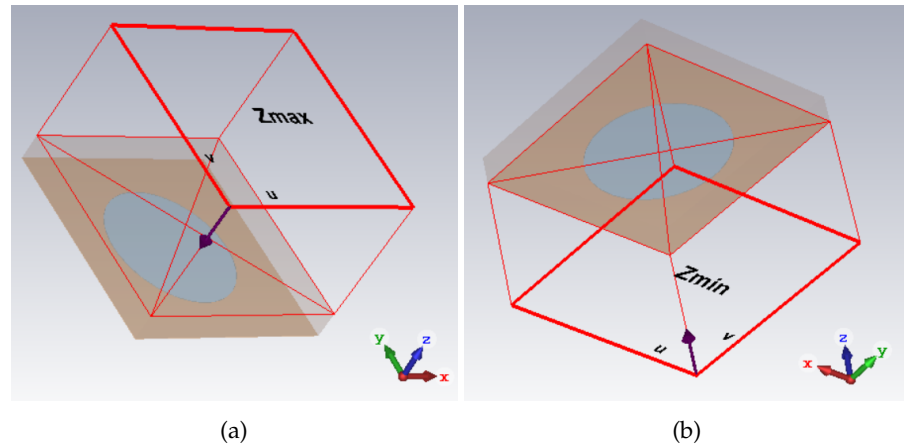


Figure G.2: Floquet ports above, (a), and below, (b), the PRS unit cell.

Because of the frequency band of interest is 18-28GHz, the chosen central frequency is at 23GHz. Above and below the unit cell, an air space of $\lambda_0/4$, with $\lambda_0 = c/f = 0.013\text{m}$, has been considered. In this way, two reference planes, on which the open boundary conditions lay, have been defined. Starting from these two planes, the Floquet ports have been placed attached to the upper and bottom PRS sides. The unit cell has then been simulated in order to find a single resonance in 18-28GHz band, as showed in Fig. 5.10b, considering just the fundamental mode for the plane-wave coming from the Z_{min} port, Fig. G.4a. The Z_{min} port represents the radiating source in the FPC structure, for example a slot.

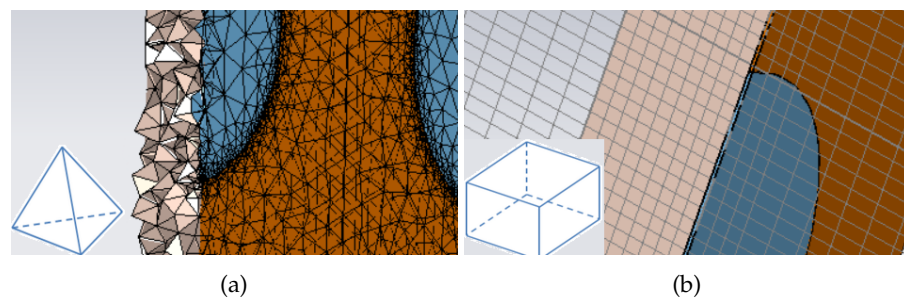


Figure G.3: (a) and (b) shows a hexahedral or tetrahedral mesh for the unit cell, respectively.

The unit cell is subdivided by the solver into discrete geometric cells in order to study its behavior. The mesh type can be hexahedral or tetrahedral, as showed in Fig. G.3. For this simulation and for the following ones, a tetrahedral mesh has been preferred due to the presence of the circular holes in the PRS metal sheet.

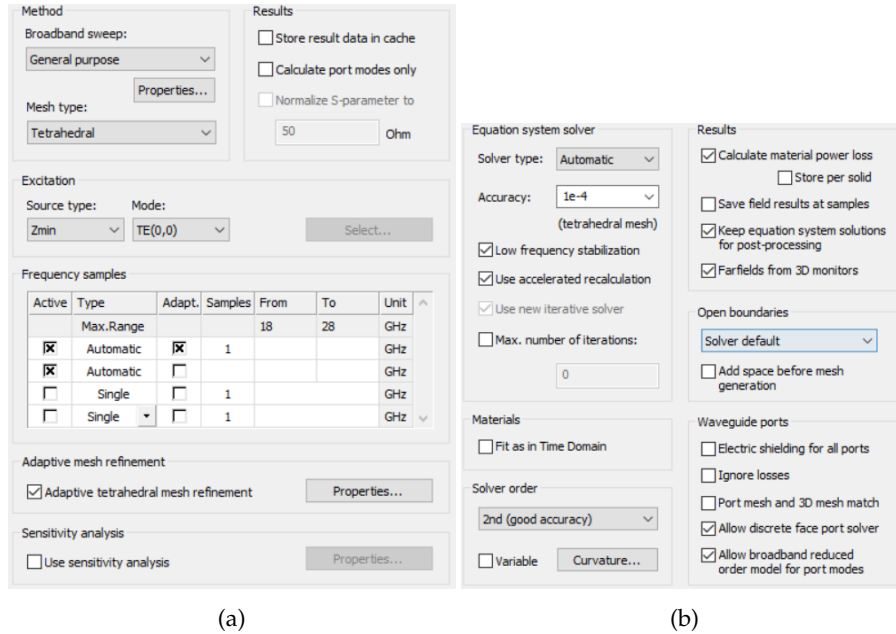


Figure G.4: The frequency domain solver has been set to take into account just the excitation coming from Z_{min} , (a). In (b) the simulation accuracy is reported.

The "General purpose" broadband frequency sweep has been chosen to derive the full spectrum behavior instead of "Fast reduced order model", that generates broadband results from very few equation system solver runs, or "Discrete samples only", that analyzes few specific frequencies.

Moreover, the "General purpose" analysis solves the linear equation system using the iterative solver or the sparse direct one and the solution comprises the field distribution as well as S-parameters and derived quantities.

In Fig. G.5, an high number has been set for the "Cells per wavelength" parameter that defines the upper limit to the cell size with respect to the wavelength and the spatial sampling rate for the signals inside the structure. Having an high value, due to its strong influence on both quality of the results and calculation time, leads to a higher accuracy. However, the total calculation time increases too but, for a unit cell that has a small structure, it is in any case really short. The "Minimum cell" size can be used to avoid over-refinement due to very high curvatures. It can be defined by choosing a number for the "absolute value" setting or by dividing the maximum cell size by a chosen number for the "Fraction of maximum cell in the model" case. In this project case, the minimum cell absolute value has been chosen equal to 0 because no

over-refinement problems have been found. Moreover, a better mesh can be obtained by working on two other parameters reported in Fig. G.5b. Through the "Smooth mesh with equilibrate ratio", the mesh smoothing can be controlled to improve the generated mesh quality. It represents the maximum ratio between the lengths of two adjacent edges and closer to 1 it is, smoother the resulting mesh will be. On the other hand, "automatic edge refinement step width" defines the refinement around edges of planar faces oriented in Z direction: if set on 0, it is disabled. For this thesis, the default values for both these parameter have been considered.

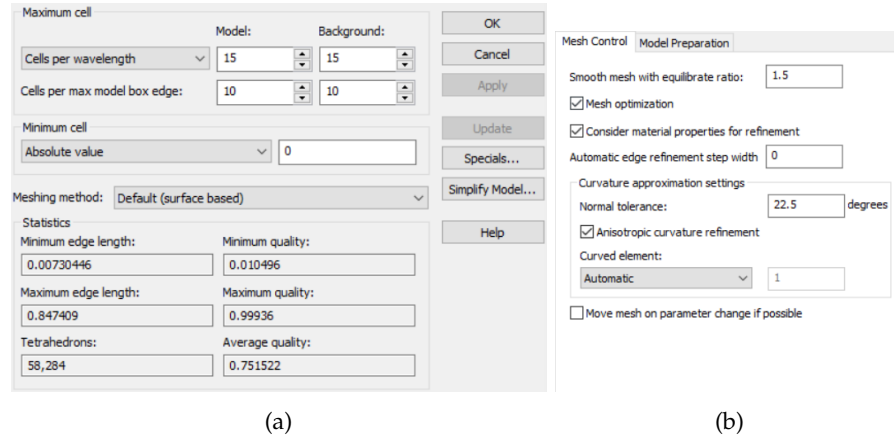


Figure G.5: Mesh properties and number of cells overview.

The resulting mesh view, with settings defined as discussed above, is reported in Fig. G.6. While on the dielectric substrate the mesh is uniform, close to the circular hole it is more dense allowing a good simulation accuracy.

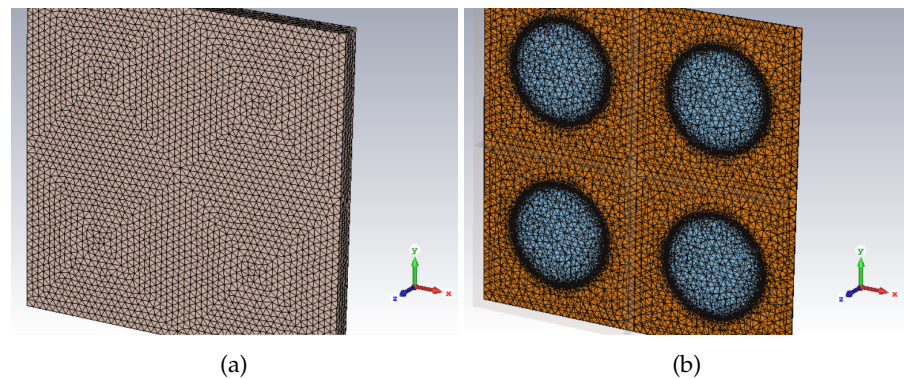
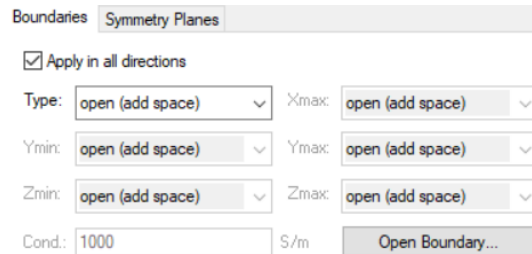


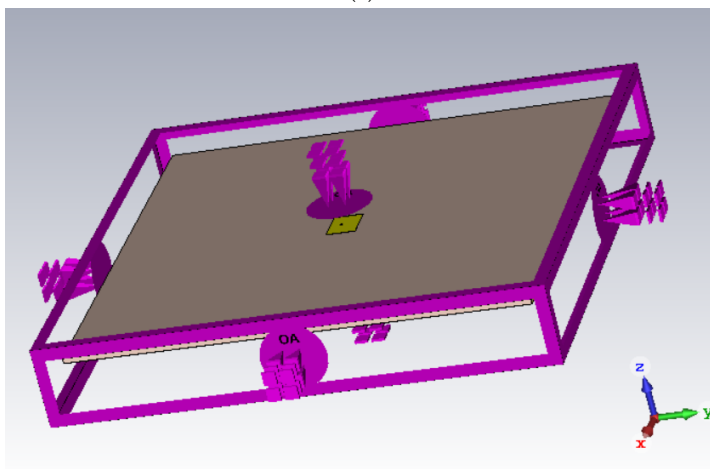
Figure G.6: Mesh view of the PRS dielectric substrate, (a), and of its metal sheet patterned with circular holes, (b).

G.2 RADIATING SOURCE

Differently from the unit cell case, the structure has a finite extension and it is not periodic anymore. For this reason, open boundaries have been set along each axis to analyze the radiating source, Fig. G.7.



(a)



(b)

Figure G.7: Radiating source boundary conditions. In (a), the boundary settings along x , y and z are reported. On the other hand, the model analyzed by the software is shown in (b).

In particular, the option "*Open (add space)*", Fig. G.7a, has been chosen instead of the "*Open*" one because it adds some extra space for farfield calculation. For the analysis, a wave-guide port has been attached to the coaxial cable that excites the patch as shown in Fig. G.8c. For the slot case the procedure is analogous: the port has been attached to the rectangular wave-guide that feeds the structure. As shown in Fig. G.8a and G.8b, the mesh is more dense between the patch and the coaxial cable pin to provide a better analysis of the patch behavior. A dense number of cells is also present between the ground plane and the cable external coating. The total number of mesh and the simulations settings, whose specific one remained the same shown in Fig. G.5b and G.4b, are reported in Fig. G.9.

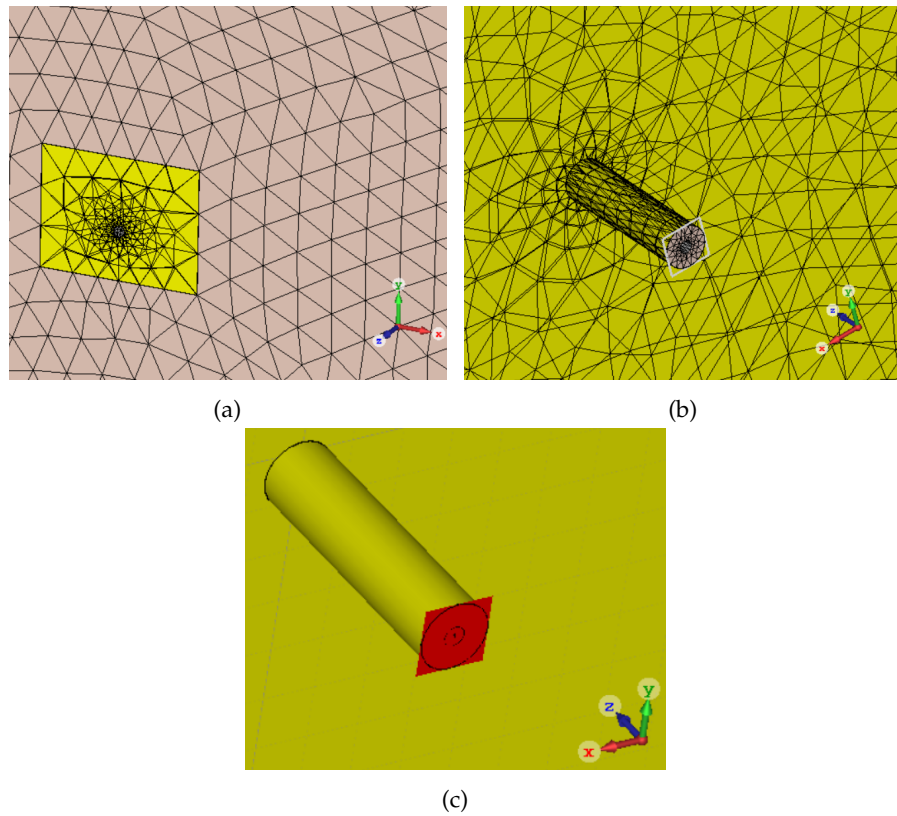


Figure G.8: In (a) and (b) the structure mesh view is reported. On the other hand, (c) shows the waveguide port location.

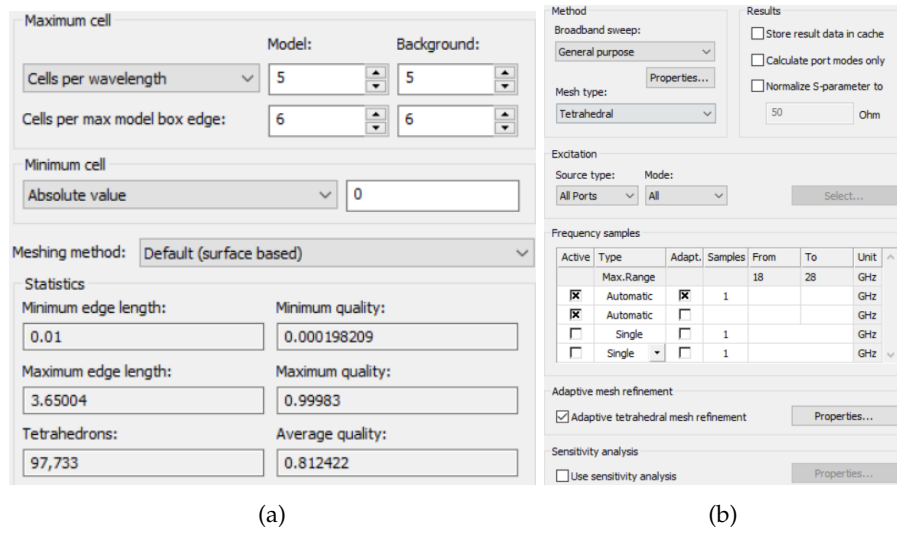


Figure G.9: Mesh properties and frequency domain solver overview.

G.3 SINGLE FED STRUCTURE

Before analyzing the structure with two feeding, the one with just a feed has been simulated to check its behavior and matching. Some

settings have been maintained, such as the "Open (add space)" boundaries and the frequency domain solver settings shown in Fig. G.9b and G.4b. The mesh view and settings are reported as follows:

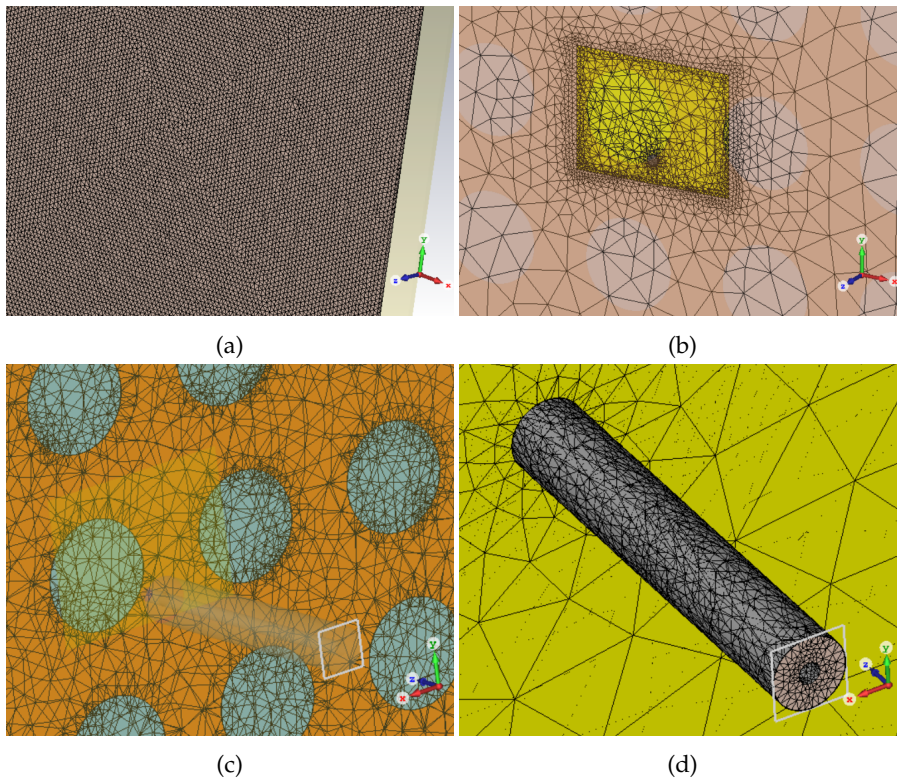


Figure G.10: Mesh view of the single fed structure. In (a) and (c), the PRS mesh is presented while in (b) and (d) the patch one is reported.

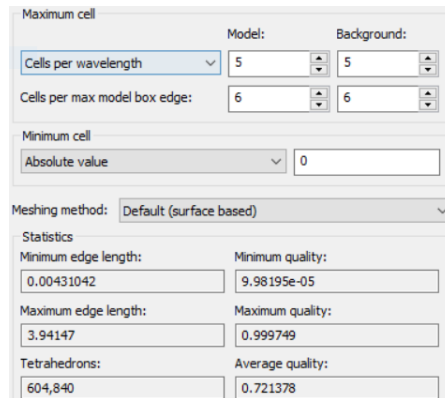


Figure G.11: Mesh settings and number of cells overview.

In this case the mesh for the patch is dense also along its edge for a better analysis of its radiation and scattering behavior. The PRS mesh is uniform on the substrate while for the metal sheet is more dense close to the circular hole.

G.4 DOUBLE FED STRUCTURE

In this last analysis, another radiating element with its own feeding line has been considered and so added to the previous structure. The settings for the single feeding case have been maintained and the mesh view and setup are reported as follows:

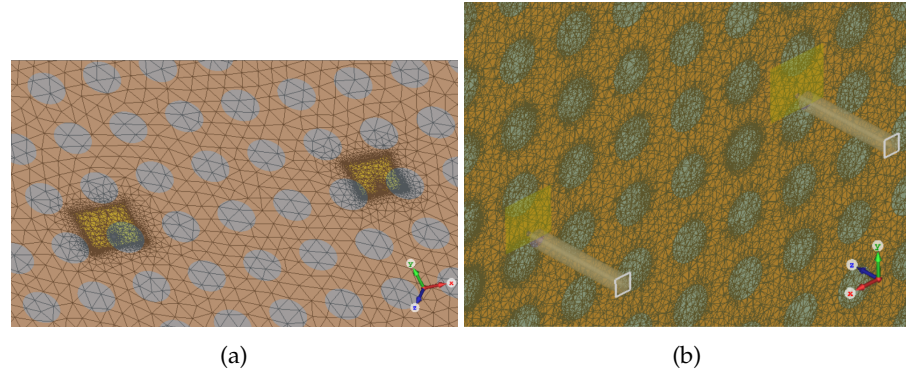


Figure G.12: Mesh view of the double fed structure. In (a) the focus is on the radiating sources while the metal sheet is reported in (b).

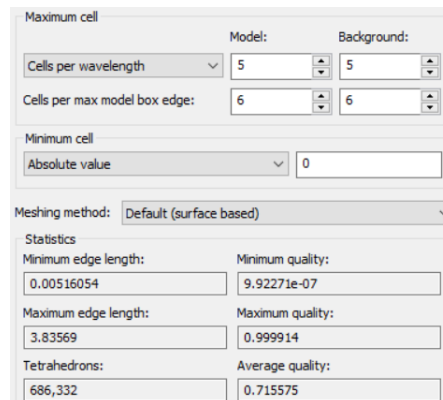


Figure G.13: Mesh settings and number of cells overview.

The mesh cells for the radiating elements are more dense close to the patches while moving away from them the number of cells become sparse because the dielectric is uniform. The mesh cells on the PRS are generated in the same way by the solver: dense close to the holes in the metal sheet while uniform and sparse on the dielectric substrate.

BIBLIOGRAPHY

- [1] M. T. Cicero. *M. Tulli Ciceronis de Divinatione: libri duo: Eiusdem liber de Fato; Cum codicibus Harleianis contulit atque emendavit Henricus Alanus*. Fellow, 1839.
- [2] J. Du Preez and S. Sinha. *Millimeter-wave antennas: configurations and applications*. Springer, 2016.
- [3] A. Boriskin and R. Sauleau. *Aperture antennas for millimeter and sub-millimeter wave applications*. Springer, 2018.
- [4] S. Kang, J. Chien, and A. M. Niknejad. "A W-band low-noise PLL with a fundamental VCO in SiGe for millimeter-wave applications." In: *IEEE Transactions on Microwave Theory and Techniques* 62.10 (2014), pp. 2390–2404.
- [5] A. Hajimiri. "MM-Wave silicon ICs: Challenges and opportunities." In: *2007 IEEE Custom Integrated Circuits Conference*. IEEE, 2007, pp. 741–747.
- [6] H. Wang and K. Sengupta. *RF and mm-Wave Power Generation in Silicon*. Academic Press, 2015.
- [7] A. T. Almutawa, A. Hosseini, D. R. Jackson, and F. Capolino. "Leaky-Wave Analysis of Wideband Planar Fabry-Pérot Cavity Antennas Formed by a Thick PRS." In: *IEEE Transactions on Antennas and Propagation* (2019).
- [8] R. Gardelli, M. Albani, and F. Capolino. "Array thinning by using antennas in a Fabry-Pérot cavity for gain enhancement." In: *IEEE Transactions on Antennas and Propagation* 54.7 (2006), pp. 1979–1990.
- [9] IEEE. "IEEE Standard for Definitions of Terms for Antennas." In: *IEEE Std 145-2013 (Revision of IEEE Std 145-1993)* (2014), pp. 1–50. ISSN: null. DOI: [10.1109/IEEESTD.2014.6758443](https://doi.org/10.1109/IEEESTD.2014.6758443).
- [10] C. A. Balanis. *Antenna theory: analysis and design*. John Wiley & Sons, 2016.
- [11] D. R. Jackson, P. Burghignoli, G. Lovat, F. Capolino, J. Chen, D. R. Wilton, and A. A. Oliner. "The fundamental physics of directive beaming at microwave and optical frequencies and the role of leaky waves." In: *Proceedings of the IEEE* 99.10 (2011), pp. 1780–1805.
- [12] W. W. Hansen. *Radiating electromagnetic wave guide*. US Patent 2,402,622. 1946.
- [13] N. Marcuvitz. "On field representations in terms of leaky modes or eigenmodes." In: *IRE transactions on antennas and propagation* 4.3 (1956), pp. 192–194.

- [14] L. Goldstone and A. A. Oliner. "Leaky-wave antennas I: Rectangular waveguides." In: *IRE Transactions on Antennas and Propagation* 7.4 (1959), pp. 307–319.
- [15] J. N. Hines and J. R. Upson. "A wide aperture tapered-depth scanning antenna." In: *Ohio State Univ. Res. Found* (1957), pp. 667–7.
- [16] W. Rotman and A. A. Oliner. "Asymmetrical trough waveguide antennas." In: *IRE Transactions on Antennas and Propagation* 7.2 (1959), pp. 153–162.
- [17] A. A. Oliner and T. Tamir. "Guided complex waves. part i: fields at an interface (Traveling wave propagation guided along radiation field of open and closed radiating structures)." In: (1962).
- [18] A. A. Oliner and T. Tamir. "Guided complex wave, part II: relation to radiation pattern." In: *Proc. IEE* 110 (1963), pp. 325–334.
- [19] A. A. Oliner. *Scannable millimeter wave arrays*. Rome Air Development Center, Air Force Systems Command, 1989.
- [20] G. Von Trentini. "Partially reflecting sheet arrays." In: *IRE Transactions on Antennas and Propagation* 4.4 (1956), pp. 666–671.
- [21] N. Alexopoulos and D. R. Jackson. "Fundamental superstrate (cover) effects on printed circuit antennas." In: *IEEE Transactions on antennas and propagation* 32.8 (1984), pp. 807–816.
- [22] D. R. Jackson and N. Alexopoulos. "Gain enhancement methods for printed circuit antennas." In: *IEEE transactions on antennas and propagation* 33.9 (1985), pp. 976–987.
- [23] D. R. Jackson and A. A. Oliner. "A leaky-wave analysis of the high-gain printed antenna configuration." In: *IEEE Transactions on Antennas and Propagation* 36.7 (1988), pp. 905–910.
- [24] D. R. Jackson, A. A. Oliner, and A. Ip. "Leaky-wave propagation and radiation for a narrow-beam multiple-layer dielectric structure." In: *IEEE Transactions on Antennas and Propagation* 41.3 (1993), pp. 344–348.
- [25] A. P. Feresidis and J. C. Vardaxoglou. "High gain planar antenna using optimised partially reflective surfaces." In: *IEE Proceedings-Microwaves, Antennas and Propagation* 148.6 (2001), pp. 345–350.
- [26] Ti. Zhao, D. R. Jackson, J. T. Williams, H.-Y.D. Yang, and A. A. Oliner. "2-D periodic leaky-wave antennas-part I: metal patch design." In: *IEEE Transactions on Antennas and Propagation* 53.11 (2005), pp. 3505–3514.

- [27] T. Zhao, D. R. Jackson, and J. T. Williams. "2-D periodic leaky-wave antennas-Part II: Slot design." In: *IEEE Transactions on Antennas and Propagation* 53.11 (2005), pp. 3515–3524.
- [28] M. V. Kuznetsov, V. G.-G. Buendía, Z. Shafiq, L. Matekovits, D. E. Anagnostou, and S. K. Podilchak. "Printed Leaky-Wave Antenna With Aperture Control Using Width-Modulated Microstrip Lines and TM Surface-Wave Feeding by SIW Technology." In: *IEEE Antennas and Wireless Propagation Letters* 18.9 (2019), pp. 1809–1813.
- [29] D. R. Jackson, C. Caloz, and T. Itoh. "Leaky-wave antennas." In: *Proceedings of the IEEE* 100.7 (2012), pp. 2194–2206.
- [30] F. Gross. *Frontiers in antennas: next generation design & engineering*. McGraw Hill Professional, 2010.
- [31] C. A. Balanis. *Modern antenna handbook*. John Wiley & Sons, 2011.
- [32] G. Lovat, P. Burghignoli, and D. R. Jackson. "Fundamental properties and optimization of broadside radiation from uniform leaky-wave antennas." In: *IEEE Transactions on Antennas and Propagation* 54.5 (2006), pp. 1442–1452.
- [33] H. G. Booker. "Slot aerials and their relation to complementary wire aerials (Babinet's principle)." In: *Journal of the Institution of Electrical Engineers-Part IIIA: Radiolocation* 93.4 (1946), pp. 620–626.
- [34] J. L. Volakis, R. C. Johnson, and H. Jasik. "Antenna engineering handbook." In: (2007).
- [35] Shubhendu Bhardwaj and Yahya Rahmat-Samii. "Revisiting the generation of cross-polarization in rectangular patch antennas: A near-field approach." In: *IEEE Antennas and Propagation Magazine* 56 (2014), pp. 14–38.
- [36] S. Sengupta, D. R. Jackson, A. T. Almutawa, H. Kazemi, F. Capolino, and S. A. Long. "Radiation Properties of a 2-D Periodic Leaky-Wave Antenna." In: *IEEE Transactions on Antennas and Propagation* 67.6 (2019), pp. 3560–3573.
- [37] *Attenuation by atmospheric gases*. ITU-R. 2012. URL: https://www.itu.int/dms_pubrec/itu-r/rec/p/R-REC-P.676-9-201202-S!!PDF-E.pdf.
- [38] D. M. Pozar. *Microwave engineering*. John Wiley & Sons, 2012.
- [39] *RO3200TM Series Circuit Materials RO3203TM, RO3206TM and RO3210TM High Frequency Circuit Laminates*. Rogers Corporation. 2011. URL: https://www.midwestpcb.com/data_sheets/RogersR03210.pdf.

- [40] *RO4360G2TM High Frequency Laminates*. Rogers Corporation. 2017.
URL: <https://www.rogerscorp.com/-/media/project/rogerscorp/documents/advanced-connectivity-solutions/english/data-sheets/ro4360g2-high-frequency-laminates-data-sheet.pdf>.
- [41] *TMM® Thermoset Microwave Materials*. Rogers Corporation. 2018.
URL: <https://rogerscorp.com/-/media/project/rogerscorp/documents/advanced-connectivity-solutions/english/data-sheets/tmm-thermoset-laminate-data-sheet-tmm3----tmm4----tmm6----tmm10----tmm10i----tmm13i.pdf>.

DECLARATION

I, *Alessio Berto*, declare that the Master's thesis entitled *Wideband Fabry-Pérot cavity antenna with overlapping feeds for Advanced Communications* contains no material that has been submitted previously, in whole or in part, for the award of any other academic degree or diploma. Except where otherwise indicated, this thesis is my own work.

Torino, December 2019

Alessio Berto